THE OPTICAL PROPERTIES OF PYROCHLORE OXIDES $R_2Mo_2O_{7-\delta}$ (R: Sm, Gd, AND Ho), THE HEAVY-FERMION UNi_2Al_3, AND THE ORGANIC CONDUCTOR $(TMTSF)_2ClO_4$

By

Ning Cao, B.Sc., M.Sc.

A Thesis

Submitted to the Faculty of Graduate Studies

in Partial Fulfilment of the Requirements

for the Degree

Doctor of philosophy

McMaster University

September, 1995

DOCTOR OF PHILOSOPHY (1995) **McMASTER UNIVERSITY**

(Physics) Hamilton, Ontario

TITLE: The Optical Properties of Pyrochlore Oxides $R_2Mo_2O_{7-\delta}$ (R: Sm, Gd, and Ho), The Heavy-Fermion UNi_2Al_3, and The Organic Conductor $(TMTSF)_2ClO_4$

AUTHOR: Ning Cao, B.Sc. (Nanjing Normal University)
M.Sc. (McMaster University)

SUPERVISOR: Dr. T. Timusk

NUMBER OF PAGES: viii, 142

THE OPTICAL PROPERTIES OF PYROCHLORE OXIDES $R_2Mo_2O_{7-\delta}$ (R: Sm, Gd, AND Ho), THE HEAVY-FERMION UNi_2Al_3, AND THE ORGANIC CONDUCTOR $(TMTSF)_2ClO_4$

ABSTRACT

The temperature dependence of the reflectance of the spin-glass materials $R_2Mo_2O_{7-\delta}$ (R: Sm, Gd, and Ho) has been measured for frequencies from 40 to 40,000 cm^{-1}. The real part of the AC conductivity of $Sm_2Mo_2O_{7-\delta}$, derived from Kramers-Kronig analysis, indicates a Drude-like behavior as the temperature is lowered. Between 150 and 40 K the scattering rate shows a sharp drop which is attributed to the scattering of conduction electrons by short-range ordered moments of the Mo ions. Below the spin-glass transition temperature T_f(≅40 K) the scattering rate saturates due to the freezing out of the moments. $Gd_2Mo_2O_{7-\delta}$ behaves like a poor metal at room temperature, but at low temperatures shows a linear increase in the conductivity for frequencies up to 400 cm^{-1} suggesting a localized hopping conductivity. The localization remains in the spin-glass state for $T<T_f$(≅25 K). The conductivity of $Ho_2Mo_2O_{7-\delta}$ is semiconductive with a small and slightly temperature-dependent gap around 0.25 eV. Our optical results support a qualitative band model proposed by Sleight and Bouchard for the pyrochlore oxides.

The optical properties of the new heavy-fermion superconductor UNi_2Al_3 have been investigated at temperatures between 10 and 300 K using reflectance spectroscopy. A characteristic energy scale (ω_c≅90 cm^{-1}), with almost the same value as the characteristic temperature T_o derived from measurements of the DC resistivity and susceptibility, is obtained from the optical conductivity. At high temperatures ($T>T_o$), this scale represents the energy gap between the ground and excited level that results from the crystal-field splitting of the $5f^2$ (J=4) level of the tetravalent uranium ion. In the low-temperature coherent region ($T<T_o$), a narrow, Drude-like, quasiparticle absorption mode develops. This mode is described using a frequency-dependent scattering rate $\Gamma(\omega)$ and mass enhancement factor $\lambda(\omega)$. This free-carrier mode may originate from a hybridization between the $3d$ conduction band of nickel and the $5f$ bands of uranium. Parameters such as

the renormalized scattering rate γ^* and the renormalized plasma frequency $\omega_P{}^*$ of the quasiparticle mode, as well as the quasiparticle band width W at 10 K are derived using the model developed by Millis and Lee.

The polarized optical reflectance of the quasi-one-dimensional organic conductor $(TMTSF)_2ClO_4$ has been measured along the chain axis from the far-infrared (~8 meV) to the visible (~1 eV) at temperatures between 10 and 300 K. The real part of the optical conductivity shows that a gap ($2\Delta \cong 21$ meV) develops in the conductivity at low temperatures that may be related to the long-range ordering of SDW found in the NMR measurement for $T < T_c{}^{3D} \cong 25$ K. Precursors of the SDW gap (pseudogap) that may result from the one-dimensional SDW fluctuations are visible as high as 100 K and are also indicated by both the temperature dependent integrated conductivity spectral weight between 2Δ and 1000 cm^{-1} and intensity of the phase phonons. Our results suggest that the very high DC conductivity of this material at low temperatures is carried by a narrow mode at zero frequency. This narrow mode has been supported by both the fitting of the reflectance data below 60 K to a Drude term plus the other terms and the large negative values in $\varepsilon_1(\omega)$ at low frequencies. The spectral weight associated with this narrow mode decreases sharply with increasing temperature which is similar to the temperature dependence of the spectral weight of the induced phonons found in far-infrared. This indicates that both the narrow zero-frequency mode and the induced phonons have the same collective-excitation origin in this quasi-one-dimensional material.

ACKNOWLEDGEMENTS

I wound like to thank my supervisor, Dr. T. Timusk, for his supervision, encouragement, and ideas which helped me finish this thesis work. I have always been impressed by his enthusiasm towards improving the experimental techniques and obtaining better results.

I am grateful to Dr. J.E. Greedan and his co-workers Drs. P. Gougeon at Université de Rennes in France, N.P. Raju, and G. Liu for supplying us with single crystals of $R_2Mo_2O_{7-\delta}$ (R: Sm, Gd, and Ho) as well as the corresponding DC resistivity and susceptibility results. I have benefited a lot from conversations with Drs. Greedan and Raju about how to understand the experimental results. I also thank Drs. B.D. Gaulin, J.P. Carbotte, A.J. Berlinsky, and C. Kallin for the valuable discussions on the optical results of $R_2Mo_2O_{7-\delta}$.

I thank J.D. Garrett for growing the high-quality UNi_2Al_3 single-crystal sample that made the optical measurements possible. Special thanks to Dr. D.B. Tanner and his graduate student H.L. Liu at University of Florida for measuring the low temperature, high frequency part of the reflectance spectra of UNi_2Al_3. I also thank Dr. B.D. Gaulin for discussing his latest neutron-scattering results on UNi_2Al_3 with us.

I thank Dr. K. Bechgaard at Riso National Laboratory in Denmark for supplying us with high-quality $(TMTSF)_2ClO_4$ crystals for this polarized reflectance measurements.

I thank R.A. Duncan for his technical support and G. Hewitson for supplying us with plenty of liquid helium without which the measurements at low temperatures could not be done.

I thank all the people in this lab for their appreciated help.

Finally, I thank my wife, Lu Huang, for taking care of my family so that I was able to study and do research at McMaster.

Contents

Chapter 1

Introduction

In this thesis we investigate the optical properties of three kinds of the solids: the pyrochlore oxides $R_2Mo_2O_{7-\delta}$ with R=Sm, Gd, and Ho, the heavy-fermion superconductor UNi_2Al_3, and the quasi-one-dimensional organic superconductor $(TMTSF)_2ClO_4$. There are some interesting physical properties associated with these materials. For example, the DC resistivity of $R_2Mo_2O_{7-\delta}$ (R: one of rare-earth elements) shows evidence of a metal-semiconductor transition as the size of the rare-earth ion is reduced. The measurements done on the polycrystalline samples indicate that the resistivity of $R_2Mo_2O_{7-\delta}$ with R=Nd, Sm, and Gd is metallic, whereas that with R=Tb and Y is semiconductive.[1] The question that will be asked is what causes the transition. A second example is the heavy-fermion superconductor UNi_2Al_3. It is generally believed that physical properties of heavy-fermion systems (Kondo-lattice systems), similar to those of a metal doped with few magnetic impurities (Kondo alloys), show some features characteristic of localized behavior above the characteristic temperature T_0, *e.g.*, Curie-Weiss behavior in $\chi(T)$ with an effective moment almost equal to the one for an isolated $5f$ (U) ion and isolated-impurity-scattering of conduction electrons in $\rho(T)$. However, the coherence effects, *e.g.*, enormously enhanced specific-heat coefficient $\gamma(0)$ and Pauli susceptibility $\chi(0)$ over conventional metals, and a sharp drop of the DC resistivity (T^2 dependence at very low temperatures), are developed in the low-temperature region ($T<T_0$).[2] Therefore, the peculiarity of heavy-fermion materials appears at a low-energy scale. It is important to experimentally determine this scale. Also it is known that crystal field (CF) effects play a critical role in understanding the results

of susceptibility, inelastic neutron scattering, and specific-heat experiments in heavy-fermion systems.[3] Can the CF effects be reflected in the photon-induced excitonic spectrum? A third example is related to the quasi-one-dimensional organic superconductor $(TMTSF)_2ClO_4$. Its longitudinal (chain-axis) DC resistivity shows a type of metallic behavior in the normal state ($T>T_c$): the resistivity decreases sharply with decreasing temperature.[4] However, the far-infrared optical conductivity, obtained from the polarized reflectance measurement along this direction, exhibits a non-metallic behavior at low temperatures, decreasing as the temperature and frequency are lowered.[5] How can one reconcile the DC conductivity data with the AC data in $(TMTSF)_2ClO_4$?

Using the technique of reflectance spectroscopy described in this thesis, one can obtain some experimental information, particularly, the information of photon-induced excitations, needed in order to understand these materials. For example, a metal manifests itself in the optical conductivity spectrum, obtained from performing Kramers-Kronig analysis (see Chapter 2), by a Drude excitation peak centered at zero frequency and one can extract the Drude parameters that are used to study the electron-scattering process in the material. For another example, if the material is a semiconductor, it will show a gap feature in the conductivity spectrum and the determination of the gap value is very important for understanding the electronic structure of the material.

The organization of this thesis is as follows. Chapter 2 introduces the theoretical background as well as the techniques that are related to reflectance spectroscopy. Chapter 3, 4, and 5 are mainly devoted to the presentation of the experimental results and the discussions of the properties of $R_2Mo_2O_{7-\delta}$ (R=Sm, Gd, and Ho), UNi_2Al_3 in the basal plane, and $(TMTSF)_2ClO_4$ along the chain axis. Finally, some remarks will be given in Chapter 6.

Chapter 2

Theoretical Background and Experimental Techniques

Reflectance spectroscopy is one of experimental techniques used to probe the electrodynamic response of a material. Basically, this technique measures the frequency dependent reflectance $R(\omega)$ of the sample over a large frequency range. To obtain both real and imaginary parts of the optical response functions, one also needs to know the corresponding frequency dependent phase factor $\theta(\omega)$ which is the shift of the phase between the reflected electric field and the incident electric field. These two quantities, $R(\omega)$ and $\theta(\omega)$, are related to each other by a Kramers-Kronig relation.[6] By performing a Kramers-Kronig transformation one can get $\theta(\omega)$ and, consequently, derive the complex dielectric function $\tilde{\varepsilon}(\omega)$ whose imaginary part is closely related to the optical conductivity in which we are most interested. This Chapter consists of two sections. In section 1 the theoretical background for reflectance spectroscopy including Kramers-Kronig analysis is introduced. The spectroscopic technique used in this work is described in section 2.

2.1. Introduction to Theoretical Background

2.1.1. Optical Parameters

The propagation of an electromagnetic wave in a medium is described by the Maxwell's electromagnetic wave equation that is given by,

$$\nabla^2 \vec{E} = \frac{\varepsilon}{c^2}\frac{\partial^2 \vec{E}}{\partial t^2} + \frac{4\pi\sigma}{c^2}\frac{\partial \vec{E}}{\partial t}, \tag{2.1}$$

where $\vec{E}$ is the electric-field vector, ε and σ are the dielectric function and conductivity of the medium, respectively, and c is the velocity of light. Inserting a plane-wave solution,

$$\vec{E} = \vec{E}_o e^{i(\vec{q}.\vec{r}-\omega t)}, \tag{2.2}$$

where $\vec{q}$ and ω are the wave vector and the frequency of the electric field, respectively, into Eqn. 2.1 one gets the dispersion relation in the medium as:

$$q^2 = \frac{\omega^2}{c^2}(\varepsilon + i\frac{4\pi\sigma}{\omega}). \tag{2.3}$$

The complex refractive index $N(\omega)$ is defined as:

$$N(\omega) = \sqrt{\varepsilon + i\frac{4\pi\sigma}{\omega}} = n(\omega) + ik(\omega), \tag{2.4}$$

where $n(\omega)$ is the index of refraction that represents the dynamic response of the medium to the incident electromagnetic field and $k(\omega)$ is the extinction coefficient which is related to the absorption coefficient $\alpha(\omega)$ by the relation: $\alpha(\omega) = \frac{2k(\omega)\omega}{c}$. The complex refractive index $N(\omega)$ is also related to the complex dielectric function $\bar{\varepsilon}(\omega)$ by the expression,

$$N(\omega) = \sqrt{\tilde{\varepsilon}(\omega)} = \sqrt{\varepsilon_1(\omega) + i\varepsilon_2(\omega)}, \tag{2.5}$$

where $\varepsilon_1(\omega)$ and $\varepsilon_2(\omega)$ are the real and imaginary parts of the complex dielectric function. So, from Eqs. 2.4 and 2.5, the relation between $\varepsilon_1(\omega)$, $\varepsilon_2(\omega)$ and $n(\omega)$, $k(\omega)$ are given as follows,

$$\varepsilon_1(\omega) = n(\omega)^2 - k(\omega)^2, \tag{2.6}$$

$$\varepsilon_2(\omega) = 2n(\omega)k(\omega) \tag{2.7}$$

or alternatively,

$$n(\omega) = \frac{1}{\sqrt{2}}\sqrt{\sqrt{\varepsilon_1(\omega)^2 + \varepsilon_2(\omega)^2} + \varepsilon_1(\omega)}, \tag{2.8}$$

$$k(\omega) = \frac{1}{\sqrt{2}}\sqrt{\sqrt{\varepsilon_1(\omega)^2 + \varepsilon_2(\omega)^2} - \varepsilon_1(\omega)}. \tag{2.9}$$

The real part of the optical conductivity $\sigma_1(\omega)$ is related to $\varepsilon_2(\omega)$ by the relation:

$$\sigma_1(\omega) = \frac{\omega\varepsilon_2(\omega)}{4\pi}. \tag{2.10}$$

2.1.2. Kramers-Kronig Analysis

The physical quantity measured in this work is the reflectance $R(\omega)$. As mentioned above, the function describing the electrodynamic response to an incident electromagnetic field $E_i(\omega)$ is complex, *i.e.*, both the amplitude and the phase of the reflected field $E_r(\omega)$ change in comparison with those of the incident field $E_i(\omega)$. The reflectivity coefficient $r(\omega)$ is defined as the ratio of the reflected electric field $E_r(\omega)$ to the incident field $E_i(\omega)$,

$$r(\omega) = \frac{E_r(\omega)}{E_i(\omega)} = \sqrt{R(\omega)}e^{i\theta(\omega)}, \tag{2.11}$$

where $\theta(\omega)$ is the phase factor. From Eqn. 2.11 one can easily see that the reflectance $R(\omega)$ is the squared modulus of $r(\omega)$. If the reflectance $R(\omega)$ is measured in a normal incidence configuration, then, $r(\omega)$ can be expressed in terms of the optical parameters $n(\omega)$ and $k(\omega)$ as the following formula,[6]

$$r(\omega) = \frac{n(\omega) + ik(\omega) - 1}{n(\omega) + ik(\omega) + 1}. \tag{2.12}$$

To determine the complex optical response function, such as $n(\omega)$ and $k(\omega)$, one needs to know the phase factor $\theta(\omega)$. Fortunately, these two quantities $\theta(\omega)$ and $R(\omega)$ are not independent of each other. $\theta(\omega)$ is related to $R(\omega)$ by an integration, the so-called Kramers-Kronig transformation,[6]

$$\theta(\omega) = \frac{1}{2\pi}\int_0^\infty \frac{\ln[R(s)] - \ln[R(\omega)]}{\omega^2 - s^2} ds, \tag{2.13}$$

which can be integrated numerically. Once $\theta(\omega)$ is obtained, $n(\omega)$ and $k(\omega)$ can be calculated using the following formulas,

$$n(\omega) = \frac{1 - R(\omega)}{1 + R(\omega) - 2\sqrt{R(\omega)}\cos\theta(\omega)} \tag{2.14}$$

and

$$k(\omega) = \frac{2\sqrt{R(\omega)}\sin\theta(\omega)}{1 + R(\omega) - 2\sqrt{R(\omega)}\cos\theta(\omega)}, \tag{2.15}$$

2.1.3. The Lorentz Oscillator

The most frequently used model to represent the photon-induced excitations in a solid is the Lorentz-oscillator model which can be derived from a classical Newton's equation (see Appendix A). In this model, the complex dielectric function $\bar{\varepsilon}(\omega)$ is expressed as a sum of the oscillators for the absorption processes taking place in the solid,

$$\bar{\varepsilon}(\omega) = \varepsilon_\infty + \sum_i \frac{{\omega_{Pi}}^2}{{\omega_i}^2 - \omega^2 - i\omega\gamma_i}, \tag{2.16}$$

where ω_i, γ_i, and ω_{Pi} are the position, width, and plasma frequency of the i^{th} oscillator, respectively, and ε_∞ is the high-frequency dielectric constant. A special example is for intraband excitations of free carriers in a metal, referred to as the Drude model, in which case the oscillator frequency is zero (ω_i=0),

$$\varepsilon(\omega) = 1 - \frac{{\omega_{PD}}^2}{\omega^2 + i\omega\gamma_D}, \tag{2.17}$$

where the Drude plasma frequency $\omega_{PD} = \sqrt{\frac{4\pi ne^2}{m^*}}$, here n and m^* are the density and the effective mass of free carriers, respectively. The corresponding Drude conductivity can be easily deduced from Eqn. 2.10 as:

$${\sigma_1}^D(\omega) = \frac{{\omega_{PD}}^2\gamma_D}{4\pi(\omega^2 + {\gamma_D}^2)}. \tag{2.18}$$

2.1.4. Extrapolations of Measured Reflectance Data

As seen in Eqn. 2.13, to perform Kramers-Kronig analysis one needs to know the reflectance $R(\omega)$ from $\omega = 0$ to ∞. Technically, $R(\omega)$ can only be measured in a limited frequency range. Therefore, it is necessary to properly extrapolate $R(\omega)$ outside of the measured frequency range. Some of the extrapolations used in this work are:

(a) Hagen-Rubens approximation at low frequencies

This approximation is usually used for a metal or a semimetal that follows the Drude law of conductivity in a low frequency region, *i.e.*, in the region where $R(\omega)$ approaches unity. If $\omega << \gamma_D$, then, Eqn. 2.18 can be approximately taken as:

$$\sigma_1^{\,D}(\omega) = \frac{\omega_{PD}^{\,2}}{4\pi\gamma_D}, \tag{2.19}$$

which is independent of frequency. In this case, since $\varepsilon_1(\omega) << \varepsilon_2(\omega)$, one has the relation,

$$[n(\omega)+ik(\omega)]^2 = \varepsilon_1(\omega)+i\varepsilon_2(\omega) \approx i\varepsilon_2(\omega) = \frac{4\pi\sigma_1}{\omega}i. \tag{2.20}$$

From Eqn. 2.20 one obtains

$$n(\omega) \approx k(\omega) \approx \sqrt{\frac{2\pi\sigma_1}{\omega}}. \tag{2.21}$$

On the other hand, from Eqn. 2.12 we have,

$$R(\omega) = |r(\omega)|^2 = \frac{[n(\omega)-1]^2 + k(\omega)^2}{[n(\omega)+1]^2 + k(\omega)^2}. \tag{2.22}$$

So, finally, the Hagen-Rubens approximation can be expressed as:

$$R(\omega) \approx 1 - \frac{2}{n(\omega)} \approx 1 - \sqrt{\frac{2\omega}{\pi\sigma_1}}. \tag{2.23}$$

One can use the lowest-frequency experimental reflectance data or use the DC conductivity data (obtained directly from the DC resistivity measurement) of the studied material to determine the prefactor $\sqrt{\frac{2}{\pi\sigma_1}}$.

(b) Free-electron behavior at high frequencies

The measured reflectance data are ended at ~40,000 cm^{-1} in this work and a power-law behavior $R(\omega) \propto \omega^{-s}$ (s is an integer) is used to extrapolate the reflectance data between 40,000 and 10^6 cm^{-1}. Beyond 10^6 cm^{-1} a free-electron behavior $R(\omega) \propto \omega^{-4}$ is usually chosen to extend the data to infinity. Here, a brief derivation of this relation is given below. The real and imaginary parts of the Drude dielectric function can be easily deduced from Eqn. 2.17 as:

$$\varepsilon_1(\omega) = 1 - \frac{\omega_{PD}^{\ 2}}{\omega^2 + \gamma_D^{\ 2}} \tag{2.24}$$

and

$$\varepsilon_2(\omega) = \frac{\omega_{PD}^{\ 2}\gamma_D}{\omega(\omega^2 + \gamma_D^{\ 2})}, \tag{2.25}$$

respectively. For the high frequency region (ω>10^6 cm^{-1}) one has a situation of

$\omega >> \omega_{PD}, \gamma_D$. So, Eqs. 2.24 and 2.25 approach

$$\varepsilon_1(\omega) \approx 1 - \frac{\omega_{PD}^2}{\omega^2} \tag{2.26}$$

and

$$\varepsilon_2(\omega) \approx 0, \tag{2.27}$$

Therefore, in this case, according to Eqs. 2.8 and 2.9, $n(\omega) \approx \sqrt{\varepsilon_1(\omega)} \approx 1 - \frac{\omega_{PD}^2}{2\omega^2}$ and $k \approx 0$. Finally, from Eqn. 2.22 the reflectance in the high frequency region can be expressed as:

$$R(\omega) \approx \frac{[n(\omega)-1]^2}{[n(\omega)+1]^2} \approx \frac{\omega_{PD}^4}{16\omega^4}. \tag{2.28}$$

With the reflectance measured in a certain frequency range and the use of some appropriate extrapolations to extend $R(\omega)$ over the entire frequency range, one can perform the Kramers-Kronig analysis, shown in Eqn. 2.13, and obtain the phase factor $\theta(\omega)$. Knowing $R(\omega)$ and $\theta(\omega)$ and using Eqs. 2.6, 2.7, 2.14, and 2.15 we are in the position to obtain the complete electrodynamic response functions $\varepsilon_1(\omega)$ and $\varepsilon_2(\omega)$, from which the optical properties of the studied sample can be extracted.

2.1.5. Frequency Dependent Scattering Rate and Renormalization Factor of a Heavy-Fermion System

For a heavy-fermion system the interaction between conduction electrons and spins of $4f$ or $5f$ electrons near the Fermi level can cause the scattering rate as well as the renormalization factor of quasiparticles to be frequency dependent. According to Allen and Mikkelsen, these two quantities can be extracted using a generalized Drude model.[7] The formulas used in this model are introduced below. Firstly, a generalized Drude-like complex conductivity is expressed as:

$$\sigma(\omega) = \frac{\omega_{eff}(\omega)^2}{4\pi[\Gamma_{eff}(\omega) - i\omega]}, \tag{2.29}$$

where,

$$\Gamma_{eff}(\omega) = \frac{\Gamma(\omega)}{1+\lambda(\omega)} \tag{2.30}$$

and

$$\omega_{eff}(\omega)^2 = \frac{\omega_P{}^2}{1+\lambda(\omega)}. \tag{2.31}$$

Here $\Gamma_{eff}(\omega)$ and $\omega_{eff}(\omega)$ are the effective scattering rate and plasma frequency of quasiparticles, respectively, $\Gamma(\omega)$ and $\lambda(\omega)$ are the frequency dependent scattering rate and renormalization factor for quasiparticles, respectively. Then the generalized complex

dielectric function $\tilde{\varepsilon}(\omega)$ is associated with $\sigma(\omega)$ by the relation $\tilde{\varepsilon}(\omega) = \frac{4\pi\sigma(\omega)}{\omega} i$, so, $\Gamma_{eff}(\omega)$ and $\omega_{eff}(\omega)$ can be derived as:

$$\Gamma_{eff}(\omega) = -\frac{\omega\varepsilon_2(\omega)}{\varepsilon_1(\omega)} \tag{2.32}$$

and

$$\omega_{eff}(\omega)^2 = -\varepsilon_1(\omega)\left[\omega^2 + \Gamma_{eff}(\omega)^2\right]. \tag{2.33}$$

Finally, using Eqs. 2.30 and 2.31, $\Gamma(\omega)$ and $\lambda(\omega)$ can be expressed as:

$$\Gamma(\omega) = \frac{\Gamma_{eff}(\omega)\omega_P{}^2}{\omega_{eff}(\omega)^2} \tag{2.34}$$

and

$$\lambda(\omega) = \frac{\omega_P{}^2}{\omega_{eff}(\omega)^2} - 1. \tag{2.35}$$

In order to use this formalism: (a) there must not be any interband transitions, and (b) one must know the value of the bare plasma frequency ω_p independently.

2.2. Experimental Techniques

2.2.1. Spectrometers

Two spectrometers are used in this optical work, a Michelson interferometer and a grating spectrometer which cover the frequency ranges between 30 and 9000 cm^{-1} and between 3800 and 40,000 cm^{-1}, respectively.

(a) Michelson Interferometer

Fig. 2.1 shows the schematic of the Michelson interferometer. A brief description is given here to explain how the interferometer works. As shown in the figure, light emitted from the lamp source hits a paraboloidal mirror to form a parallel beam. The parallel beam reaches the beam-splitter where one half of the beam is directly transmitted to a fixed mirror, while the other half is reflected 45^{o} to propagate toward the moving mirror. Both of the beams bounce back from the fixed and moving mirrors, and are recombined at the beam-splitter where they *interfere with each other coherently* due to the difference (δ) in path length. The coherent beam is reflected from a flat mirror and a paraboloidal mirror, passes through the chopper (C), focuses at the aperture (A), passes through the polarizer holder (P), is reflected from a toroidal mirror, goes through a polypropylene (in far-infrared) or a KRS-5 (in near-infrared to ultraviolet) window, and hits a sample or a reference mirror in a small angle (near a normal incidence) inside an evacuated chamber (10^{-5} torr). The beam is then reflected from another toroidal mirror and finally reaches the detector. The signal received by the detector is the interferogram, *i.e.*, intensity *vs.* δ, which is transformed into a spectrum , *i.e.*, intensity *vs.* frequency, using a Fourier transformation. It is necessary to use different combinations of lamps, beam-splitters, and detectors, which are shown in Table 2.1, for different frequency

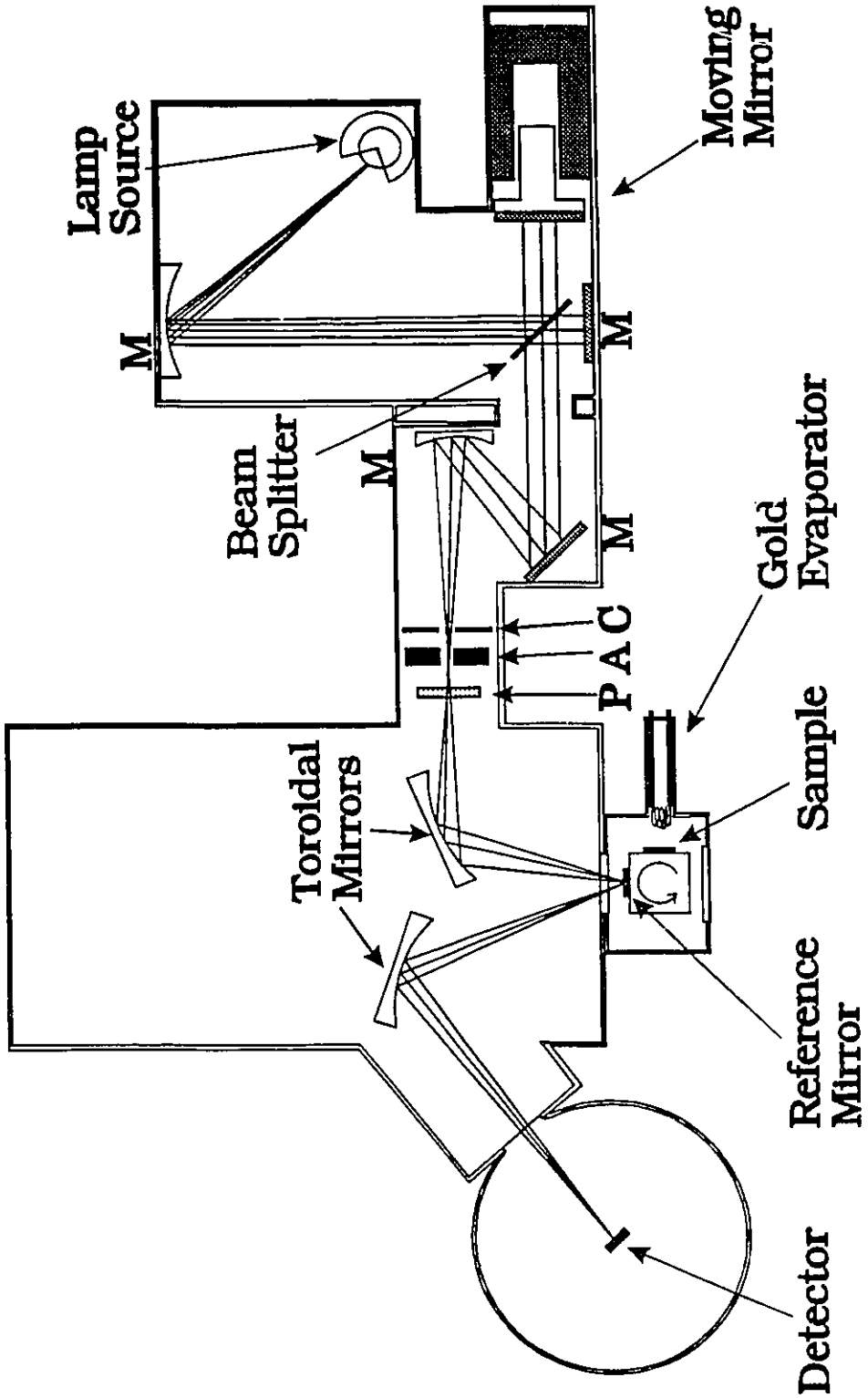

Figure 2.1. Schematic of the Michelson interferometer used to measure reflectance between 30 and 9000 cm^{-1}.

ranges in order to obtain the optimum reflectance spectra.

Table 2.1. Combinations of lamps, beam-splitters, and detectors for the Michelson interferometer for the different frequency ranges:

Range (cm^{-1})	**Lamp**	**Beam-splitter**	**Detector**
30~200	Hg arc	12.5 μ Mylar	1.2 K Si bolometer
60~700	Hg arc	3 μ Mylar	4.2 K Si bolometer
500~9000	quartz W-halogen	KBr	77 K HgCdTe (MCT)

(b) Grating Spectrometer

The grating spectrometer uses the fact that, if white light shines on a grating, its frequency components will diverge. Therefore, a fixed detector can only pick up a single-frequency component for each grating orientation. By changing of the grating orientation continuously, one can obtain a power spectrum over a large frequency range.

The configuration of the grating spectrometer is displayed in Fig. 2.2. The light emitted from the source lamp (S) passes through a chopper, which generates a comparison AC signal for the lock-in amplifier which measures and amplifies the reflectance signal from the sample. It then passes through an aperture (A), and is reflected from a plane mirror and a toroidal mirror which focuses the incidence upon the sample or the reference mirror located in an evacuated chamber (~10^{-5} torr) (C). The beam then bounces back from another toroidal and plane mirror and travels through a filter (F), whose function is to eliminate the effects of the higher-order diffraction, and the entrance slit. The light is then reflected from a sphere mirror, and hits the grating (G) whose orientation can be

changed continuously by rotating it about an axis perpendicular to the page. Finally, the dispersed beam bounces back from another sphere mirror, passes through the exit slit and a convergent lens (L), which focuses the light onto the detector (D). The signal received by the detector goes into a lock-in amplifier and the enhanced output signal is fed into a computer. As is the case with the Michelson interferometer, different combinations of lamps, filters, gratings, and detectors, which are listed in Table 2.2, are used to yield optimum reflectance spectra in the different frequency ranges.

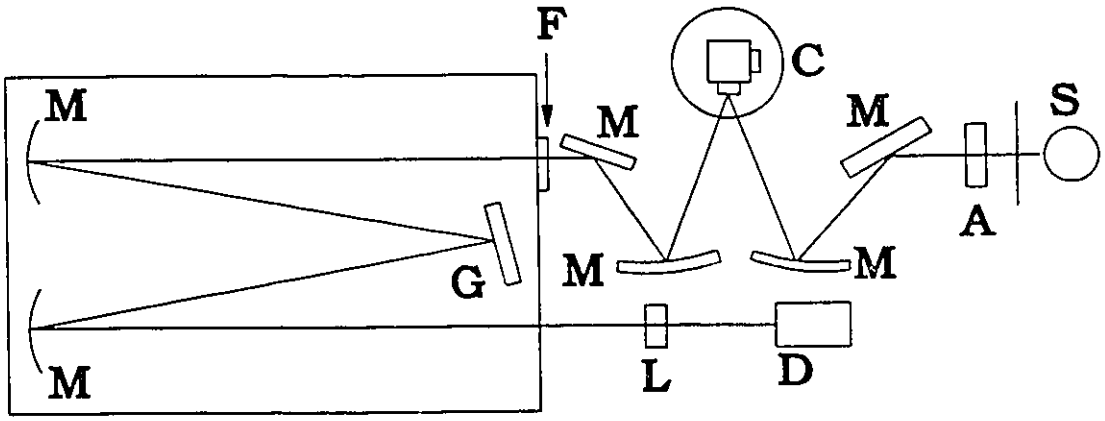

Figure 2.2. Schematic of the grating spectrometer used to measure reflectance between 3800 and 40,000 cm^{-1}.

Table 2.2. Combinations of lamps, filters, gratings, and detectors for the grating spectrometer for the different frequency ranges:

Range (cm^{-1})	Lamp	Filter	Grating (lines/mm)	Detector
3800-6300	quartz W-halogen	Ge	400	PbS
5500-10,000	quartz W-halogen	Si	400	PbS
9200-16,700	quartz W-halogen	red glass	1,200	Si photo diode
11,000-23,000	quartz W-halogen	yellow glass	1,200	photomultiplier
15,000-30,000	quartz W-halogen	blue glass	1,200	photomultiplier
20,000-35,000	deuterium	purple glass	1,200	photomultiplier
25,000-40,000	deuterium	#9863 glass	1,200	photomultiplier

2.2.2. Some Experimental Details

(a) Cryostat

As mentioned above, the sample and reflectance mirror are located in a evacuated chamber (~10^{-5} torr). There are two main reasons for evacuating the chamber: (1) reducing the effects of water (especially, preventing ice from forming on the sample's surface at low temperatures) and (2) the *in-situ* evaporation of metallic films (Au or Al) onto the sample's surface . The sample and reference mirror are glued to the tip of brass cones (for a smaller size of sample), which diffusely scatter all radiation that misses the sample or reference mirror. Then the sample and reflectance mirror holders are screwed on the neighboring faces of a copper block that is attached to the cold-finger of an

R.J. Hansen Hi-Tran continuous flow cryostat, which allows the temperature of the sample to vary between 10 and 300 K. The cryostat sits on a thrust bearing so that it can be rotated back and forth 90° to let the sample or reflectance mirror face on the incident beam during an experiment.

(b) Polarizer

For the polarized reflectance measurements, two wire grid polarizers were used for the frequencies ranging from 30 to ~700 cm^{-1} and from 500 to 9000 cm^{-1}, respectively. The specific polarization direction is determined using a least-squares method in which the ratio of chopper signals from the sample to those from the reference mirror, $I(\varphi)$, as a function of polarizer angle, φ, is fitted to a squared sine function $I(\varphi) = I_0 + I_1[\sin(\varphi + \varphi_0)]^2$, where I_0, I_1, and φ_0 are the fitting parameters.

(c) Calculation of the absolute reflectance

The reflected power spectrum of the sample, R_s, is obtained by performing a Fourier transformation on the interferogram obtained from the Michelson interferometer at each temperature or from the grating spectrometer at room temperature. This spectrum is normalized by the reflected power spectrum of the reference mirror, R_m, at the same temperature to get the reflectance spectrum of the sample (R_s / R_m). It is necessary to correct for the effects of scattering due to the irregular shape of the sample by evaporating a metallic film (Au for the frequency range of 30~16,700 cm^{-1} or Al for 11,000~40,000 cm^{-1}), thick enough that the incident beam cannot penetrate through the film and thin enough that it does not significantly change the sample shape, onto the sample's surface. This is done *in-situ* at room temperature. The temperature dependent reflectance measurement is then repeated using the coated sample to obtain R_c / R_m. By remeasuring the reflectance of the coated sample, the geometrical differences between the sample and

the reference mirror can also be taken into account. Finally, the absolute reflectance of the sample is calculated from the following relation,

$$R_s^{ab.}(\omega) = \frac{(R_s / R_m)}{(R_c / R_m)} R_c^{ab.}(\omega), \tag{2.36}$$

where $R_c^{ab.}(\omega)$ is the known absolute reflectance of the coated metallic film.

Chapter 3

Pyrochlore Oxides $R_2Mo_2O_{7-\delta}$ (R: Sm, Gd, and Ho)

This chapter consists of four sections. In section 1 the introduction to the physical properties, other than the optical ones, of pyrochlore oxides $R_2Mo_2O_{7-\delta}$ obtained from different kinds of experiments is given. This review will focus on transport and magnetic measurements of three members, R=Sm, Gd, and Ho, of the family on which the optical reflectance has been probed. The results of the optical properties of $R_2Mo_2O_{7-\delta}$ (R=Sm, Gd, and Ho), which have been published,[8] are presented in section 2. Some discussions and the conclusions are given in sections 3 and 4, respectively.

3.1. Introduction of Previous Experiments on $R_2Mo_2O_{7-\delta}$

The pyrochlore oxides $R_2Mo_2O_{7-\delta}$ (R: one of rare-earth elements) show spin-glass transitions at low temperatures, but they differ from usual spin-glasses in the fact that the frustration results from *intrinsic* geometrical factors, rather than from a random distribution of magnetic or non-magnetic impurities.[9,10, 11, 12, 13] One of the characteristic properties of a spin-glass is a magnetic susceptibility that begins to deviate from the Curie-Weiss (CW) law at temperatures $T>>T_f$, where T_f is the spin freezing temperature. This indicates that some local magnetic clusters, within which spins of ions become correlated, are formed above T_f. Below T_f all these correlated spins are frozen out

resulting in the dependence of susceptibility on the history of applied magnetic field. Also, in a metallic spin-glass, the DC resistivity usually exhibits a broad maximum at a temperature $T_m >> T_f$. This was found for example in AuCr, AuMn, AgMn, and CuMn alloys and was attributed to the scattering of conduction electrons by the local magnetic clusters (short-range order) formed below T_m.[14] Reflectance spectroscopy can be used in a metallic $R_2Mo_2O_{7-\delta}$ material to study the temperature and, more importantly, the frequency dependence of the scattering rate of conduction electrons leading to information about the interaction between the conduction electrons and the magnetic Mo ions.

The DC resistivity of $R_2Mo_2O_{7-\delta}$ shows evidence of a metal-semiconductor transition as the size of the rare-earth ion (R) is decreased. The measurements done on the polycrystalline samples indicate that the electrical resistivity of $R_2Mo_2O_{7-\delta}$ with R=Nd, Sm, and Gd is metallic whereas that with R=Tb and Y is semiconductive.[1] Sleight and Bouchard (SB) have proposed a qualitative band model for pyrochlore oxides which is shown in Fig. 3.1.[15] In this model, the band structure of $R_2Mo_2O_{7-\delta}$ can be drawn as two inter-penetrating networks of R_2O and $2MoO_3$. The transition is governed by the presence of a small gap, Δ, between the full narrow Mo-O π^*a valence band and the empty broad R-O σ^* conduction band. Reflectance spectroscopy can be used to gain insight into electronic excitations in these materials. For non-metallic $R_2Mo_2O_{7-\delta}$ an absorption threshold should appear in the conductivity spectrum, if the absorption is due to electrons across the semiconducting gap. If the absorption is due to electrons' hopping within Anderson localized states, then a monotonically rising conductivity should appear in a low-frequency region at low temperatures.[16] With the availability of the single crystals $R_2Mo_2O_{7-\delta}$ with R=Sm, Gd, and Ho, the conduction mechanism in these materials can be investigated using optical techniques.

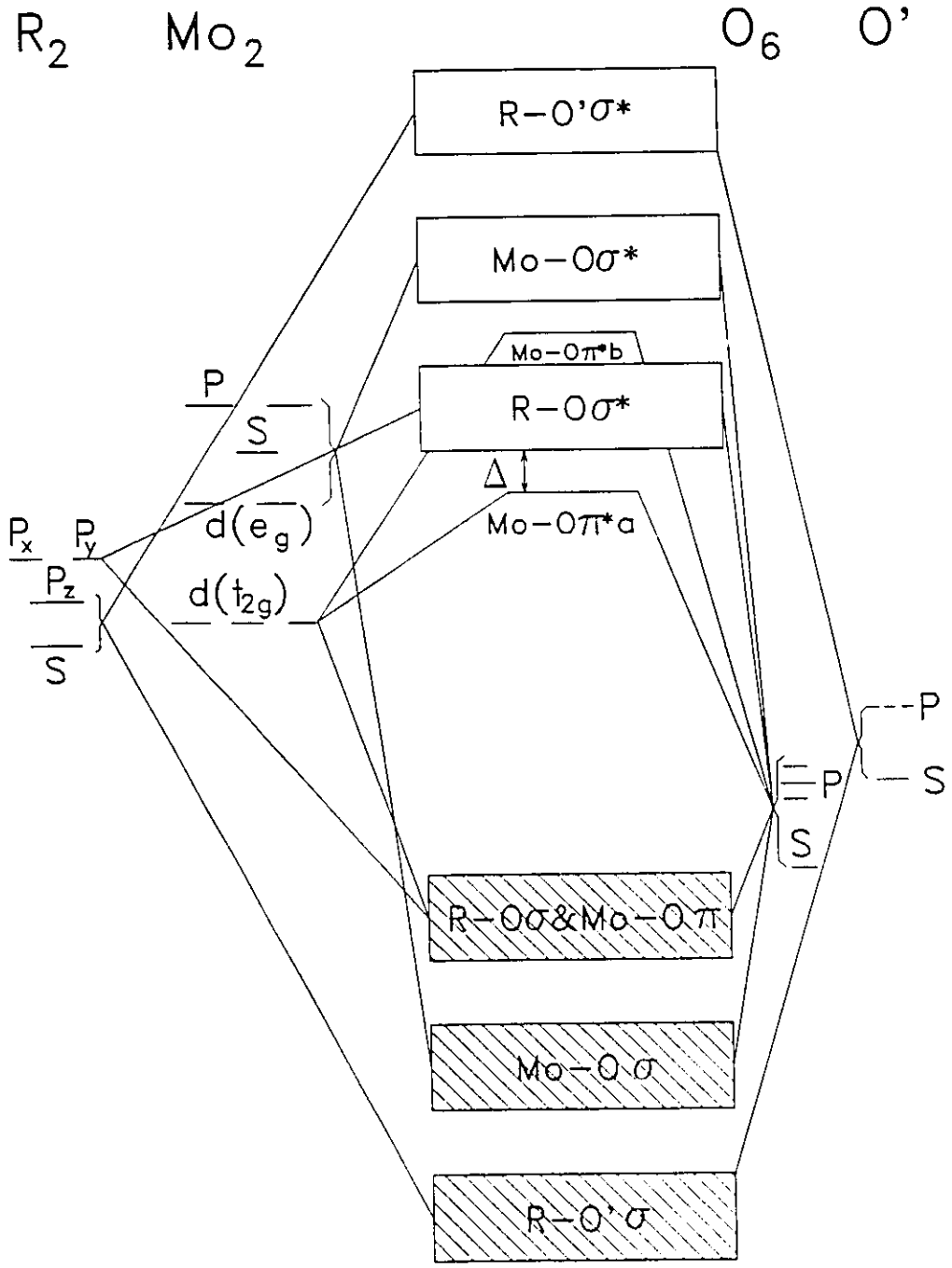

Figure 3.1. Band structure model of pyrochlore oxides $R_2Mo_2O_{7-\delta}$ proposed by Sleight and Bouchard.[15]

The crystal structure of the pyrochlore oxides has been determined by powder neutron and x-ray diffraction,[17, 12] which is shown in Fig. 3.2 (a),[18] and is face-centered cubic with a space group of $Fd\bar{3}m$. The R and Mo ions each form an infinite three-dimensional lattice of corner-sharing tetrahedra. With antiferromagnetic coupling between the nearest-neighbor Mo ions, such positions are highly frustrated.[10] This is illustrated in Fig. 3.2 (b). The optical work has been done on the three single crystals $R_2Mo_2O_{7-\delta}$ with R=Sm, Gd, and Ho. The crystals were grown by Dr. P. Gougeon at Université de Rennes in France. The DC resistivity and susceptibility of the single crystals were measured using a four-probe technique and a SQUID magnetometer, respectively, by Dr. Greedan and his co-workers at McMaster.[19] Only the brief results that are related to the optical results are shown in Figs. 3.3, 3.4, and 3.5.

Fig. 3.3 (a) shows the DC resistivity of a crystal of $Sm_2Mo_2O_{7-\delta}$. The resistivity increases slightly as the temperature is lowered from 300 to 150 K. As the temperature is reduced further the resistivity drops substantially, but surprisingly, it turns up again at 40 K. The zero-field cooling (ZFC) inverse susceptibility, displayed in Fig. 3.3 (b), shows the CW law behavior at high temperatures, which is expressed as:

$$\chi(T) = \frac{C}{T - \Theta}, \tag{3.1}$$

where Θ is the Curie temperature and

$$C = \frac{N p_{eff}^{\ 2}}{3k_B}, \tag{3.2}$$

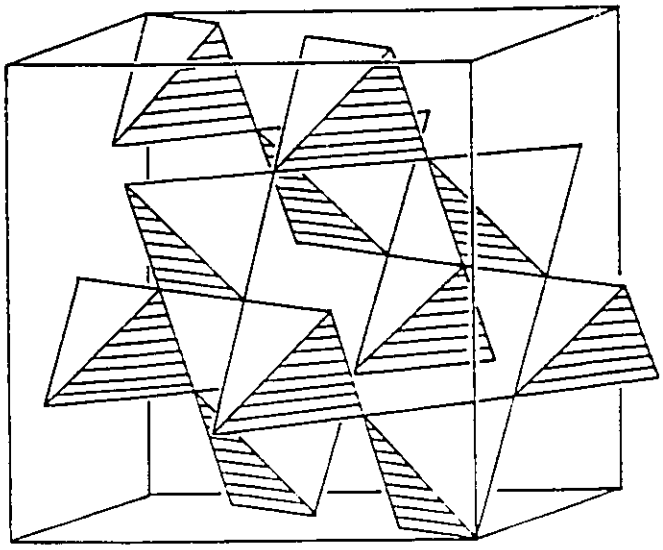

(a)

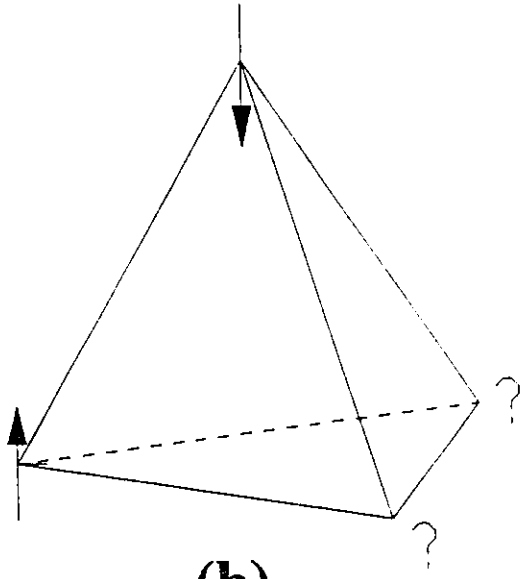

(b)

Figure 3.2. (a) The three-dimensional network of corner-sharing tetrahedra formed by the Mo^{4+} sublattice in $R_2Mo_2O_{7-\delta}$. The R^{3+} sublattice is identical to this except for a spatial displacement of $(\frac{1}{2},\frac{1}{2},\frac{1}{2})$. The frame of the cubic unit cell is also shown;[18] **(b)** The frustration exists between four antiferromagnetically coupled spins on a single tetrahedron.

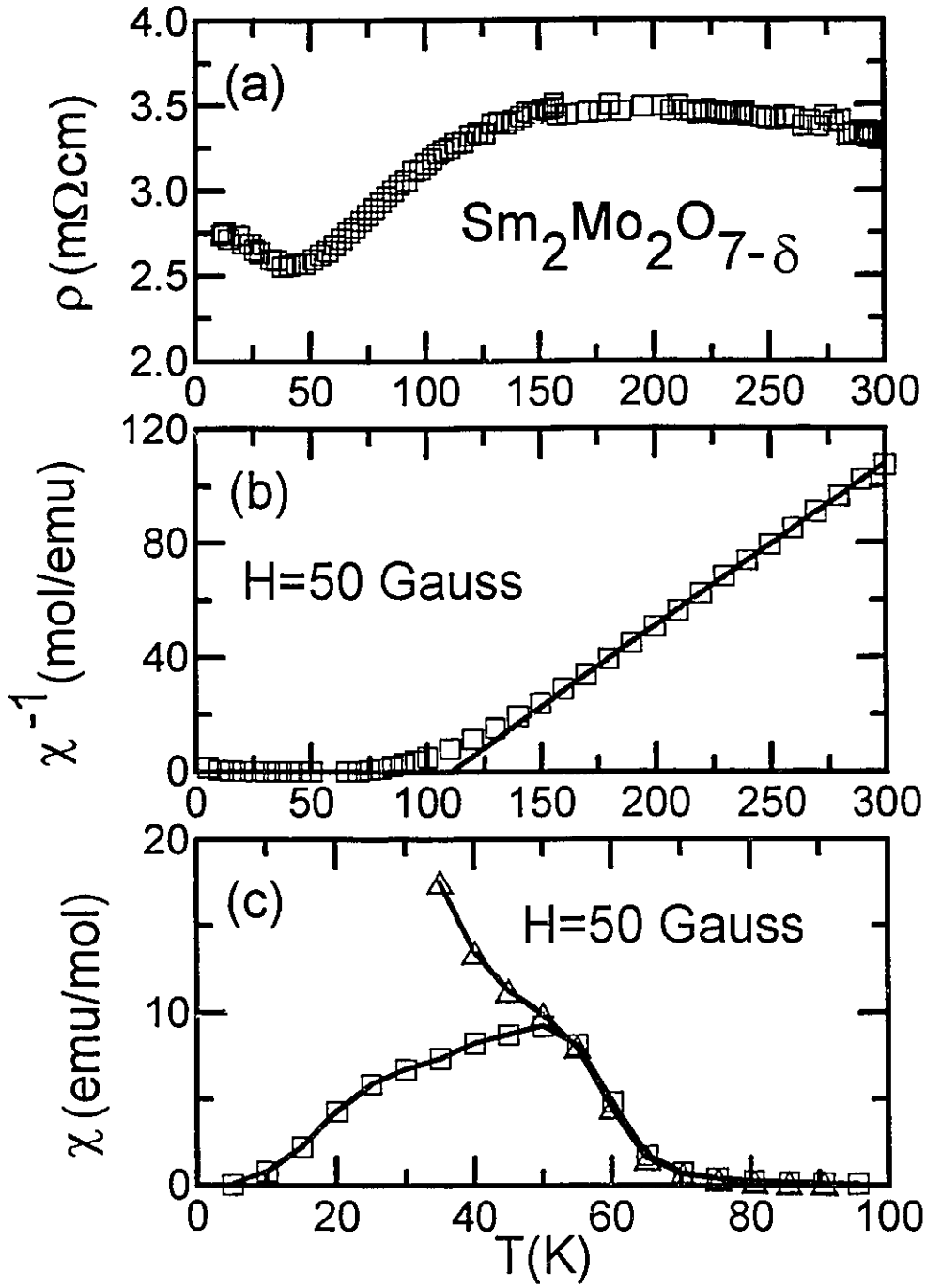

Figure 3.3. (a) The DC resistivity of $Sm_2Mo_2O_{7-\delta}$; **(b)** The inverse susceptibility of $Sm_2Mo_2O_{7-\delta}$ up to room temperature. The solid line is the result of the Curie-Weiss law fitting at high temperatures; **(c)** The susceptibility of $Sm_2Mo_2O_{7-\delta}$ at low temperatures (squares: zero-field cooling data; triangles: field cooling data; solid lines: guide to the eye).

where p_{eff}, N and k_B are the effective moments, Avogadro's number and Boltzmann constant, respectively, and deviates from this law below ~150 K which is due to a partial short-range ordering of the Mo ion moments in this temperature range. From the CW law fit, Θ and p_{eff} are found to be 110 K and 2.6 μ_B per $SmMoO_{3.5-\delta/2}$, respectively. The presence of the CW law for the susceptibility of $Sm_2Mo_2O_{7-\delta}$ at high temperatures is quite surprising because the susceptibility of an isolated Sm^{3+} ion does not satisfy this law due to thermal excitations of $4f$ electrons between neighboring levels of the L-S (orbit-spin) multiplet.[6] This raises a question of whether the CW law behavior results from the contribution of the Mo^{4+} ions or the intrinsic contribution of Sm^{3+} in this material. To answer this question, Dr. Greedan and his co-worker synthesized a polycrystalline $Sm_2Ti_2O_{7-\delta}$ sample with the same crystal structure as the one of $Sm_2Mo_2O_{7-\delta}$ and measured its susceptibility. It was found that the susceptibility of $Sm_2Ti_2O_{7-\delta}$ also agrees with the CW law at high temperatures with $p_{eff} = 3.1\ \mu_B$ per $SmTiO_{3.5-\delta/2}$ (p_{eff} =2.1~2.5 μ_B for Mo^{4+} in $Y_2Mo_2O_{7-\delta}$[11]). Because Ti^{4+} is non-magnetic, it is concluded that the susceptibility of the Sm^{3+} ions in the pyrochlore oxides does obey the CW law at high temperatures. The experimental result for the effective moments of a free Sm^{3+} ion is 1.5 μ_B, whereas the effective moments for a free Mo^{4+} ion obtained from the Hund Rules is 2.8 μ_B.[6] Therefore, the contributions of the Sm^{3+} and Mo^{4+} ions in $Sm_2Mo_2O_{7-\delta}$ to the susceptibility disagree with those of the free ions. Fig. 3.3 (c) shows the magnetic susceptibility of the $Sm_2Mo_2O_{7-\delta}$ crystal. Below the freezing temperature T_f (~50 K) the susceptibility depends on the history of the applied magnetic field: with ZFC some of the magnetic moments are frozen at low temperatures, a characteristic of spin-glass materials.

The DC resistivity of the $Gd_2Mo_2O_{7-\delta}$ crystal, shown in Fig. 3.4 (a), is quite different from that of $Sm_2Mo_2O_{7-\delta}$. The resistivity is non-metallic, increasing as the

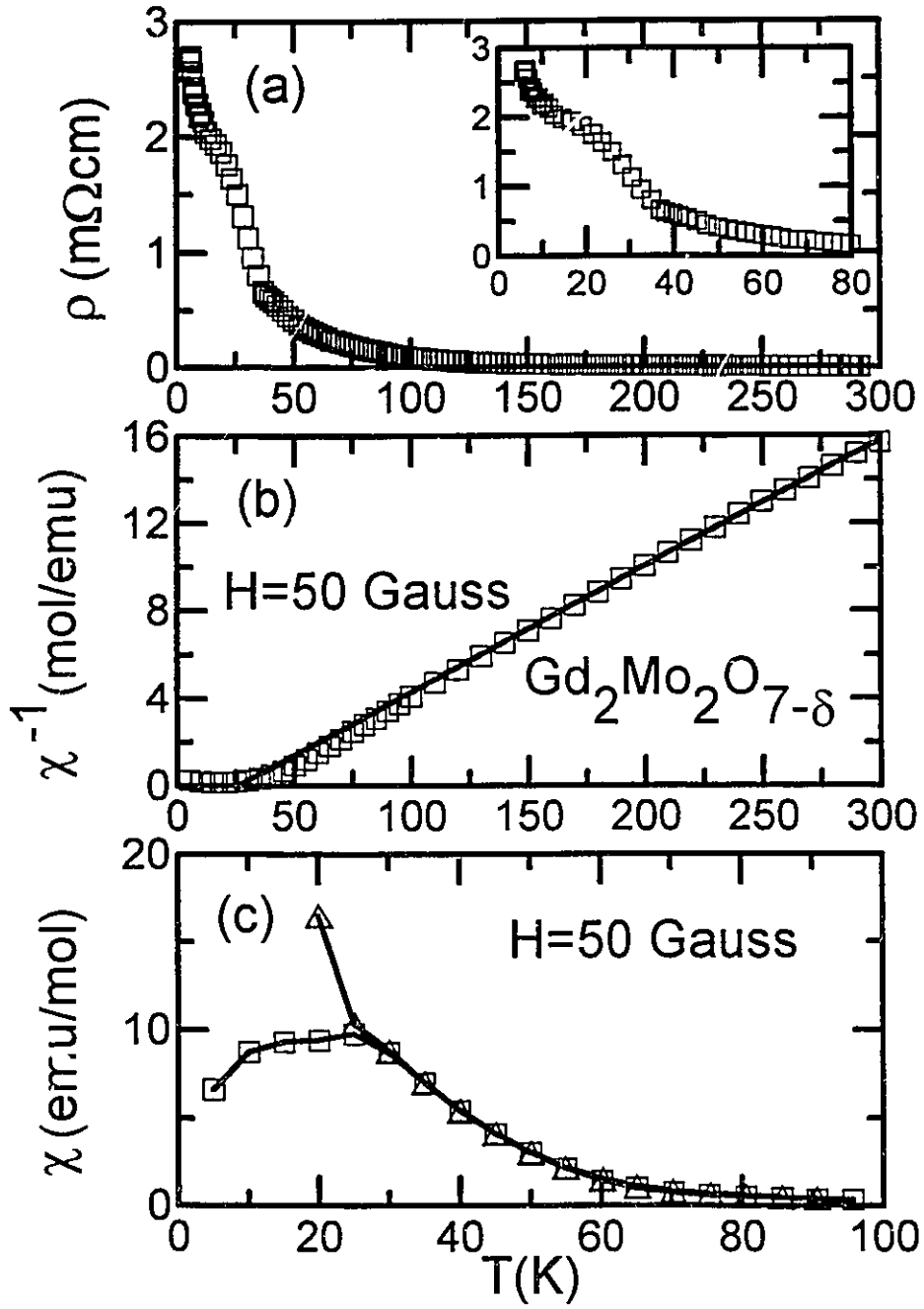

Figure 3.4. **(a)** The DC resistivity of $Gd_2Mo_2O_{7-\delta}$ up to room temperature. The inset is the DC resistivity at low temperatures; **(b)** The inverse susceptibility of $Gd_2Mo_2O_{7-\delta}$ up to room temperature. The solid line is the result of the Curie-Weiss law fitting at high temperatures; **(c)** The susceptibility of $Gd_2Mo_2O_{7-\delta}$ at low temperatures (squares: zero-field cooling data; triangles: field cooling data; solid lines: guide to the eye).

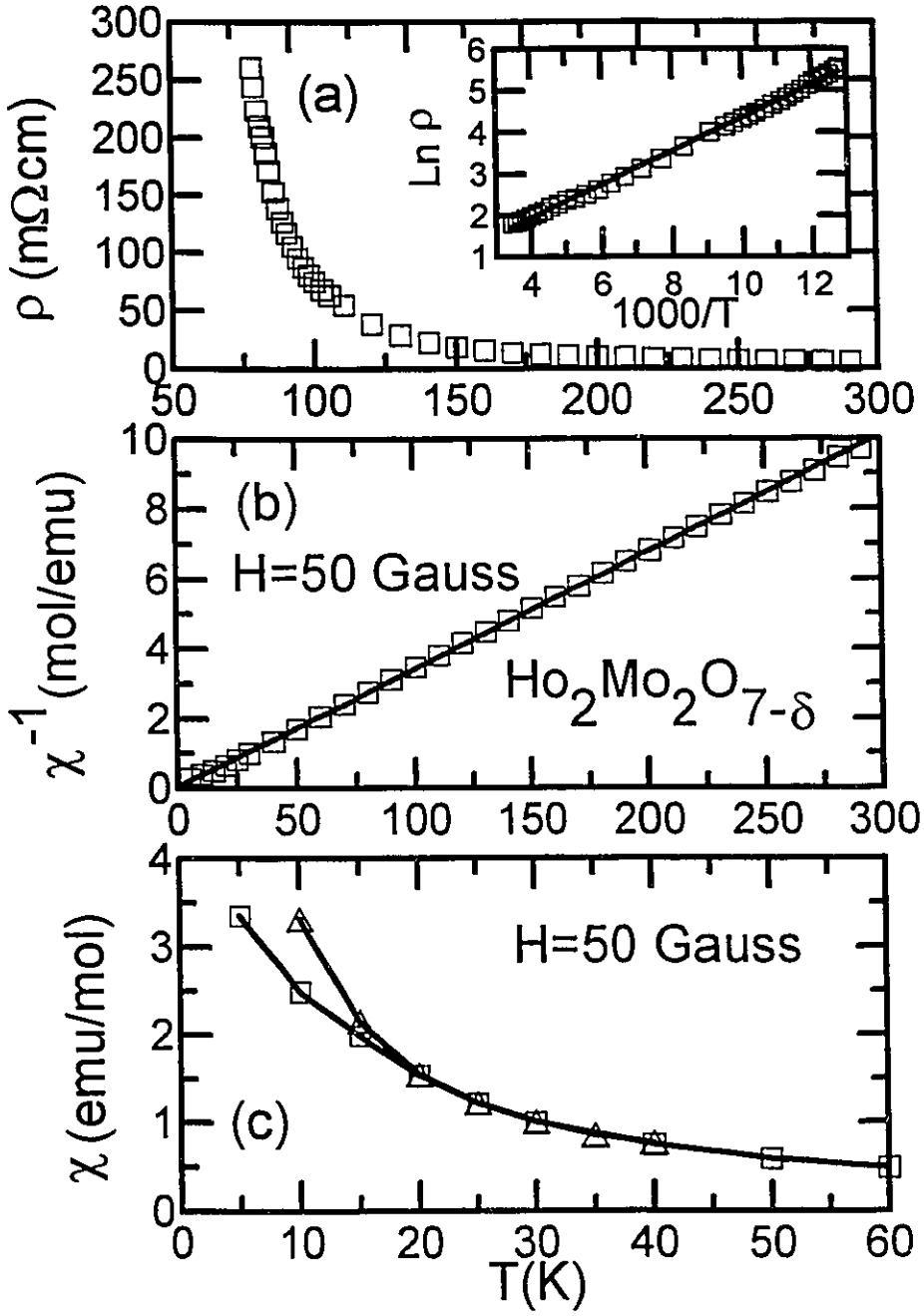

Figure 3.5. **(a)** The DC resistivity of $Ho_2Mo_2O_{7-\delta}$. The inset is the plot of $\ln(\rho)$ *vs.* $1000/T$; **(b)** The inverse susceptibility of $Ho_2Mo_2O_{7-\delta}$ up to room temperature. The solid line is the result of the Curie-Weiss law fitting; **(c)** The susceptibility of $Ho_2Mo_2O_{7-\delta}$ at low temperatures (squares: zero-field cooling data; triangles: field cooling data; solid lines: guide to the eye).

temperature is lowered, but it also has a bump that appears between 10 and 35 K shown clearly in the inset. Fig. 3.4 (b) shows the inverse susceptibility of $Gd_2Mo_2O_{7-\delta}$. The deviation from the CW law occurs around 100 K and from a fit to the higher temperature data one obtains the values of Θ and p_{eff} of 25.9 K and 8.3 μ_B per $GdMoO_{3.5-\delta/2}$, respectively (the expected free Gd^{3+} ion effective moments are 8.0 μ_B[6]). The susceptibility of the $Gd_2Mo_2O_{7-\delta}$ crystal shown in Fig. 3.4 (c) is similar to that of $Sm_2Mo_2O_{7-\delta}$ and shows that some spins at the Mo ion sites are frozen below 25 K.

Fig. 3.5 (a) shows the DC resistivity of the $Ho_2Mo_2O_{7-\delta}$ crystal. It has an activated semiconductive behavior which is clearly shown in the inset of $\ln[\rho(T)]$ against $1000/T$. The activation energy, E_a, deduced from the slope is 35 meV. The inverse susceptibility of the $Ho_2Mo_2O_{7-\delta}$ crystal up to room temperature is shown in Fig. 3.5 (b). It adheres to the CW law down to 20 K. The values of Θ and p_{eff} were found to be -1.3 K and 10.9 μ_B per $HoMoO_{3.5-\delta/2}$, respectively (the expected free Ho^{3+} ion effective moments are 10.4 μ_B[6]). Fig. 3.5 (c) shows the susceptibility of $Ho_2Mo_2O_{7-\delta}$ which suggests that a spin-glass state develops below 20 K.

3. 2. Optical Properties of $R_2Mo_2O_{7-\delta}$ (R=Sm, Gd and Ho)

The reflectance of the single crystals $R_2Mo_2O_{7-\delta}$ (R=Sm, Gd, and Ho) were measured from 30 to 8000 cm^{-1} at temperatures between 10 and 300 K and from 3800 to 40,000 cm^{-1} at room temperature. In the following three subsections the optical properties of $Sm_2Mo_2O_{7-\delta}$, $Gd_2Mo_2O_{7-\delta}$ and $Ho_2Mo_2O_{7-\delta}$ are presented successively.

3.2.1. $Sm_2Mo_2O_{7-\delta}$

Fig. 3.6 shows the far-infrared reflectance spectra of $Sm_2Mo_2O_{7-\delta}$ at five temperatures. All spectra have phonon peaks superimposed on a background showing a characteristic metallic decrease of reflectance with frequency. As the temperature is reduced the reflectance increases systematically for all but the 10 K data. Its reflectance is higher than the 40 K data only for frequencies below 150 cm^{-1}. Fig. 3.7 shows the room-temperature reflectance of $Sm_2Mo_2O_{7-\delta}$ up to 40,000 cm^{-1}. It decreases smoothly with frequency up to 10,000 cm^{-1}, followed by an increase due to the presence of a broad peak centered at 30,000 cm^{-1}. At low frequencies the Hagen-Rubens approximation $R = 1 - A\sqrt{\omega}$ was used to extrapolate the reflectance, where A is a constant determined by the value of the reflectance at the lowest experimental frequency. The room-temperature reflectance between 700 to 40,000 cm^{-1} was used to extend the low temperature reflectance spectra. This extrapolation does not significantly alter the low frequency conductivity since the slopes of the low temperature spectra are similar to that of the room-temperature data. Beyond 40,000 cm^{-1} the reflectance was extrapolated using an ω^{-4} frequency dependence. A different high-frequency extrapolation has little effect on the optical conductivity at low frequencies (see a detail discussion in the next subsection). Fig. 3.8 shows the room-temperature optical conductivity of $Sm_2Mo_2O_{7-\delta}$ obtained from Kramers-Kronig analysis. Note that there is a broad absorption peak centered at 25,000 cm^{-1} which is associated with the reflectance peak around 30,000 cm^{-1}. It is assigned as an interband transition between the lower valence band and the conduction band. This will be discussed in more detail later on.

The conductivity of $Sm_2Mo_2O_{7-\delta}$ at far-infrared frequencies is shown in Fig. 3.9. The overall conductivity consists of two components: (1) the sharp phonon absorption

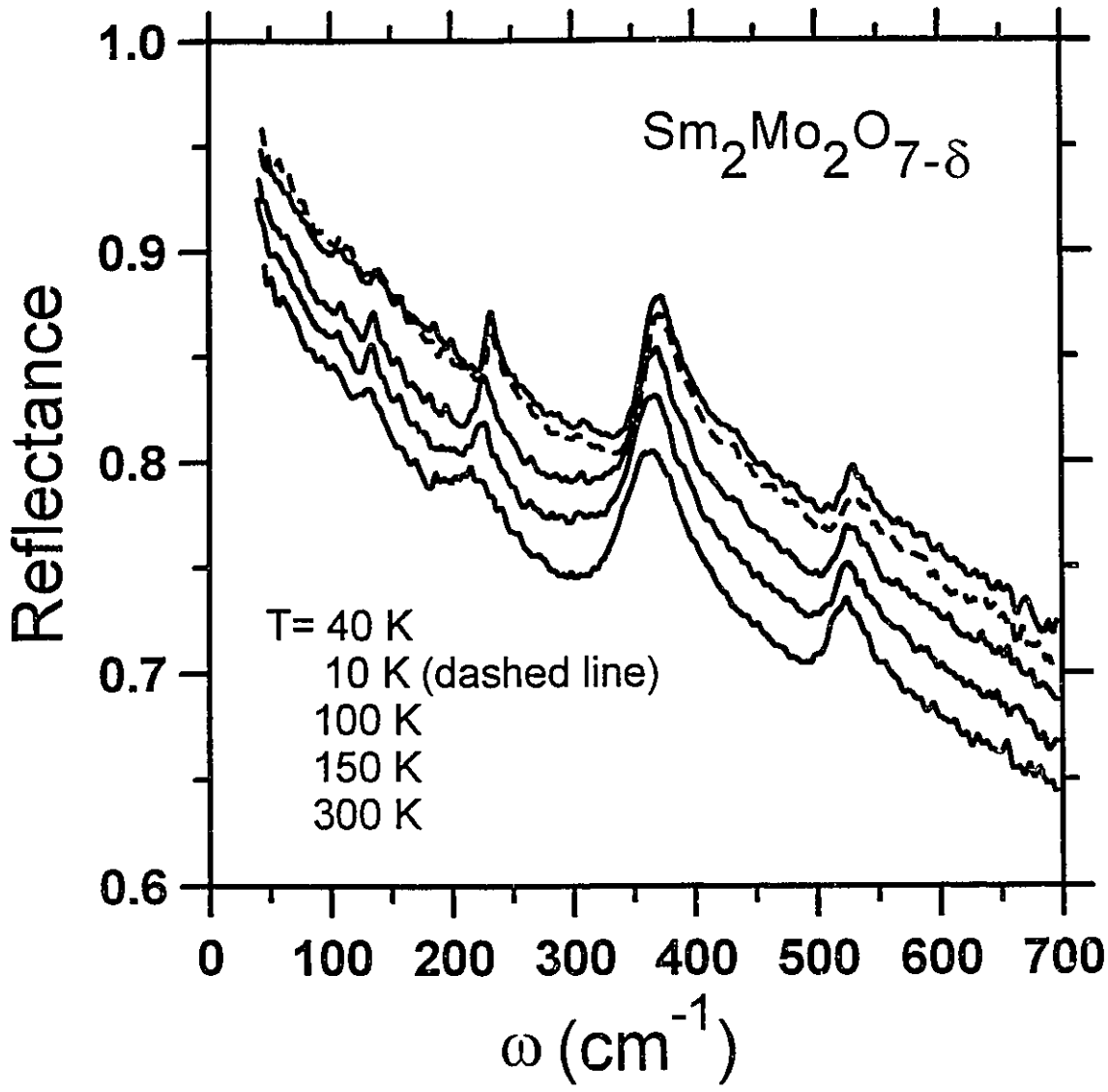

Figure 3.6. Reflectance of $Sm_2Mo_2O_{7-\delta}$ at far-infrared frequencies at 10 (dashed line), 40, 100, 150 and 300 K (from top to bottom).

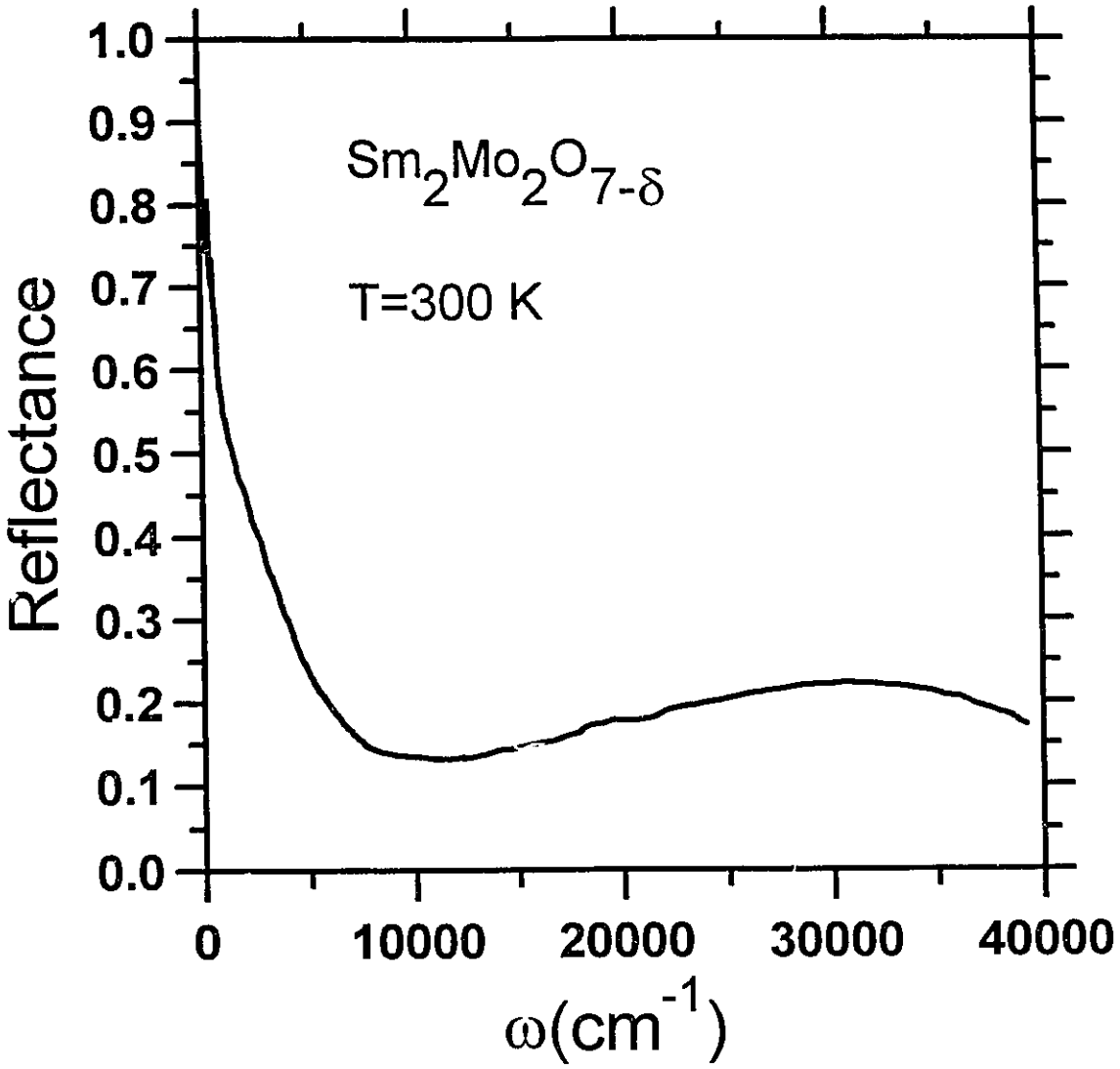

Figure 3.7. Room-temperature reflectance of $Sm_2Mo_2O_{7-\delta}$ up to 40,000 cm^{-1}.

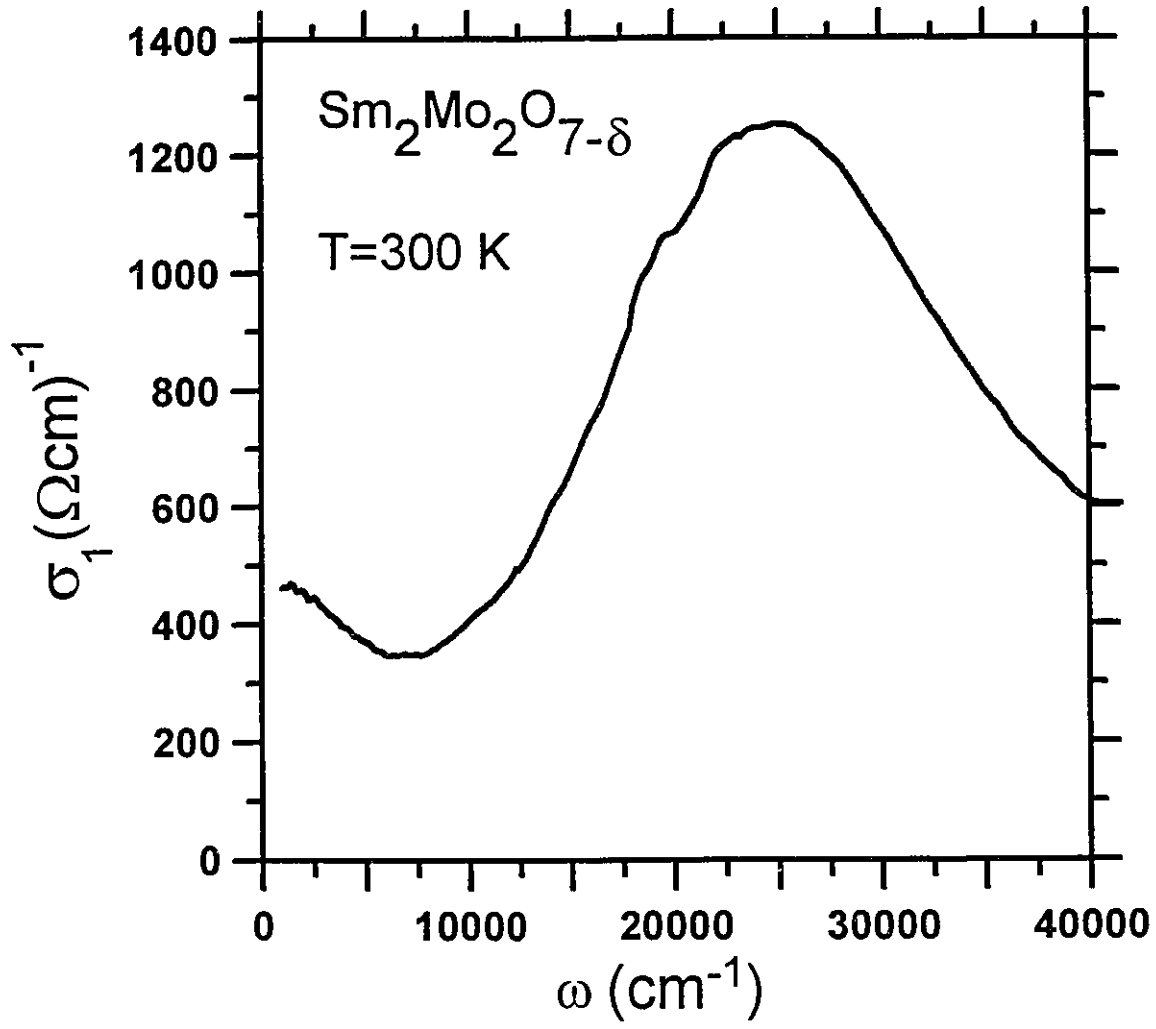

Figure 3.8. Real part of the AC conductivity of $Sm_2Mo_2O_{7-\delta}$ at 300 K as a function of frequency up to 40,000 cm^{-1}.

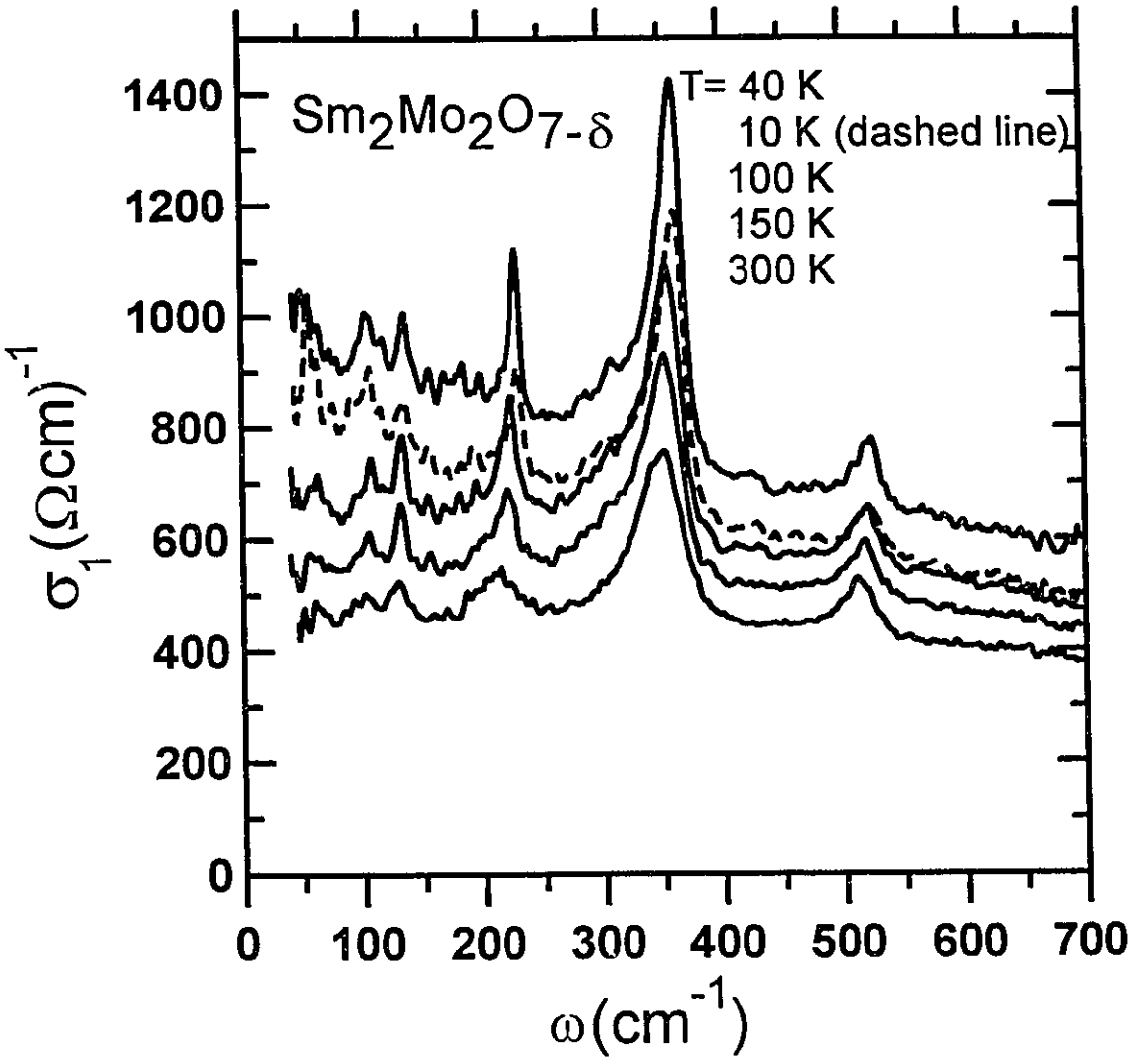

Figure 3.9. Real part of the far-infrared AC conductivity of $Sm_2Mo_2O_{7-\delta}$ at 10 (dashed line), 40, 100, 150, 300 K (from top to bottom).

peaks and (2) the continuum background. To isolate the continuum background in $\sigma_1(\omega)$ the phonon lines were fit to Fano lineshapes (see Appendix B)[20], in which the interaction between phonon and electronic continuum is taken into account, with the baseline fit to constant, linear, and quadratic terms as shown in the following formula:

$$\sigma_1(\omega) = a + b\omega + c\omega^2 + \sum_{i=1}^{n} d_i \frac{(x_i + q_i)^2}{1 + x_i^2}, \tag{3.3}$$

where $x_i = \frac{\omega - \omega_i}{\gamma_i}$, a, b, and c are constants, n is the total number of the phonon lines, ω_i, γ_i, and d_i are the position, width, and strength parameters of the i^{th} phonon, respectively, and q_i describes how asymmetric the i^{th} phonon is. Note that the Fano lineshape will be symmetric if $q_i >> x_i$. The fitting parameters of the Fano lineshapes for $Sm_2Mo_2O_{7-\delta}$ are listed in Table 3.1. There are six phonon modes in $\sigma_1(\omega)$ (the lowest frequency mode in the 100, 150 and 300 K data is very weak). All modes except the one at 345 cm^{-1} are symmetric. Little temperature dependence was found in the 101, 129, and 510 cm^{-1} modes. The 210 cm^{-1} mode narrows and hardens at low temperatures. The 345 cm^{-1} mode is symmetric at room temperature. At lower temperatures it becomes asymmetric, *i.e.*, the absolute value q decreases, and hardens.

The phonon fits were used to subtract their contribution from the total conductivity, leaving only the background conductivity $\sigma_1^b(\omega)$ shown in Fig. 3.10 together with the Drude conductivity fit (Eqn. 2.18) as shown in the dashed-dotted lines. The DC conductivity of the $Sm_2Mo_2O_{7-\delta}$ crystal at 300 K is shown as a filled square on the left vertical axis. There is a nearly 150 $\Omega^{-1}cm^{-1}$ difference between the DC conductivity and the extrapolated value. We think that, instead of being caused by the

choice of the high-frequency reflectance extrapolation and its influence on the far-infrared optical conductivity, this discrepancy is caused by an error in the DC resistivity measurement due to the irregular shape of the sample which results in the error in the thickness of the sample. Note that $\sigma_1^b(\omega)$ at room temperature decreases only slightly with increasing frequency. This is characteristic of a poor metal with a broad Drude peak centered at zero frequency. As the temperature is lowered $\sigma_1^b(\omega)$ increases in an almost Drude-like manner. It is noted that the low-temperature ($T \leq 100$ K), fitted Drude conductivity curve deviates slightly from the experimental data below 120 cm^{-1} which may be due to the scattering rate being weakly frequency dependent in this frequency range. A conductivity anomaly occurs in the 10 K data where $\sigma_1^b(\omega)$ shifts *downward* in comparison to the 40 K data. This unusual behavior is in accord with the DC resistivity of $Sm_2Mo_2O_{7-\delta}$ which shows a resistive minimum at 40 K. Fig. 3.11 shows the resulting temperature dependence of the Drude parameters. The scattering rate $\gamma_D(T)$ gently decreases as the temperature is lowered from 300 to 150 K. At lower temperatures it drops sharply until it finally saturates for temperatures below 40 K. Above 150 K the slope of $\gamma_D(T)$ results from phonons and one gets λ=0.19, which is a reasonable value, using the formula $\gamma_D(T) = 2\pi\lambda k_B T$, where λ is the electron-phonon coupling constant, that describes the scattering of conduction electrons by phonons. The scattering of conduction electrons from the short-range ordered Mo ions, which sets in at about 150 K, causes the sharp decrease of $\gamma_D(T)$ between 150 and 40 K. This is supported by the susceptibility of $Y_2Mo_2O_{7-\delta}$, with non-magnetic moments for the Y^{3+} ion, that shows the deviations from the CW law below 80 K which was attributed to the short-range magnetic correlation of Mo^{4+}.[11] The fact that in the temperature range of 40 to 150 K the behavior of $\gamma_D(T)$ is similar to that of the DC resistivity of $Sm_2Mo_2O_{7-\delta}$ implies that the sharp decrease in the scattering rate gives rise to the steep drop in the DC resistivity. If this picture is correct, the saturation of $\gamma_D(T)$ below 40 K is due to the freezing of moments

Table 3.1. The parameters used in Eqn. 3.3 to fit the optical conductivity $\sigma_1(\omega)$ of $Sm_2Mo_2O_{7-\delta}$ from 40 to 700 cm^{-1}. The units for a, b, and c are $\Omega^{-1}cm^{-1}$, Ω^{-1}, and $\Omega^{-1}cm$, respectively; the units for ω_i, γ_i, and d_i are cm^{-1}, cm^{-1}, and $\Omega^{-1}cm^{-1}$, respectively; q_i is unitless. Here, i refers to the i^{th} phonon.

Mode	T(K)				
	300	150	100	40	10
a	467.6	521.4	631.6	886.5	768.0
b	-0.1711	0.06148	-0.03836	-0.4528	-0.3797
c	0.00007385	-0.0002644	0.0002781	-.00002560	-.00004332
ω_1				49.57	55.32
γ_1				9.506	5.047
d_1				2.303	2.358
q_1				7.500	10.10
ω_2	100.9	104.2	107.4	106.1	104.2
γ_2	9.156	6.470	4.051	7.909	11.03
d_2	0.04708	0.02523	0.01671	0.002293	0.002467
q_2	29.04	47.67	68.12	217.5	218.6
ω_3	128.6	131.3	132.4	135.4	134.3
γ_3	7.187	4.025	3.666	4.336	3.857
d_3	0.02837	0.1316	0.007474	0.0009105	0.0006771
q_3	48.86	29.64	132.7	358.8	360.5

ω_4	209.4	218.7	222.0	228.3	229.0
γ_4	23.25	9.128	6.567	3.739	4.659
d_4	0.3362	0.05133	0.01656	0.005871	0.004547
q_4	16.51	49.10	105.9	222.4	203.5
ω_5	345.0	353.0	357.0	362.0	362.0
γ_5	24.96	19.89	16.96	12.56	13.55
d_5	0.09563	9.507	21.34	29.03	17.64
q_5	58.56	-6.450	-4.729	-4.797	-5.518
ω_6	509.7	519.3	520.1	523.1	522.7
γ_6	19.86	16.18	14.65	11.21	14.07
d_6	0.05322	1.551	1.317	0.9744	0.5442
q_6	45.52	-8.181	-9.114	-11.03	-12.74

on the Mo ions.

It is noted that the overall scattering rate of $Sm_2Mo_2O_{7-\delta}$ is quite large, much larger than what is seen in conventional metals, but it is comparable with that of other magnetic systems such as chromium [γ_D(300 K)≈340 cm^{-1}], URu_2Si_2 [γ_D(90 K)≈3000 cm^{-1}], and UNi_2Si_2 [$\gamma_D(T)$≈500 cm^{-1} at 140 K in the basal plane and 800 cm^{-1} at 300 K along the c-axis].[21, 22, 23] Also note that the overall scattering rate of $Sm_2Mo_2O_{7-\delta}$ consists of two components: the temperature-dependent one, which has been discussed before, having phonon and magnetic origins, and the temperature-independent background which is associated with the large temperature-independent component of the DC resistivity of $Sm_2Mo_2O_{7-\delta}$. The origin of this background is not clear. However, the fact that there is always some large temperature-independent component in the DC resistivity

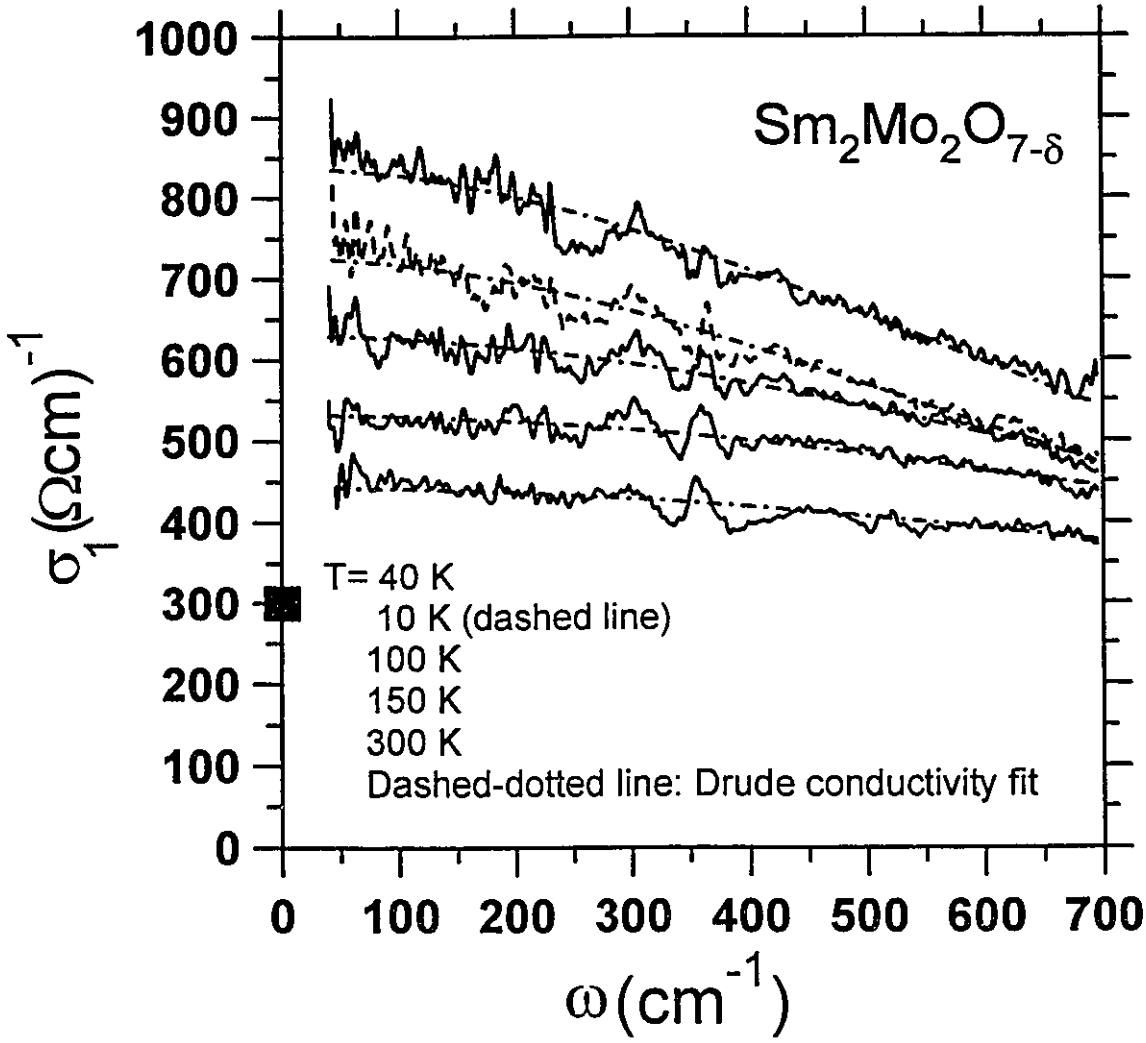

Figure 3.10. Background AC conductivity of $Sm_2Mo_2O_{7-\delta}$ obtained by subtracting the phonon absorption peaks from the overall conductivity at each temperature. The dashed-dotted lines are the Drude conductivity fit with the parameters shown in Fig. 3.11. The value of the DC conductivity of $Sm_2Mo_2O_{7-\delta}$ at 300 K is shown as a filled square on the left vertical axis.

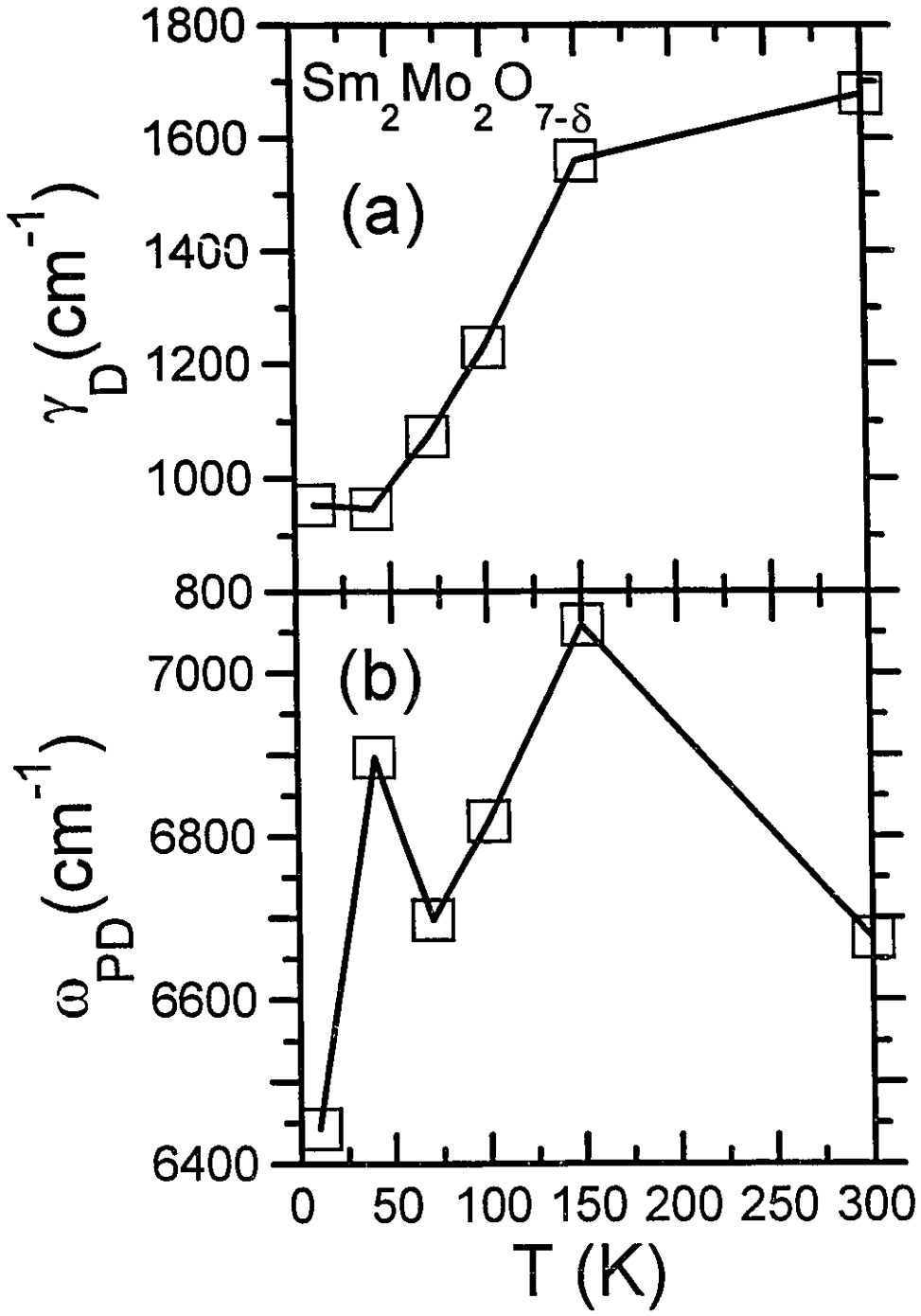

Figure 3.11. (a) The temperature dependence of the scattering rate of $Sm_2Mo_2O_{7-\delta}$; **(b)** The temperature dependence of the plasma frequency of $Sm_2Mo_2O_{7-\delta}$. Both of them are found by fitting the background conductivity in Fig. 3.10 to the Drude conductivity formula in Eqn. 2.18. Solid lines are guides to the eye.

of conventional metallic spin-glass materials suggests that it might be related to impurity scattering.[14]

The Drude plasma frequency $\omega_{PD}(T)$ increases slightly as the temperature is lowered from 300 to 150 K. It then drops from 150 to 70 K and another maximum appears at 40 K. Finally, it drops again from 40 to 10 K. The decrease of $\omega_{PD}(T)$ from 40 to 10 K gives rise to an increase in the DC resistivity and a decrease in the AC conductivity in the same temperature range. The slight increase in the DC resistivity from 300 to 150 K cannot be explained by the optical results, which suggest that the resistivity *decreases* in this temperature range. It should be noted that a room-temperature carrier density of 5.0×10^{20} cm^{-3} is deduced from the plasma frequency, assuming that the effective mass of the conduction electrons is equal to that of the free electron. This value is characteristic of a poor metal.

The behavior of $\gamma_D(T)$, which mainly has a magnetic origin, can be understood in terms of a picture of the temperature dependence of the spin correlation function $\langle S(0)S(r)\rangle$ of the Mo ions, where r is the spacing between two nearest-neighbor Mo ions. The correlation function is quite small at high temperatures due to thermal fluctuations, begins to increase as the temperature is reduced to the value of the exchange integral, J, which is proportional to the Curie temperature Θ(=110 K), and saturates as spins on the Mo ion sites are frozen below T_f. Therefore, the scattering experienced by conduction electrons from the magnetic Mo ions is incoherent at high temperatures, becomes more and more coherent as the correlation develops, and, finally, reaches a constant value as a result of the saturation of the spin correlation.

At this stage it is unclear why the DC resistivity of $Sm_2Mo_2O_{7-\delta}$ shows the upturn below 40 K. One possibility could be a pseudo-gap opened at the Fermi surface with an energy scale below our experimental limit. The decrease in the plasma frequency in this temperature region might mean a reduction in the free-carrier density provided that the effective mass of free carriers is constant. It is also possible that the upturn is due to the Kondo effect with spin exchanges between Sm ions and conduction electrons. It is an open question whether or not there is a physical connection between the DC resistivity anomaly and the spin frustrations in the spin-glass state.

3.2.2. $Gd_2Mo_2O_{7-\delta}$

The temperature dependent far-infrared reflectance of $Gd_2Mo_2O_{7-\delta}$ is shown in Fig. 3.12. The room-temperature spectrum is similar to that of $Sm_2Mo_2O_{7-\delta}$, in that there are some phonon peaks superimposed on a background reflectance that decreases with frequency. In contrast to $Sm_2Mo_2O_{7-\delta}$ the overall reflectance of $Gd_2Mo_2O_{7-\delta}$ decreases as the temperature is lowered. However, this result is consistent with the DC resistivity measurement which shows an increasing resistivity as the temperature is lowered. Note that an anomaly occurs in the 25 K data. When comparing it to either the 10 K or 100 K data it is apparent that the reflectance is higher at low frequencies and lower at high frequencies. Fig. 3.13 shows the room-temperature reflectance of $Gd_2Mo_2O_{7-\delta}$ up to 40,000 cm^{-1}. The reflectance decreases with frequency up to 10,000 cm^{-1} where it turns up and has a peak centered at 35,000 cm^{-1}. The extrapolations used for Kramers-Kronig analysis were the same as those used for $Sm_2Mo_2O_{7-\delta}$. We also used the published high-frequency reflectance data of $Gd_2(MoO_4)_3$ from Mamedov and Zejnally[85] to extend the experimental data up to 2.5×10^5 cm^{-1}. The discrepancy of the optical conductivity at low frequencies, obtained from Kramers-Kronig analysis, using the different extrapolations

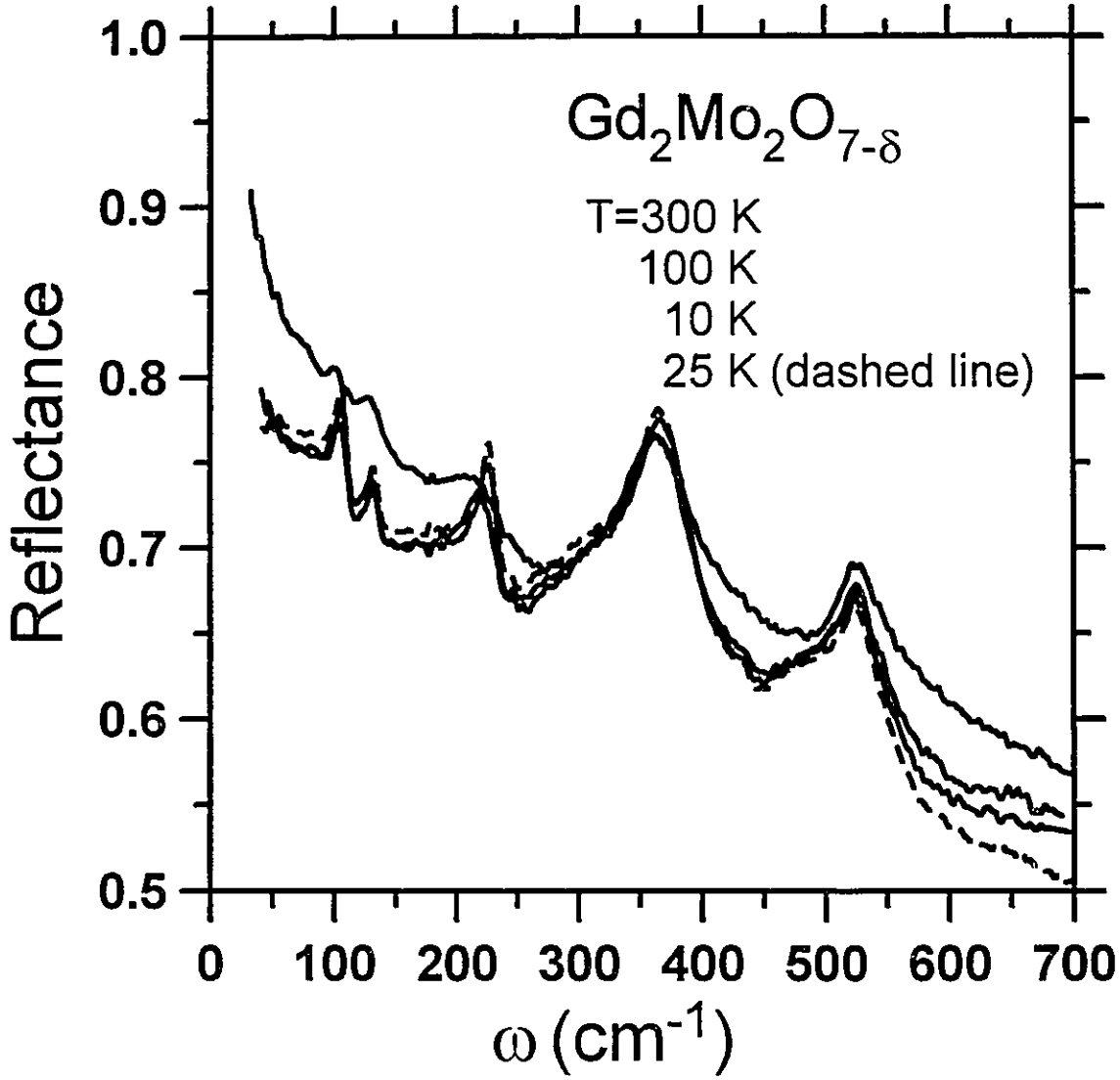

Figure 3.12. Reflectance of $Gd_2Mo_2O_{7-\delta}$ in the far-infrared region at 300, 100, 25 (dashed line), and 10 K (from top to bottom).

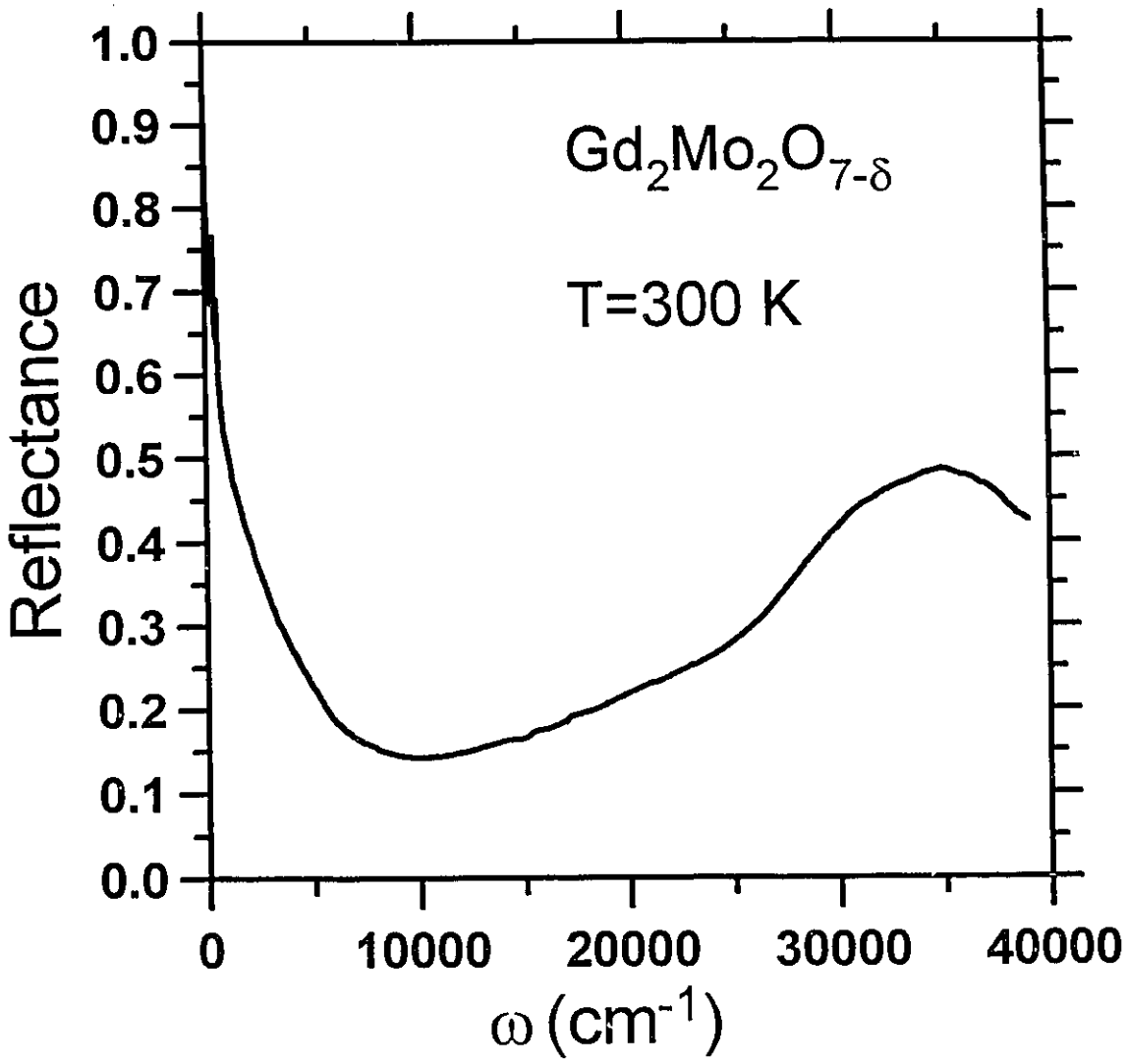

Figure 3.13. Reflectance of $Gd_2Mo_2O_{7-\delta}$ at 300 K up to 40,000 cm^{-1}.

is much small (~2% at 40 cm^{-1}; ~5% at 700 cm^{-1}; ~2% at 5000 cm^{-1}).The resulting room-temperature conductivity up to 35,000 cm^{-1} is shown in Fig. 3.14. As is the case with $Sm_2Mo_2O_{7-\delta}$ there exists a strong interband-transition peak centered at near 27,500 cm^{-1}.

Fig. 3.15 shows the temperature dependent far-infrared optical conductivity of $Gd_2Mo_2O_{7-\delta}$. Excluding the 25 K data, it consists of phonon peaks superimposed on a continuum background which decreases in strength as the temperature is reduced. This behavior is different from that of $Sm_2Mo_2O_{7-\delta}$ at low temperatures. As is the case for $Sm_2Mo_2O_{7-\delta}$ Eqn. 3.3 was used to fit $\sigma_1(\omega)$ allowing a separation of the phonon and background contributions to the conductivity. The fitting parameters for $Gd_2Mo_2O_{7-\delta}$ are listed in Table 3.2.

The background conductivity $\sigma_1^b(\omega)$ of $Gd_2Mo_2O_{7-\delta}$ at 300, 100, 25, and 10 K is shown in Fig. 3.16. Also shown is the DC conductivity of $Gd_2Mo_2O_{7-\delta}$ at 100 and 300 K. Note that the room-temperature DC conductivity is nearly 100 $\Omega^{-1}cm^{-1}$ smaller than the extrapolated value at ω=0 cm^{-1}. Again, we think that the discrepancy is due to the error in the DC resistivity measurement (see the explanation in subsection 3.2.1). Also note that the room-temperature conductivity increases slightly with frequency. At low temperatures a conductivity depression occurs below 400 cm^{-1}. The conductivity behavior of $Gd_2Mo_2O_{7-\delta}$ ($\delta \cong 0.22$ for the single crystal[30]) can be understood in terms of Anderson localization (see Appendix C). The reason for using the Anderson localization to interpret the experiment result can been seen clearly in section 3.3 in terms of the band structure. In this model the Fermi level E_F is in the region of the density of states where the states are localized and DC conductivity is induced by excitations of conduction electrons to the mobility edge E_c, which separates localized states from extended states. The almost frequency-independent AC conductivity at room temperature is due to optical

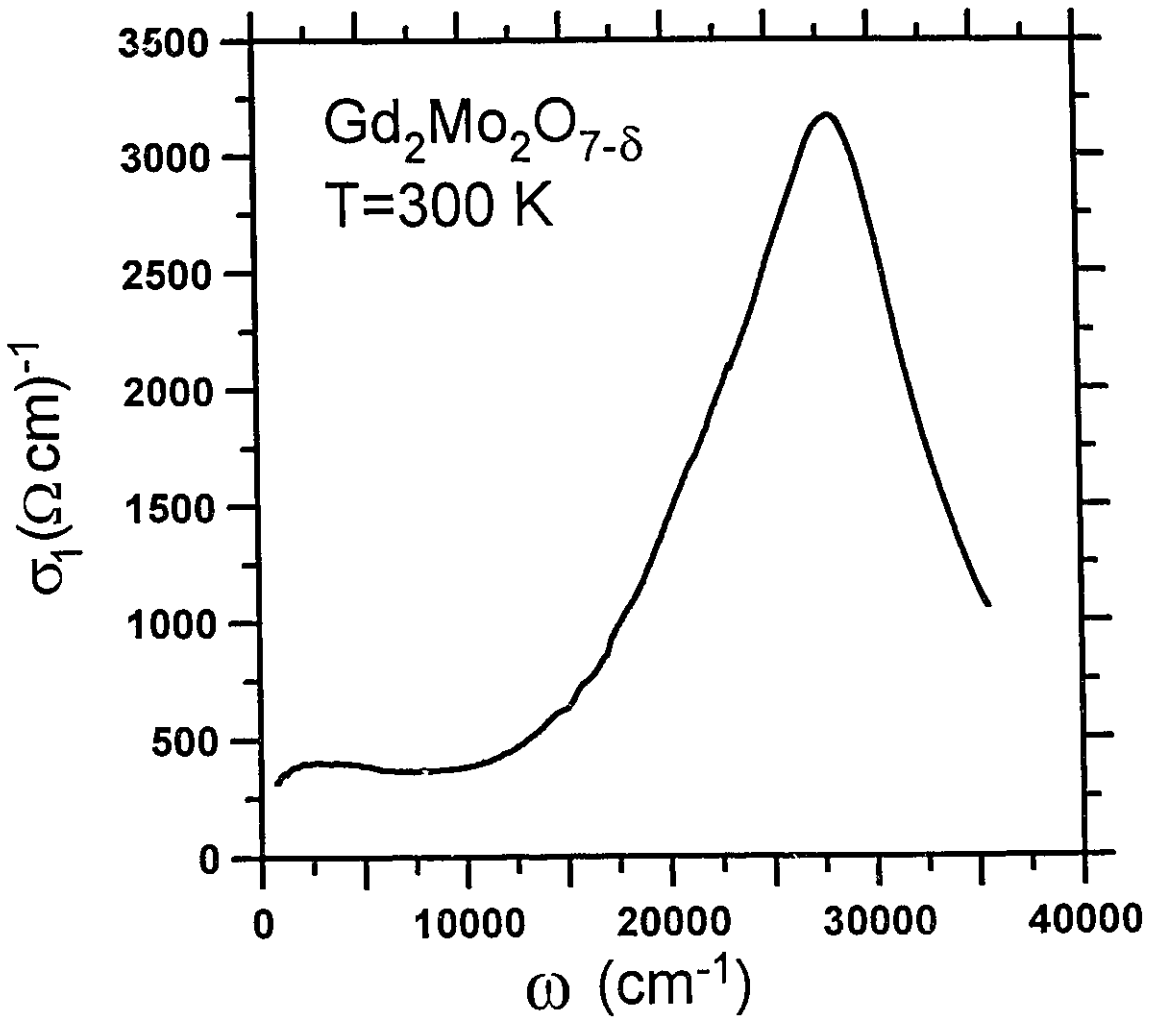

Figure 3.14. Real part of the AC conductivity of $Gd_2Mo_2O_{7-\delta}$ at 300 K as a function of frequency up to 35,000 cm^{-1}.

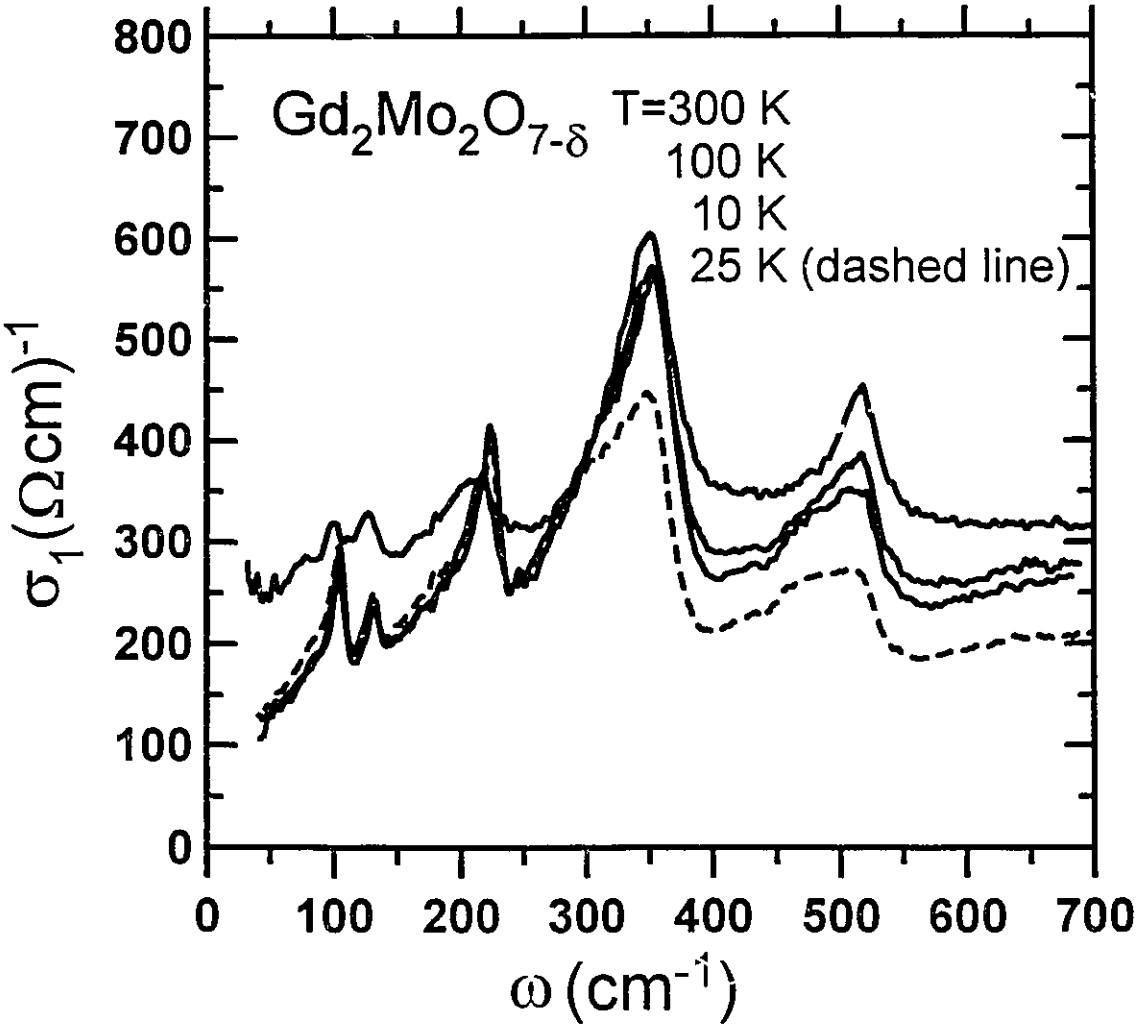

Figure 3.15. Real part of the far-infrared AC conductivity of $Gd_2Mo_2O_{7-\delta}$ as a function of frequency at 300, 100, 25 (dashed line), and 10 K (from top to bottom).

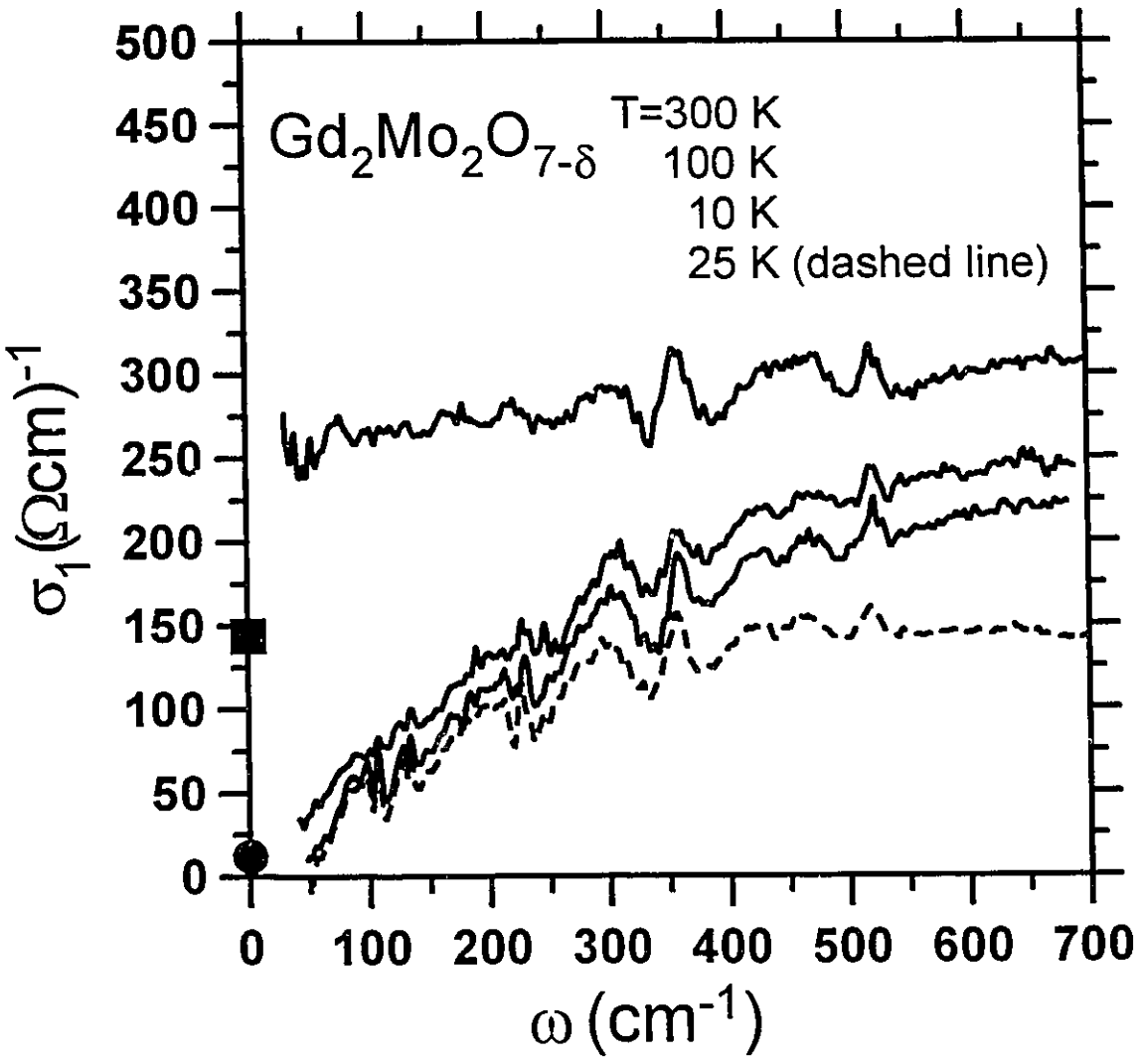

Figure 3.16. Background AC conductivity of $Gd_2Mo_2O_{7-\delta}$ which is obtained by subtracting the phonon peaks from the overall conductivity shown in Fig. 3.15 at 300, 100, 25 (dashed line), and 10 K (from top to bottom). The values of the DC conductivity of $Gd_2Mo_2O_{7-\delta}$ at 300 and 100 K are shown on the left vertical axis as a filled square and circle, respectively.

Table 3.2. The parameters used in Eqn. 3.3 to fit the optical conductivity $\sigma_1(\omega)$ of $Gd_2Mo_2O_{7-\delta}$ from 40 to 700 cm^{-1}. Here a, b, and c are in the units of $\Omega^{-1}cm^{-1}$, Ω^{-1}, and $\Omega^{-1}cm$, respectively, ω_i, γ_i, and d_i are in the units of cm^{-1}, cm^{-1}, and $\Omega^{-1}cm^{-1}$, respectively, and q_i is unitless. Here, i refers to the i^{th} phonon.

Mode	T(K)			
	300	100	25	10
a	254.9	12	0	0
b	0.1014	0.6765	0.5542	0.6125
c	-0.00003808	-0.0004873	-0.0005123	-0.0004209
ω_1	98.79	104.4	104.0	104.4
γ_1	9.861	5.411	4.361	4.683
d_1	0.1422	1.924	2.165	1.141
q_1	17.45	-6.627	-6.977	-10.03
ω_2	125.8	130.3	130.6	131.4
γ_2	7.777	4.370	2.271	2.496
d_2	0.0168	1.611	0.001788	0.05532
q_2	53.44	-5.571	-155.7	-29.52
ω_3	203.9	220.0	225.0	225.4
γ_3	23.87	11.25	7.879	7.388
d_3	0.1368	10.92	14.35	10.33
q_3	23.53	-3.316	-3.051	-3.918

ω_4	345.0	356.1	357.7	359.5
γ_4	29.09	28.32	31.72	27.86
d_4	0.1329	24.53	56.23	40.71
q_4	47.96	-3.511	-1.911	-2.683
ω_5	511.8	521.5	518.9	519.6
γ_5	24.67	28.50	33.38	34.34
d_5	0.08234	23.72	30.02	27.68
q_5	40.25	-2.203	-1.509	-1.976

excitations of those electrons which have been thermally activated to E_c and, therefore, behaves like a poor metal. The hopping conductivity has been studied by Mott and Davis. They have given an expression describing the temperature and frequency dependence of $\sigma_1(\omega)$.[24] The linear-dependent conductivity with frequency up to 400 cm^{-1} displayed by $Gd_2Mo_2O_{7-\delta}$ at 100, 25, and 10 K is in agreement with the theory of Mott and Davis and is due to the optically activated hopping of conduction electrons within localized states. It should be pointed out that such a hopping conduction process has been found in the far-infrared absorption spectrum of the neutron-transmutation-doped germanium in which a non-periodic potential field is set up.[25]

Mott pointed out that for Anderson localization the DC conductivity behaves as $\cong \sigma_0 \exp\left[-(E_c - E_F)/k_B T\right]$ at high temperatures and $\cong \sigma_1 \exp\left[-(Q/k_B T)^{0.25}\right]$ (the variable-range hopping conductivity) at sufficiently low temperatures, where $Q = 1.5\alpha^3 / N(E_F)$, $N(E_F)$ is the density of states at E_F and α represents the fall-off rate of the envelope of the wave function $\phi \propto \exp(-\alpha r)$.[26] This behavior has been observed in the $(Dy_xY_{1-x})_2Mo_2O_7$ pyrochlore materials by Raju and Rangarajan.[27] The following formula,

$$\sigma = \sigma_0 \exp\left[-(E_c - E_F)/k_B T\right] + \sigma_1 \exp\left[-(Q/k_B T)^{0.25}\right], \qquad (3.4)$$

was used to fit the DC conductivity of $Gd_2Mo_2O_{7-\delta}$. Fig. 3.17 shows the result of the fit together with the DC conductivity data. The fit is good at high and very low temperatures ($T \leq 25$ K), but it does not agree with the experimental data at intermediate temperatures. The resulting parameters are σ_0=678 Ω^{-1}cm^{-1}, E_c-E_F=324 cm^{-1}, σ_1=1.81 Ω^{-1}cm^{-1}, and Q=1.70 cm^{-1}. Comber *et al.* studied the transport properties of amorphous Si films which is another Anderson localization system.[28] In their studies the temperature dependence of the DC conductivity was divided into three regions: from room temperature to the temperature T_1 the conductivity is due to thermal excitations of carriers to the mobility edge with an activation energy E_c-E_F; the slope of $\ln\left[\sigma_{DC}(T)\right]$ against $1/T$ changes at T_1. Between T_1 and T_2 the conductivity takes place through phonon-assisted hopping within the localized states and is still activated but with a smaller energy E_x-E_F+W_e, where E_x is the energy around which hopping occurs and W_e is the hopping energy; for $T<T_2$, E_x approaches E_F and W_e decreases as the temperature is lowered. As E_x approaches E_F the conductivity is proportional to $\exp\left[-(Q/k_B T)^{0.25}\right]$.

The DC conductivity of $Gd_2Mo_2O_{7-\delta}$ can also be divided into three regions: the high temperature region between room temperature and T_1 (≈180 K), in which E_c-E_F=324 cm^{-1}, the intermediate temperature region between T_1 and T_2 (≈25 K) where the slope of $\ln\left[\sigma_{DC}(T)\right]$ *vs.* $1/T$ decreases continuously, and the low temperature region for $T<T_2$ where the conductivity is described by variable-range hopping. The difference between $Gd_2Mo_2O_{7-\delta}$ and amorphous Si film is that the slope is not constant for $Gd_2Mo_2O_{7-\delta}$ in the intermediate temperature region which indicates that the movement of E_x towards E_F and the drop of W_e have already taken place in this region. This could be

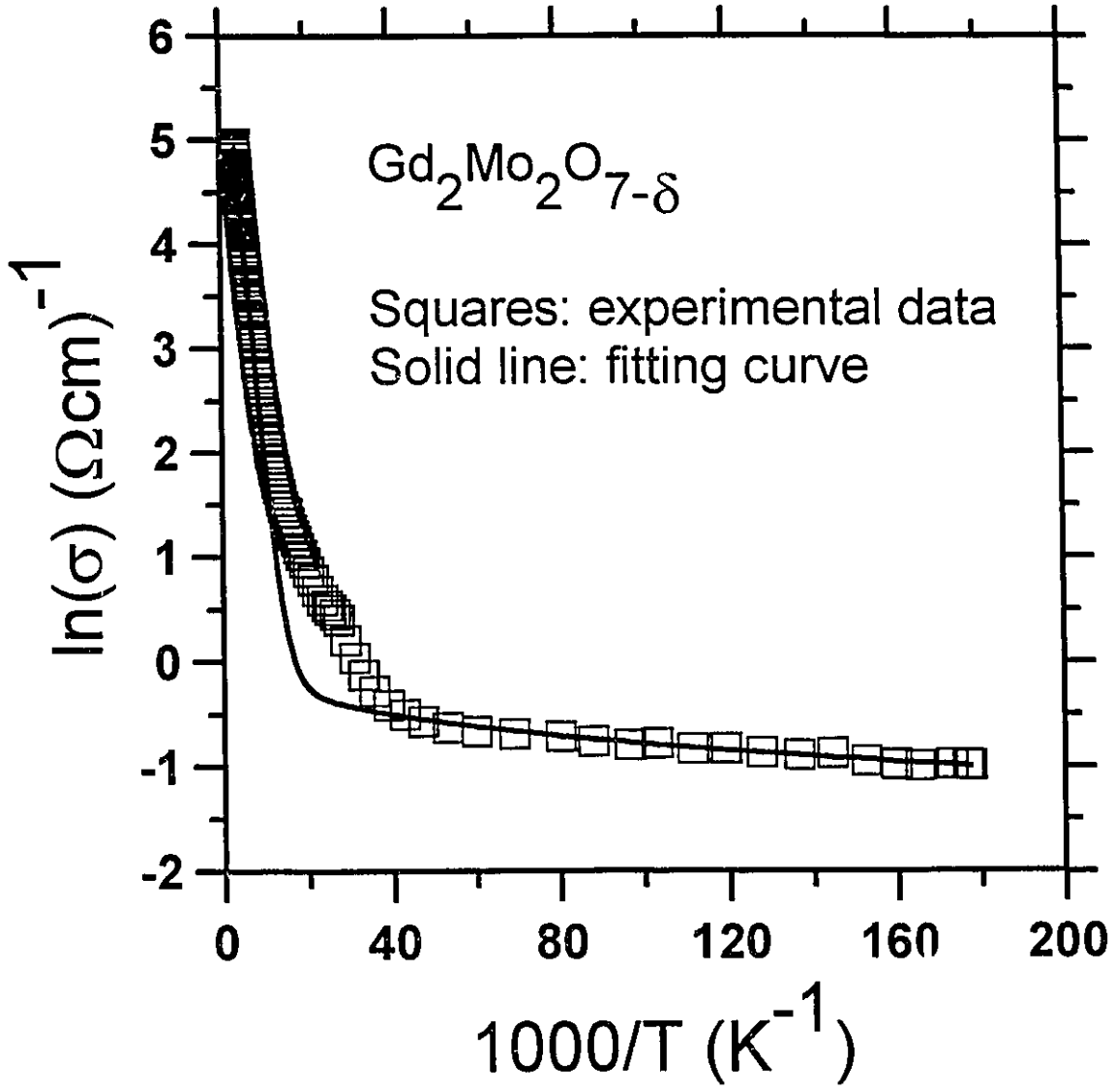

Figure 3.17. Logarithmic DC conductivity of $Gd_2Mo_2O_{7-\delta}$ as a function of $1000/T$ shown as squares. The solid line is the fitting curve using Eqn. 3.4 in the text.

caused by a magnetic interaction between conduction electrons and magnetically short-range ordered Mo ions. Our far-infrared optical results shown in Fig. 3.16 support this interpretation. The almost flat AC conductivity at 300 K results from optical excitations of conduction electrons in the extended states just above E_c, whereas at low temperatures the conductivity begins to be depressed at 400 cm^{-1}, which is roughly equal to the value of E_c-E_F given above, and this is caused by the optically activated hopping of electrons in the localized states below E_c. Using the fitted Q and assuming α^{-1}=10 Å, the same order of the lattice constant a (≈10 Å), then one gets $N(E_F)\approx 4\times 10^{23}$ $cm^{-3}eV^{-1}$, a reasonable value slightly higher than that of a typical semimetal.

It should be noted that there is a conductivity anomaly in the 25 K data: $\sigma_1^{\,b}(\omega)$ at this temperature is lower than that at 10 K. As mentioned earlier there is a bump in the DC resistivity between 10 and 35 K. Also, a Curie temperature of 26 K is deduced from fitting the high-temperature susceptibility data. These two observations suggest that there might be another scattering process around 25 K which has a magnetic origin. We believe that this extra scattering is responsible for the presence of the AC conductivity anomaly at 25 K and may be caused by spin frustrations which exist in the spin-glass state around 25 K.

At room temperature $Gd_2Mo_2O_{7-\delta}$ has 5 symmetric phonon modes at 99, 126, 204, 345, and 512 cm^{-1}. As the temperature is reduced the phonon line shapes become asymmetric which is quantified by the dramatic reduction in the absolute value of the parameter q (the only exception is the 126 cm^{-1} mode at 10 and 25 K). The 99, 126, and 204 cm^{-1} modes narrow and the 10 K data shows that the mode positions shift to 104, 131, and 225 cm^{-1}, respectively. The width of the 345 cm^{-1} mode does not change as the temperature is reduced to 10 K, but it does shift to 360 cm^{-1}. The 512 cm^{-1} mode

becomes broader and hardens to 520 cm^{-1}. In Fano's paper the width of the resonance, 2γ, is equal to $2\pi|V_E|^2$, where $|V_E|$ is the coefficient of the resonance-continuum (in our case the electron-phonon, e-p) interaction and the position of resonance is at $E = E_\varphi + F$, where E_φ is the position with $V_E = 0$ and $F(E) = P\int dE'|V_{E'}|^2/(E-E')$ which determines the shift of the position of the resonance.[20] The localization of the free carriers at low temperatures causes a reduction of e-p interaction and gives rise to the narrowing of the three lowest frequency modes. The increase of the e-p interaction for the 512 cm^{-1} mode at low temperatures leads to the widening of this mode. These two effects cancel each other out for the 345 cm^{-1} mode because at this frequency most of electrons at localized states are excited to the extended states above E_c. This accounts for its unchanged width. The shape of phonons can be understood qualitatively. According to the Fano's paper,[20]

$$q = \frac{\langle \Phi | T | i \rangle}{\pi V_E^* \langle \psi_E | T | i \rangle}, \tag{3.5}$$

where $\langle \Phi | T | i \rangle$ is the transition matrix element between an initial state i and the modified discrete state Φ, in which a real discrete state φ is admixed with states of the continuum, and $\langle \psi_E | T | i \rangle$ is another transition matrix element between the state i and the unperturbed continuum state ψ_E. We assume that the numerator in Eqn. 3.5 is a dominant factor in determining the value of q. At low temperatures electrons are localized and the conductivity results from phonon-assisted hopping so that the matrix element $\langle \Phi | T | i \rangle$ is much smaller, and, therefore, q is much smaller causing the phonon shape to be asymmetric. At room temperature conduction electrons in the extended region can be

optically excited to a higher energy level without phonon assistance and as a result $\langle \Phi | T | i \rangle$ becomes larger which leads to a symmetric phonon shape.

3.2.3. $Ho_2Mo_2O_{7-\delta}$

The frequency dependence of the reflectance of $Ho_2Mo_2O_{7-\delta}$ at 300, 100, 40, and 10 K is shown in Fig. 3.18. At far-infrared frequencies several phonons are superimposed on a smooth background reflectance that decreases with increasing frequency at each temperature. The overall reflectance decreases between 300 and 100 K and becomes temperature independent below 100 K. Unlike the $Sm_2Mo_2O_{7-\delta}$ and $Gd_2Mo_2O_{7-\delta}$ reflectance spectra, the $Ho_2Mo_2O_{7-\delta}$ spectrum shows a sharp drop at the end of the far-infrared region with a minimum at 700 cm^{-1}. This feature is independent of temperature and develops into a deep valley at low temperatures. Interestingly, a peak shows up near 2000 cm^{-1} which is absent in the reflectance spectra of $Sm_2Mo_2O_{7-\delta}$ and $Gd_2Mo_2O_{7-\delta}$ and changes slightly as the temperature is lowered. Fig. 3.19 shows the room-temperature reflectance spectrum up to 40,000 cm^{-1}. It exhibits a broad peak at high frequencies.

The temperature dependence of the optical conductivity of $Ho_2Mo_2O_{7-\delta}$, obtained from the Kramers-Kronig transformation using the same extrapolations as before, is displayed in Fig. 3.20. In far-infrared region, three phonons can be seen superimposed on a continuous background. The background becomes weaker as the temperature is lowered from 300 to 100 K and is independent of temperature below 100 K. The background conductivity is separated from phonons using the same procedure as the one used for $Sm_2Mo_2O_{7-\delta}$ and $Gd_2Mo_2O_{7-\delta}$. The fitting parameters of the Fano-lineshapes for $Ho_2Mo_2O_{7-\delta}$ are listed in Table 3.3. All phonon modes except the one at 225 cm^{-1} are

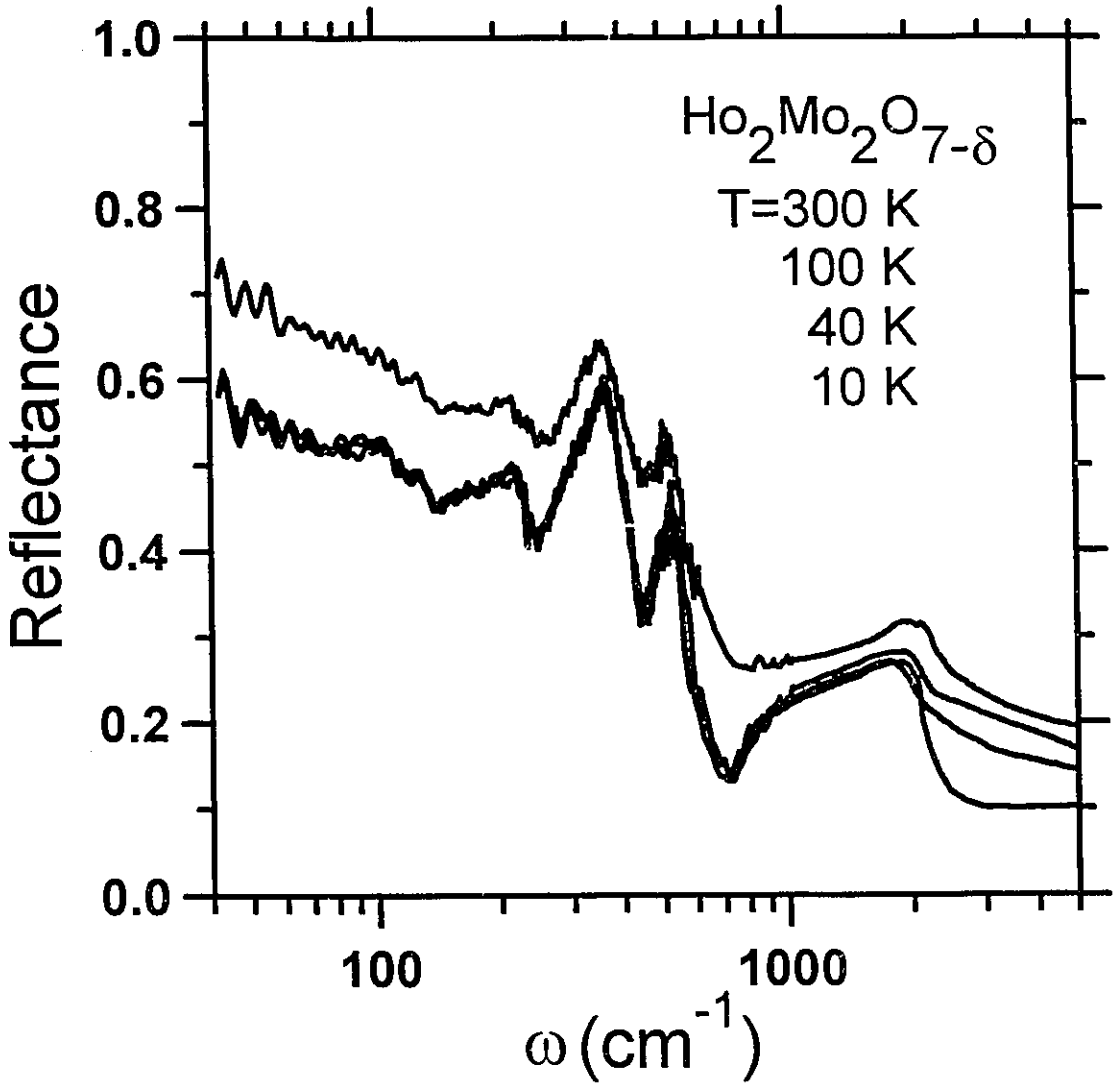

Figure 3.18. Reflectance of $Ho_2Mo_2O_{7-\delta}$ in the frequency range up to 5000 cm^{-1} at 300, 100, 40, and 10 (from top to bottom).

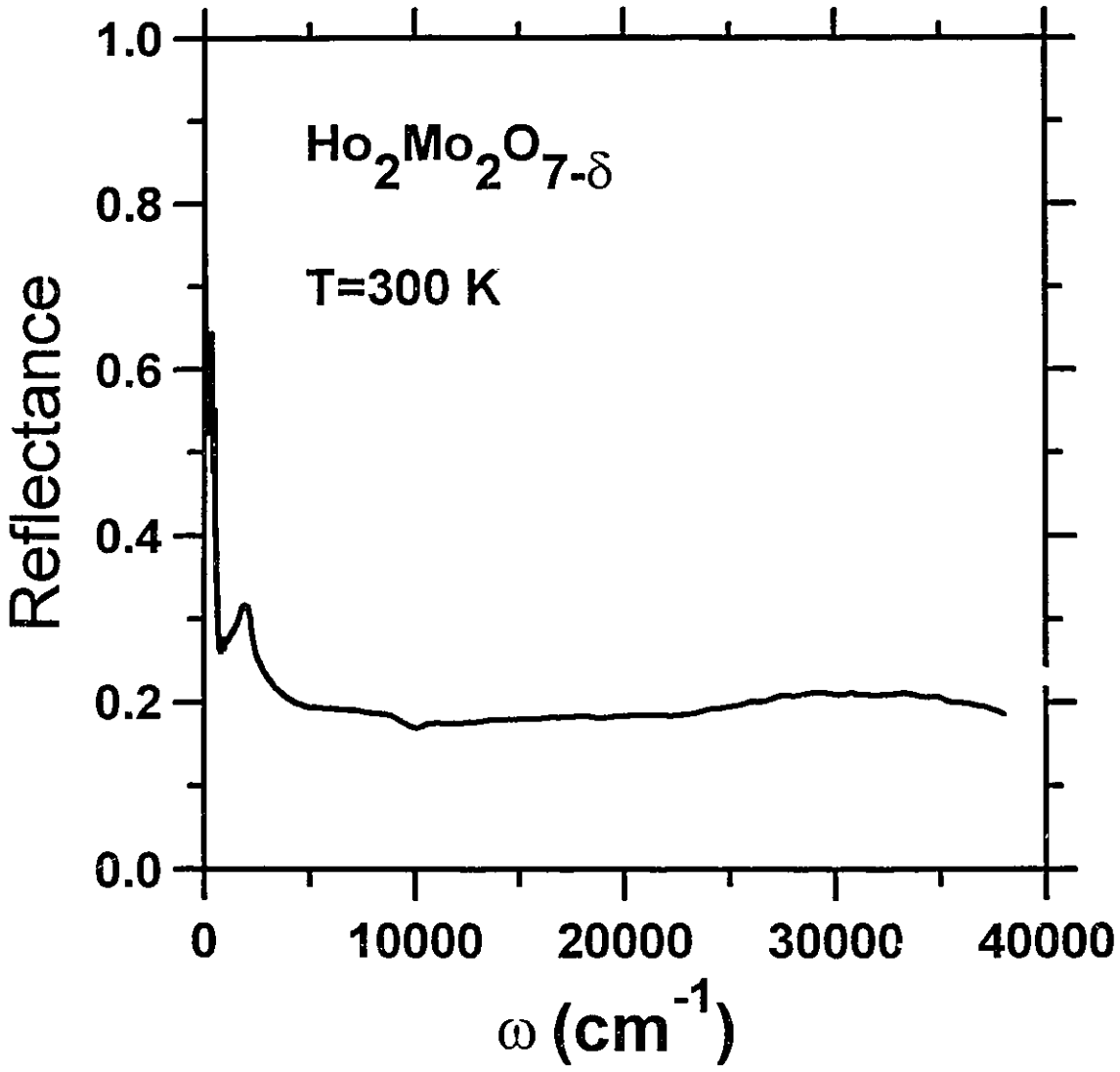

Figure 3.19. Reflectance of $Ho_2Mo_2O_{7-\delta}$ at 300 K up to 40,000 cm^{-1}.

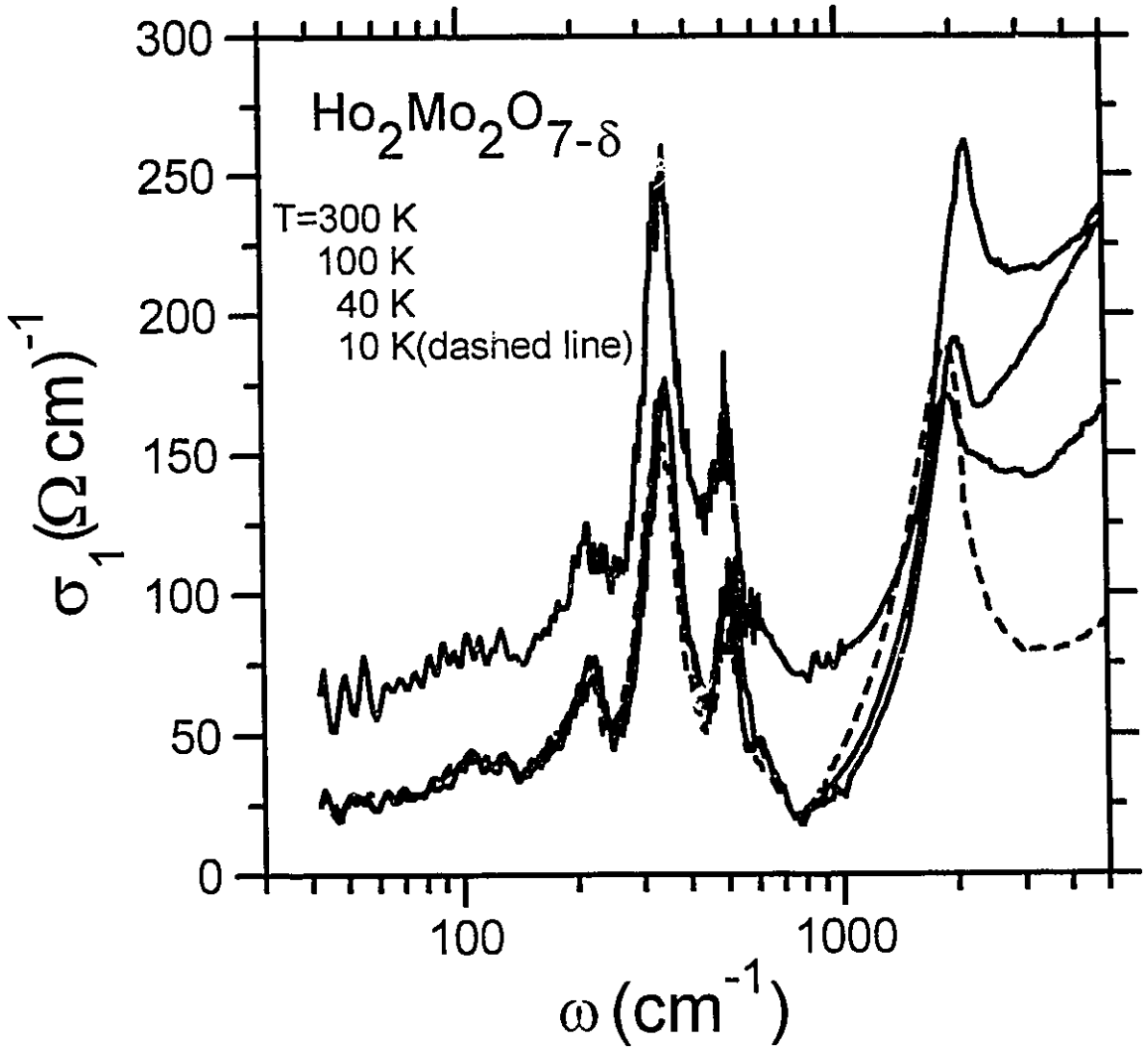

Figure 3.20. Real part of the AC conductivity of $Ho_2Mo_2O_{7-\delta}$ as a function of frequency at 300, 100, 40, and 10 (dashed line) K (from top to bottom).

Table 3.3. The parameters used in Eqn. 3.3 to fit the optical conductivity $\sigma_1(\omega)$ of $Ho_2Mo_2O_{7-\delta}$ from 40 to 700 cm^{-1}. Here a, b, and c are in the units of $\Omega^{-1}cm^{-1}$, Ω^{-1}, and $\Omega^{-1}cm$, respectively, ω_i, γ_i, and d_i are in the units of cm^{-1}, cm^{-1}, and $\Omega^{-1}cm^{-1}$, respectively, and q_i is unitless. Here, i refers to the i^{th} phonon.

Mode	T(K)	
	300	100
a	58.82	18.29
b	0.09131	0.03663
c	-0.0001162	-0.00004654
ω_1	214.7	225.3
γ_1	20.10	22.63
d_1	0.6604	3.764
q_1	-6.879	-2.779
ω_2	340.9	342.8
γ_2	42.70	41.95
d_2	0.08443	0.1251
q_2	44.70	33.46
ω_3	496.4	513.7
γ_3	38.99	41.56
d_3	0.06902	0.09191
q_3	32.06	27.77

symmetric. As the temperature is reduced, all modes harden with little change in their widths. Fig. 3.21 shows the resulting far-infrared background conductivity at 300 and 100 K. It is essentially independent of frequency and the magnitude changes from 70($\Omega^{-1}cm^{-1}$) at 300 K to 20 ($\Omega^{-1}cm^{-1}$) at 100 K. The value of the DC conductivity at 300 K is 163 $\Omega^{-1}cm^{-1}$ which is 90 $\Omega^{-1}cm^{-1}$ larger than the extrapolated value of the far-infrared conductivity to zero frequency at the same temperature. The discrepancy is due to the error in the DC resistivity measurement (see the explanation in subsection 3.2.1). It is reminiscent of the free carrier conductivity of a semiconductor which decreases as the temperature is lowered. There are several problems with this idea. Firstly, the flatness of the conductivity implies a very large scattering rate, of the order of the band gap. Secondly, it is hard to understand the temperature independent conductivity below 100 K. It seems that the conductivity somehow reaches a minimum value at 100 K and cannot decrease further. It should be noted that an asymmetric peak appears around 2000 cm^{-1}. This peak shifts slightly towards lower frequencies with decreasing temperature and does not change below 40 K. There is no interband transition around 2000 cm^{-1} due to the crystal field effect of Ho^{3+}.[29] It appears to be due to excitations of electrons across a small semiconducting gap Δ with a value of 2000 cm^{-1} (~0.25 eV) between the valence band (next to the conduction band) and the conduction band. This will be discussed in detail in the next section. Fig. 3.22 shows the room-temperature conductivity spectrum over a wider range, up to 40,000 cm^{-1}. Generally, the conductivity increases with frequency and there is a broad interband transition peak centered at 32,000 cm^{-1}, which has also been seen in $Sm_2Mo_2O_{7-\delta}$ and $Gd_2Mo_2O_{7-\delta}$ at the two different frequencies. Note that there is a weak structure around 10,000 cm^{-1} which is not real. It is due to a small structure in the merge area of the reflectance spectra from two runs of the experiment covering two different frequency ranges, shown in Fig. 3.19 around 10,000 cm^{-1}.

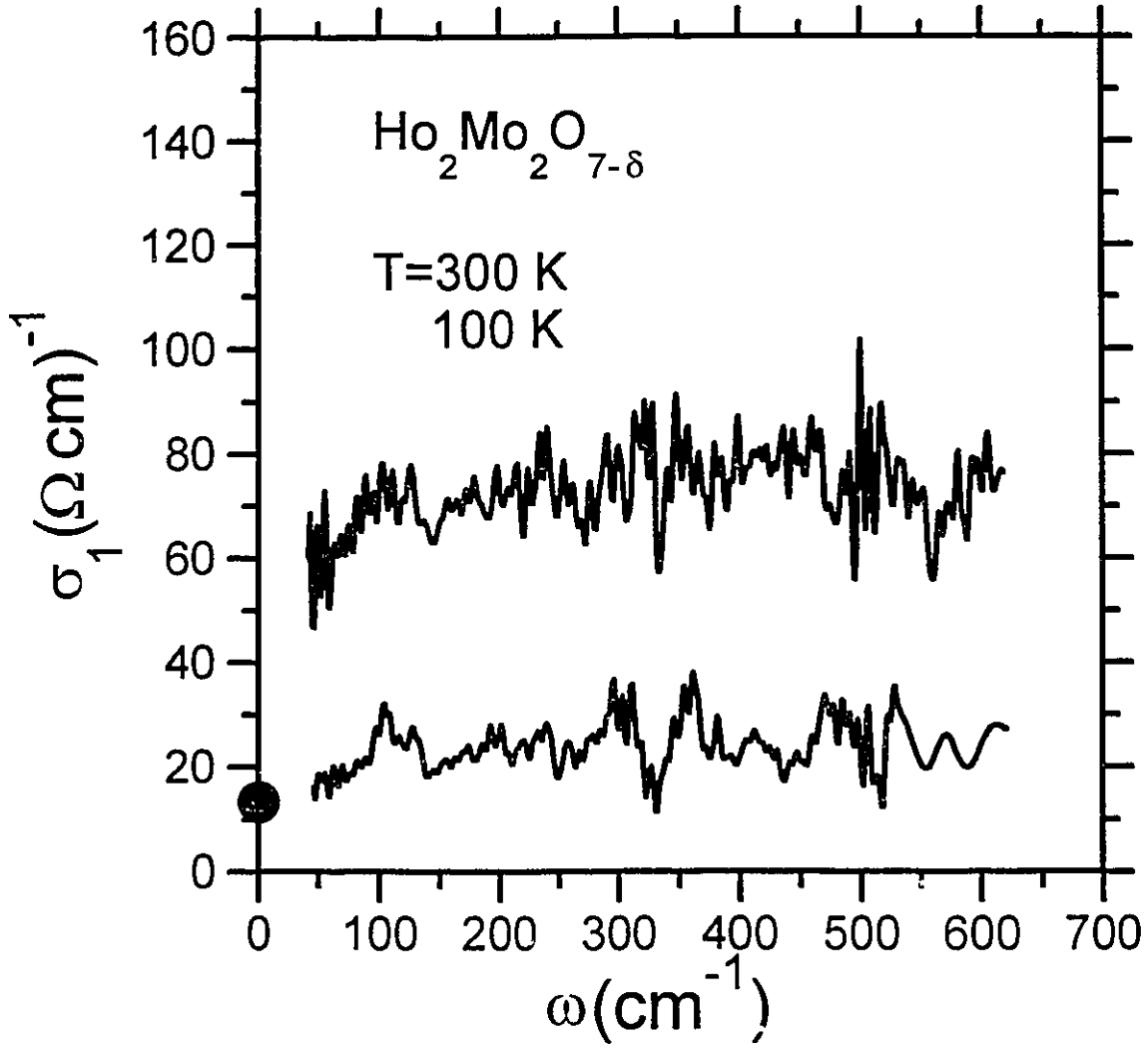

Figure 3.21. Far-infrared background conductivity of $Ho_2Mo_2O_{7-\delta}$ at 300 and 100 K (top and bottom). The value of the DC conductivity of $Ho_2Mo_2O_{7-\delta}$ at 100 K is shown on the left vertical axis as a filled circle.

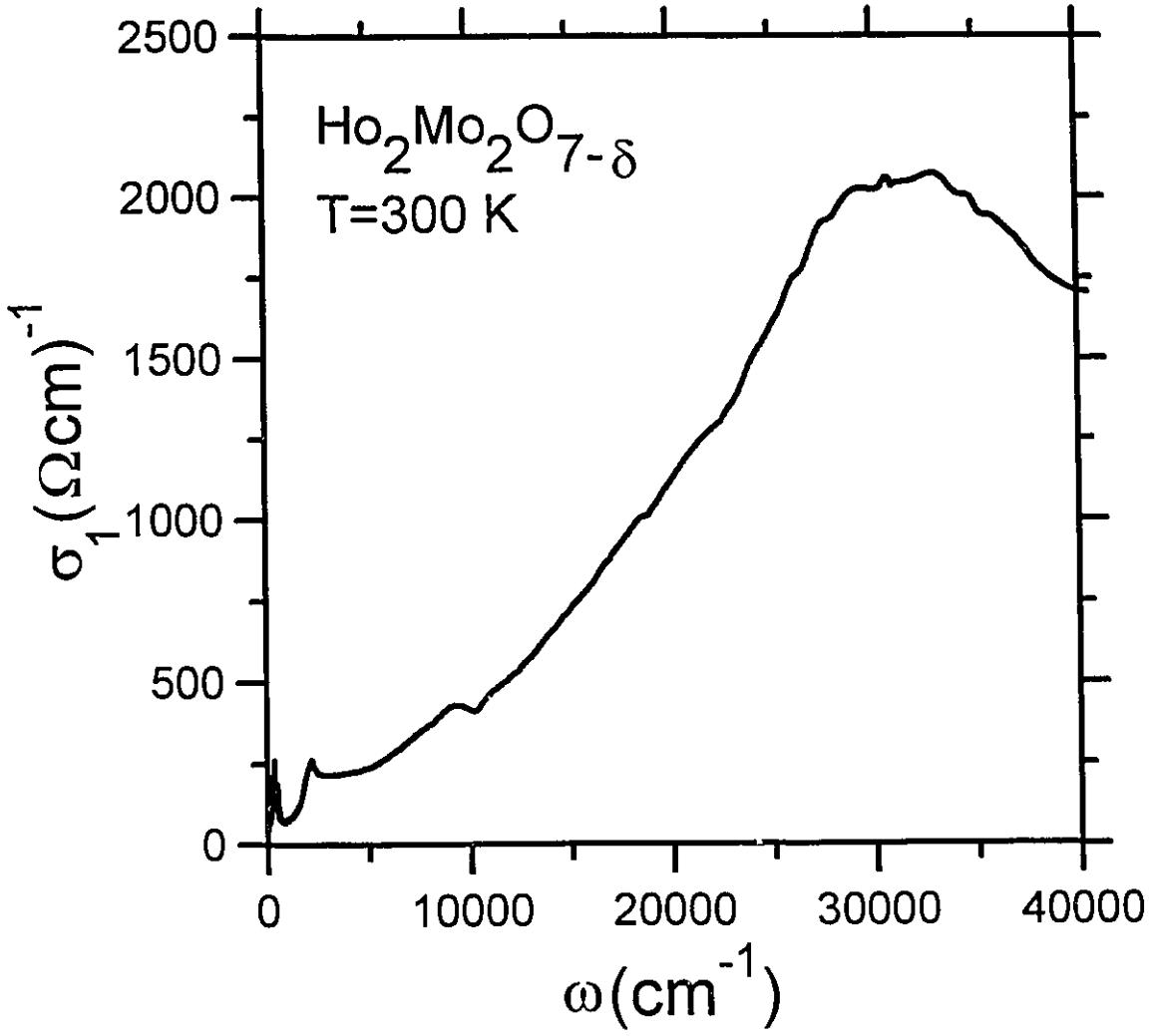

Figure 3.22. Real part of the AC conductivity of $Ho_2Mo_2O_{7-\delta}$ at 300 K as a function of frequency up to 40,000 cm^{-1}.

3.3. Discussions

According to the SB model the band structure of pyrochlore oxides, which is shown schematically in Fig. 3.1, can be considered in terms of two interpenetrating networks of R_2O and $2MoO_3$.[15] The two hybridization bands, the full narrow Mo-O π^*a valence band and the empty broad R-O σ^* conduction band, are separated by a small energy gap Δ in the semiconducting $R_2Mo_2O_{7-\delta}$ materials with a smaller ionic radius of R^{3+} As the radius increases the conduction band moves downward and these two bands ultimately overlap leading to the metallic behavior. The big absorption peak observed in the optical conductivity spectra of $R_2Mo_2O_{7-\delta}$ at high frequencies can be assigned to optical excitations of electrons across the interband gap E_g between the lower filled R-O σ and Mo-O π valence band and the conduction band. Fig. 3.23 shows the interband gap E_g of $R_2Mo_2O_{7-\delta}$ as a function of ionic radius of R^{3+}. It was found that E_g increases linearly with decreasing ionic radius which attests to the applicability of the SB model. $Ho_2Mo_2O_{7-\delta}$ is a semiconductor with $\Delta \approx 2000$ cm^{-1} (~0.25 eV) and $E_g \approx 32{,}000$ cm^{-1}. This is also indicated in the DC resistivity result shown earlier, but the value of the gap $E_a \approx 0.035$ eV deduced from the DC resistivity is much smaller than that (Δ) from the AC conductivity. This is probably caused by an indirect phonon-assisted thermal-excited transition of the conduction electron ($\Delta\vec{k} = \vec{q}$, where $\Delta\vec{k} = \vec{k}' - \vec{k}$ is the difference between the final and initial momentum vectors of the electron, and $\vec{q}$ is the phonon momentum vector) with a smaller gap in the DC conductivity measurement, but, a direct photon-induced transition ($\Delta\vec{k} = 0$) with a larger gap in the AC conductivity measurement. In $Gd_2Mo_2O_{7-\delta}$ E_g is reduced to ≈27,500 cm^{-1} and, therefore, those two bands (Mo-O π^*a and R-O σ^* bands) overlap slightly. This leads to a band structure in which localized states separate from extended states by a mobility edge E_c. The Fermi energy E_F lies at the localized region 300-400 cm^{-1} below E_c, which has been estimated

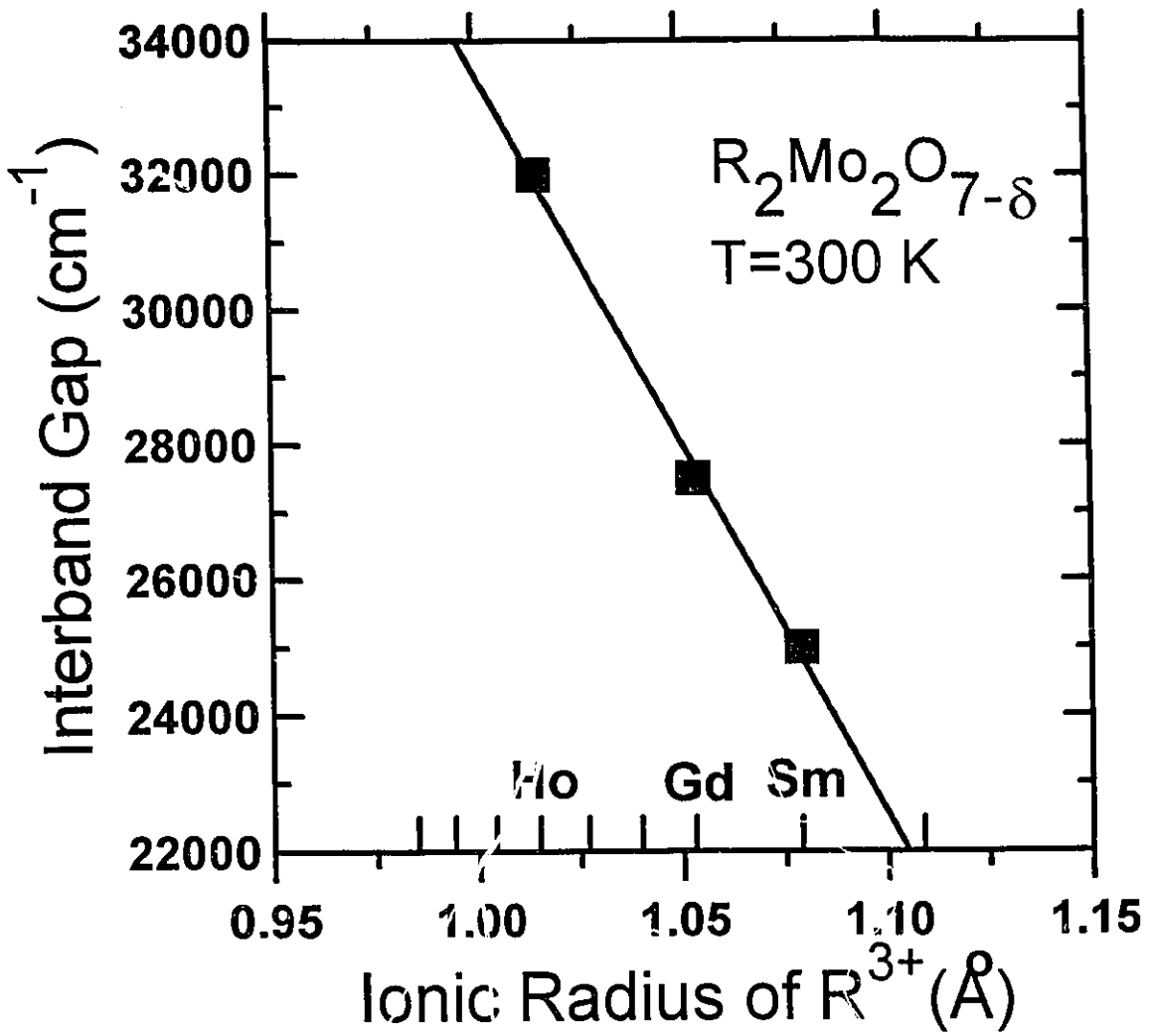

Figure 3.23. Interband gap of $R_2Mo_2O_{7-\delta}$ between the lower R-O σ and Mo-O π valence band and the R-O σ^* conduction band as a function of the ionic radius of R^{3+} for the 8-fold coordination. The solid straight line is the least-squares fit to the data.

from both the optical and DC resistivity measurements in this chapter, resulting in Anderson localization in this crystal. It should be noted that Anderson localization can only happen where there exist some random potential fields to cause the localization of the one-electron wave function.[16] These fields could be built up by some oxygen deficiencies in the $Gd_2Mo_2O_{7-\delta}$ crystal. Recently, the oxygen content was determined by refinement of site occupation parameters on the x-ray data and δ turns out to be ~0.22.[30] This can also be seen indirectly in the DC resistivity measurement on a fully oxygenated polycrystalline $Gd_2Mo_2O_{7-\delta}$ sample which exhibits a metallic behavior.[1] $Sm_2Mo_2O_{7-\delta}$ is a metal because the full Mo-O π^*a band completely merges into the empty R-O σ^* band which can be seen from a further decrease of E_g to 25,000 cm^{-1}. Although there may be some oxygen deficiencies in the single crystals of $Sm_2Mo_2O_{7-\delta}$ and $Ho_2Mo_2O_{7-\delta}$, the electrical behavior of them does not critically depend on the deficiencies, instead, it depends on the size of the rare-earth ion that can been seen in Fig. 3.23.

As pointed by Dr. W.J.L. Buyers,[86] to use the band structure for the system consisting of magnetically localized ions, such as Mo^{4+} and R^{3+} (R: rare-earth elements), one must assume that the magnetic cores of these ions are fixed in the band structure.

3.4. Conclusions

The temperature dependence of the AC conductivity of the spin-glass materials $Sm_2Mo_2O_{7-\delta}$, $Gd_2Mo_2O_{7-\delta}$, and $Ho_2Mo_2O_{7-\delta}$ were obtained by measuring the reflectance of these crystals and by performing Kramers-Kronig analysis on the resulting spectra. The conclusions can be drawn as follows:

(1) The AC conductivity of $Sm_2Mo_2O_{7-\delta}$ shows that it is a poor metal with a large Drude peak width at room temperature. With decreasing temperature it continues to exhibit a metallic behavior. The scattering rate, which is deduced from fitting the far-infrared conductivity using the Drude formula, drops sharply between 150 and 40 K due to the scattering of the conduction electrons by short-range ordered moments of the Mo ions. The scattering rate saturates below 40 K because the moments are frozen out in the spin-glass state.

(2) The empty conduction band and the nearest full valence band overlap slightly in $Gd_2Mo_2O_{7-\delta}$ causing Anderson localization, in which the density of states at E_f is localized. At room temperature electrons are thermally excited to the mobility edge E_c and the AC conductivity is by optical excitations of those electrons in extended states. This results in a behavior characteristic of a poor-metal. In contrast, at low temperatures electrons are localized and the low-frequency AC conductivity is achieved in terms of the optically activated hopping of electrons in localized states which shows a linear depression below 400 cm^{-1}. The localization of electronic states and the phonon-assisted hopping process cause the asymmetric shape of the phonon resonances in the conductivity spectra at low temperatures.

(3) $Ho_2Mo_2O_{7-\delta}$ is a semiconductor with a small gap of $\Delta \approx 2000$ cm^{-1} (~0.25 eV). The gap value decreases a little as the temperature is reduced and does not change below 40 K. The far-infrared conductivity is independent of frequency at all temperatures. Its magnitude shifts downward between room temperature and 100 K and is independent of temperature below 100 K.

An interband-transition peak was found in the ultraviolet region of all these crystals. The position of the peak increases linearly as the ionic radius of R^{3+} is decreased. It supports the following picture of a metal-semiconductor transition in $R_2Mo_2O_{7-\delta}$ within the SB model. The full narrow Mo-O π^*a valence band and the empty broad R-O σ^* conduction band are separated with a semiconducting gap for R=Ho in $Ho_2Mo_2O_{7-\delta}$. With the increase of the ionic radius for R=Gd these two bands overlap slightly due to the R-O σ^* band shifting downward and Anderson localization occurs for $Gd_2Mo_2O_{7-\delta}$. The degree of the overlap increases for R=Sm turning $Sm_2Mo_2O_{7-\delta}$ into a metal.

Chapter 4

The Heavy-Fermion Superconductor UNi_2Al_3

This chapter consists of three sections. The introduction to this newly-discovered material is given in section 1. Section 2 is devoted to present, analyze, and discuss the optical measurement data of UNi_2Al_3. The conclusion will be given in section 3.

4.1. Introduction

Heavy-fermion (HF) materials, especially those that exhibit the coexistence of antiferromagnetic (AF) ordering and superconductivity at low temperatures, *e.g.*, URu_2Si_2[31] and UPt_3[32], have aroused a lot of interest among both experimentalists and theorists. In these materials there is usually a characteristic temperature T_o, above which spin-disorder scattering of the conduction electrons causes the temperature coefficient of the DC resistivity to be negative, below T_o, the scattering is frozen out resulting in a sharp reduction in resistivity.[33] The temperature dependence of the magnetic susceptibility shows a broad peak near T_o that has been explained by crystal-field (CF) splitting,[34] but there is no direct evidence from neutron scattering for these levels. Moreover, susceptibility suggests that the $5f$ moments of the U ions are localized at high temperatures and somehow become delocalized for $T<T_o$. This delocalization has been explained as due to the Kondo effect of the $5f$ spins being compensated by the spins of the conduction

electrons.[35] The trouble with this explanation, as noted by Millis and Lee[36], is that there are not enough conduction electrons within the range of T_K of the Fermi surface, where T_K is the Kondo temperature, to compensate the spins of the ion. Other authors believe that the orbital moment of the ion is so large in these compounds that it results in an almost compensated $5f$ orbital and spin moments.[37] The large electronic specific-heat coefficient γ_e, *e.g.*, $\gamma_e = 422$ mJ/mol K^2 for UPt_3,[38] suggests an enhancement of the effective mass of the quasiparticles resulting from the many body effects of the d conduction electrons and the f electrons of U. Attempts to determine the theoretical ground state which accounts for all these unusual and unique properties of the HF materials have been made.[36,39]

Optical reflectance spectroscopy is a very useful technique in the study of these materials because it can probe the electronic excitation spectra of the heavy quasiparticles that are condensed into superconducting pairs for $T<T_c$. The optical properties of the HF materials have been studied by reflectance and absorption measurements. Bonn *et al.* measured the temperature dependence of the reflectance of URu_2Si_2 in the far-infrared region.[40] They found a spin-density-wave (SDW) gap at the Fermi surface below T_N and a narrow Drude-like mode developing in the coherent region. A similar mode was found in UPt_3.[41,42] This mode is described within a generalized Drude formula by a frequency dependent scattering rate and renormalized effective mass.[7]

Recently, two new HF superconductors, UNi_2Al_3 and UPd_2Al_3, have been discovered.[43,44] Both undergo an AF as well as superconducting phase transition at low temperatures with T_N=4.6 and 14 K and T_c=1 and 2 K, respectively. An optical reflectance measurement has been performed on a polycrystalline UPd_2Al_3 sample, finding a zero-frequency narrow resonance at low temperatures.[45] Single crystals of UNi_2Al_3

have been grown at McMaster and the details of the growth process have been described previously.[46] The crystal quality was characterized using neutron scattering. There are no impurity phases detected. The crystal structure of UNi_2Al_3 is of the hexagonal $PrNi_2Al_3$ material (space group *P6/mmm*), which is shown in Fig. 4.1,[47] with a=5.024 Å and c=4.018 Å. It was found that there exists a longitudinal spin density wave with a very small ordered moment $\mu_{ord} \cong 0.24\ \mu_B$ in the hexagonal basal plane below T_N.[46] The a-c plane DC resistivity of the UNi_2Al_3 single crystal used in this work was measured using a four-probe technique, which is shown in Fig. 4.2. The DC susceptibility was measured by Dr. Gaulin and his co-workers on a second crystal that was used for neutron scattering measurements.[46] Both measurements yield results that are similar to those reported previously.[43] Fig. 4.3 shows the susceptibility of UNi_2Al_3 measured by Geibel *et al.*[43] At high temperatures (T>150 K) the resistivity saturates, which is attributed to spin-disorder scattering, whereas both the absolute value and the slope of the susceptibility at 300 K are characteristic of localized 5*f* electrons of U. A sharp drop in the resistivity below 100 K is accompanied by a broad peak in the $\chi(T)$ *vs.* T curve near ~100 K. This behavior reflects the freezing out of the spin-disorder scattering. Thus, from these two experiments, the characteristic temperature T_o that separates the spin-disorder from the coherent scattering regions is deduced to be approximately 100 K.

Fig. 4.5 shows the specific-heat difference between UNi_2Al_3 and $ThNi_2Al_3$, measured by Steglich *et al.*, with the purpose of isolating the magnetic contribution of the U ion to the specific heat from that of the Ni ions.[48] The experimental data are fit to a model that includes a single-site Kondo effects (S=1/2, T_K=48 K) *via* the Bethe Ansatz and an CF splitting of 125 K (~87 cm^{-1}) between the doublet of the ground state and the singlet of the first excited state of $5f^2$ configuration (J=4) of U. The effective mass of the conduction electron of UNi_2Al_3, m^*, estimated from the resistivity, magnetic, and

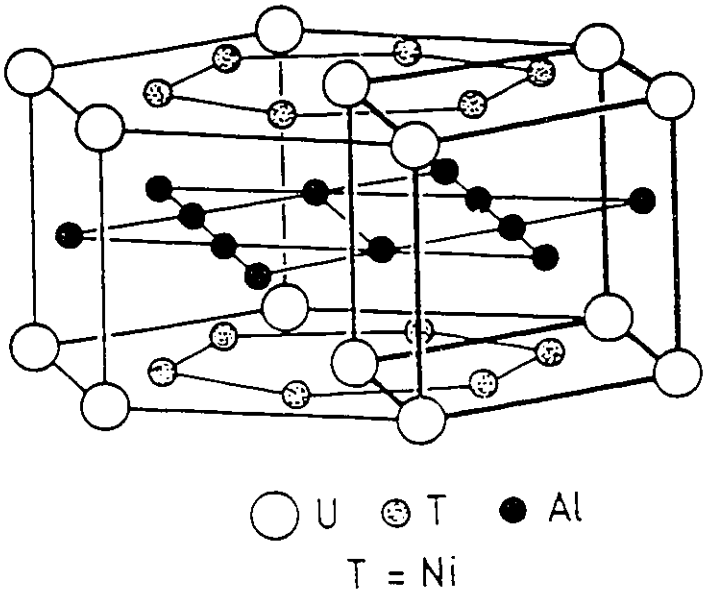

Figure 4.1. Hexagonal UNi_2Al_3 crystal structure. Heavy lines indicate the unit cell. From Ref. 47.

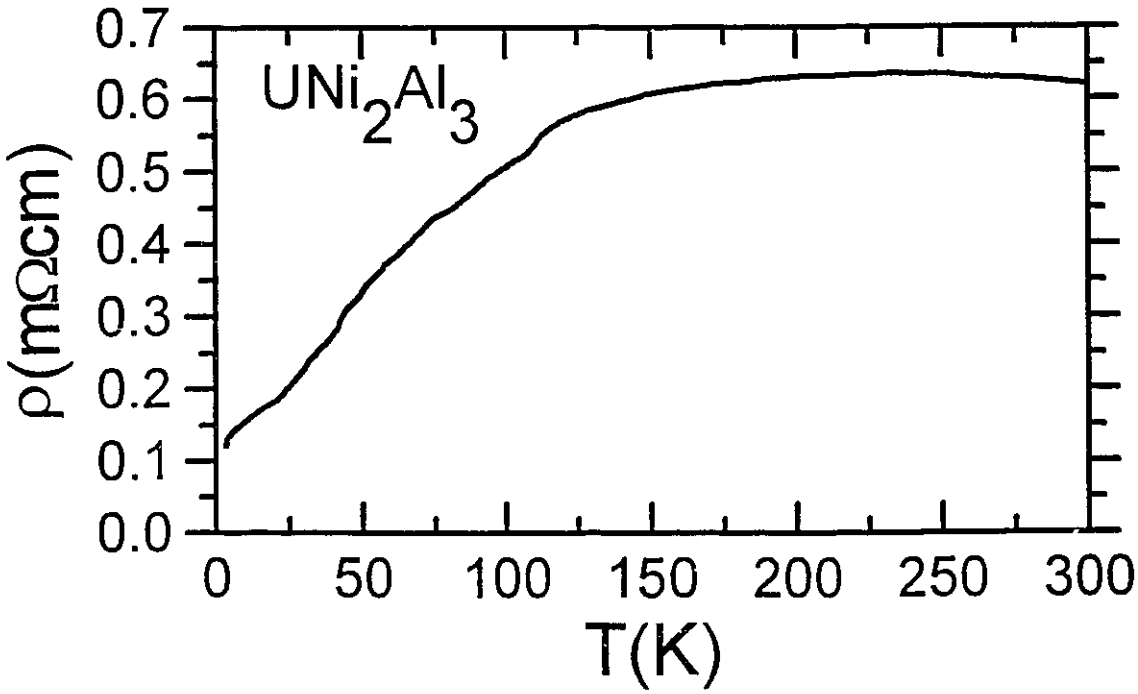

Figure 4.2. DC resistivity of UNi_2Al_3 as a function of temperature.

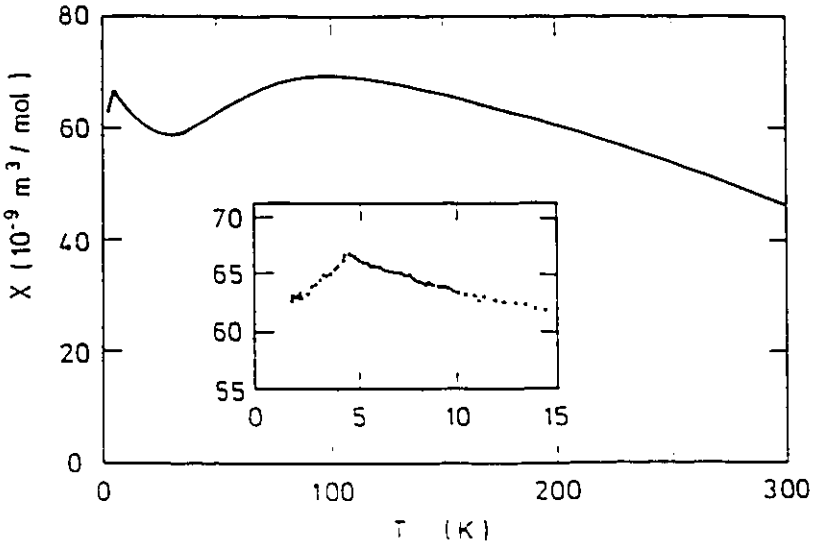

Figure 4.3. DC susceptibility of UNi_2Al_3 as a function of temperature. Inset shows the antiferromagnetic transition at T_N=4.6 K. From Ref. 43.

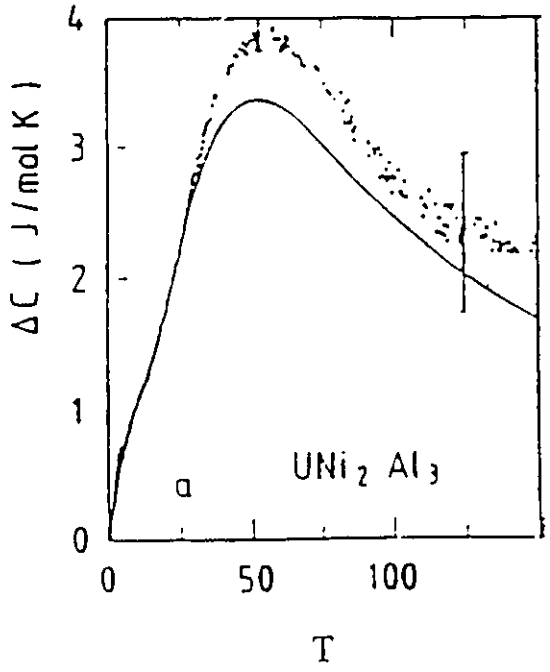

Figure 4.4. ΔC=C(UNi_2Al_3)–C($ThNi_2Al_3$) *vs.* T. Solid curve represents the Bethe-Ansatz result for spin 1/2 single-ion Kondo effect (T_K=48 K) and a doublet-singlet CF splitting of 125 K. From Ref. 48.

specific-heat measurements is 48 m_e, where m_e is the mass of a free electron.

The tunneling experiment has been done on a polycrystalline UNi_2Al_3 sample by Aarts *et al.*[49] The result shows that there is a gap of 10 meV (~81 cm^{-1}) below T_N(≅4.8 K) which is attributed to the excitations of electrons between the ground and the next excited level, which results from the effect of the CF splitting.

4.2. Optical Properties of UNi_2Al_3 along the a-axis

To prepare a UNi_2Al_3 sample suitable for optical measurements, the single crystal was cut parallel to its a-c plane using a spark cutter and was successively polished using #600 diamond grit paper, #4000 waterproof silicon carbide paper, one micron diamond paste, and finally colloidal alumina solution (0.05 μm Al_2O_3 powder suspended in water). The temperature dependence of the polarized reflectance of the UNi_2Al_3 single crystal has been measured from 30 to 8000 cm^{-1} for temperatures between 10 and 300 K using a Michelson interferometer. A second grating spectrometer was used to measure the room-temperature reflectance from 3800 to 40,000 cm^{-1}. The reflectance between 4000 and 44,000 cm^{-1} at low temperatures was measured by Dr. Tanner and his co-worker at University of Florida using a grating spectrometer. We found that the anisotropy of the reflectance between the a and c axis is very small. The results presented here are along the a-axis only.

Fig. 4.5 shows the reflectance of UNi_2Al_3 at 300, 100, and 10 K. Generally speaking, the behavior of the reflectance is metallic, decreasing with increasing frequency. The room-temperature reflectance at high frequencies is similar to that of UPd_2Al_3 and has a bump around 3000 cm^{-1} that also appears at low temperatures.[45] The overall

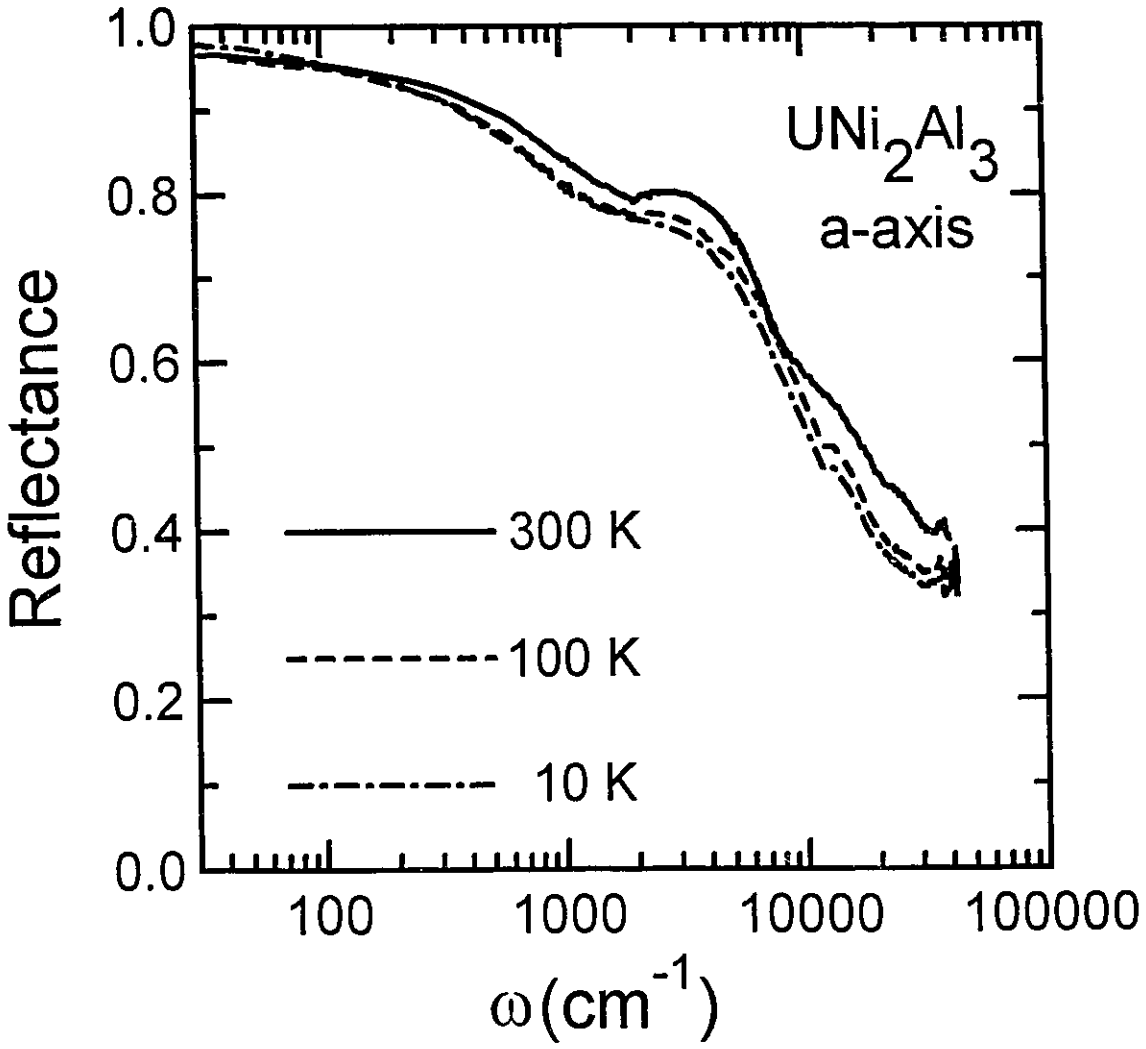

Figure 4.5. Polarized reflectance spectra of UNi_2Al_3 (E||a) at 300, 100, and 10 K in the whole measured frequency region. The 100 and 10 K reflectance was measured between 4000 and 44,000 cm^{-1} by Dr. Tanner and his co-worker at University of Florida using a grating spectrometer.

reflectance at high frequencies decreases with decreasing temperature from 300 to 100 K and has a little temperature dependence between 100 and 10 K. In comparison with the results of the pyrochlore oxides presented in Chapter 3, there is no phonon peak found in the reflectance spectra of UNi_2Al_3 which may be due to screening by the conduction electrons. It is noted that there are two sharp phonon features, one at 108 cm^{-1} and the other at 377 cm^{-1}, found in the reflectance spectra of URu_2Si_2.[31] The temperature dependence of the far-infrared reflectance is shown in Fig. 4.6. Its magnitude decreases with decreasing temperature at higher frequencies, but this behavior changes at lower frequencies below 100 K. The crossover occurs at ~100 cm^{-1} between the 300 and 10 K data and at ~150 cm^{-1} between the 100 and 10 K data. This is typical behavior for the HF materials.[40,50] Note an almost linear frequency-dependent (non-Drude) reflectance at low frequencies for the 300 and 100 K data. This results in an unusual optical conductivity described below.

The real part of the dielectric function $\varepsilon_1(\omega)$ and the real part of the optical conductivity $\sigma_1(\omega)$ are obtained from Kramers-Kronig analysis. To perform this transformation one needs to extrapolate the reflectance at both low and high frequencies. The Hagen-Rubens relation is used as an extrapolation to low frequencies. The results in the experimental data region do not depend on the specific low-frequency extrapolation used. Between 40,000 and 10^6 cm^{-1} a power law of ω^{-2} and beyond this frequency range a free-electron-like behavior ω^{-4} are used. Fig. 4.7 displays the real part of the optical conductivity of UNi_2Al_3 in the whole frequency range at 300, 100, and 10 K. We first focus on the far-infrared conductivity only and will discuss the high-frequency conductivity later. Fig. 4.8 shows the far-infrared conductivity at 300, 100 and 10 K together with the corresponding values for the DC conductivity. It is noted that the extrapolation of the optical conductivity towards zero frequency agrees with the measured

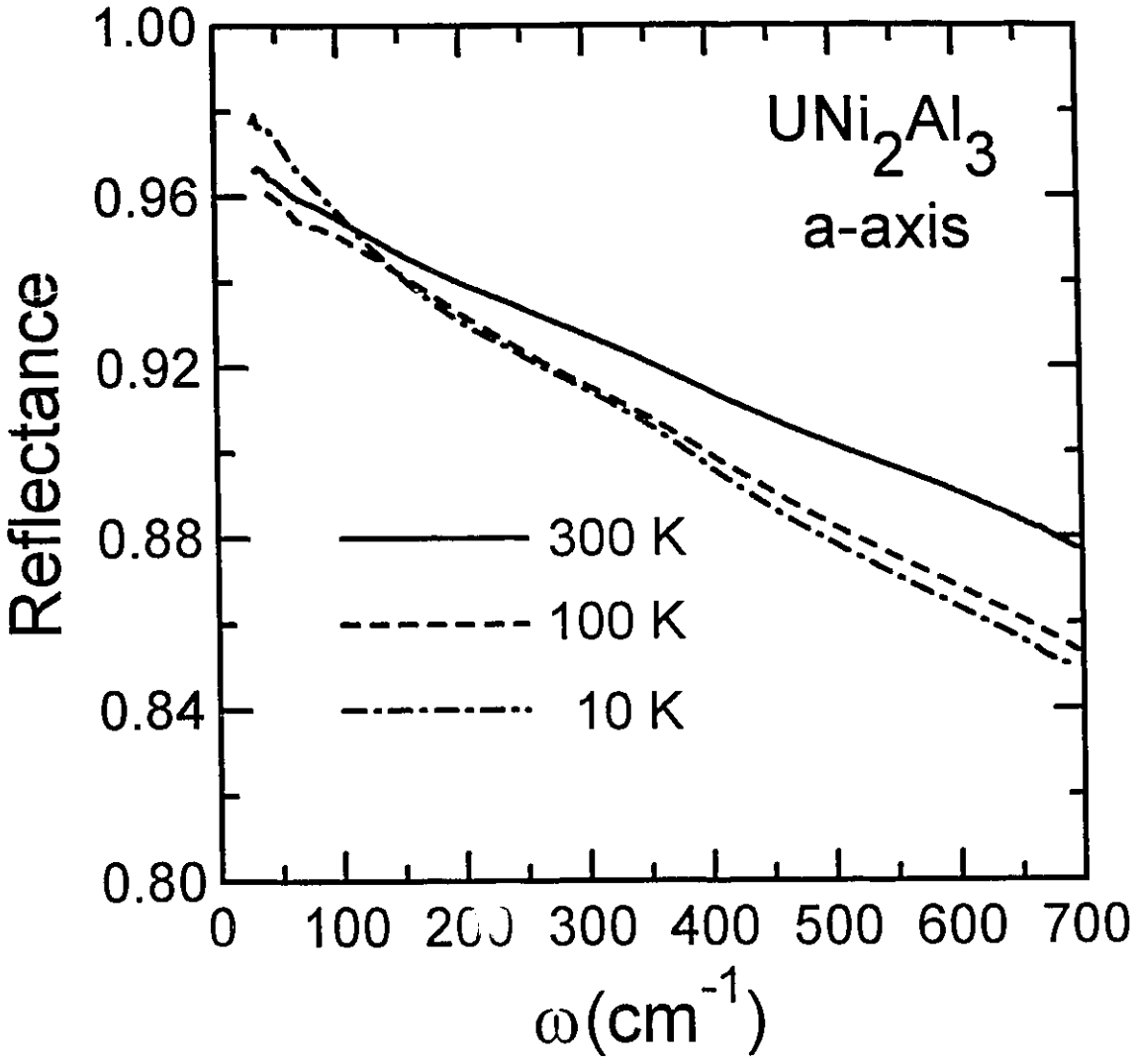

Figure 4.6. Far-infrared reflectance of UNi_2Al_3 at 300, 100, and 10 K. Note that the magnitude of $R(\omega)$ decreases with decreasing temperature at high frequencies, while the opposite behavior is observed at low frequencies below 100 K. The crossover between the 300 and 10 K data occurs at ~100 cm^{-1}, while the crossover between 100 and 10 K data occurs at ~150 cm^{-1}.

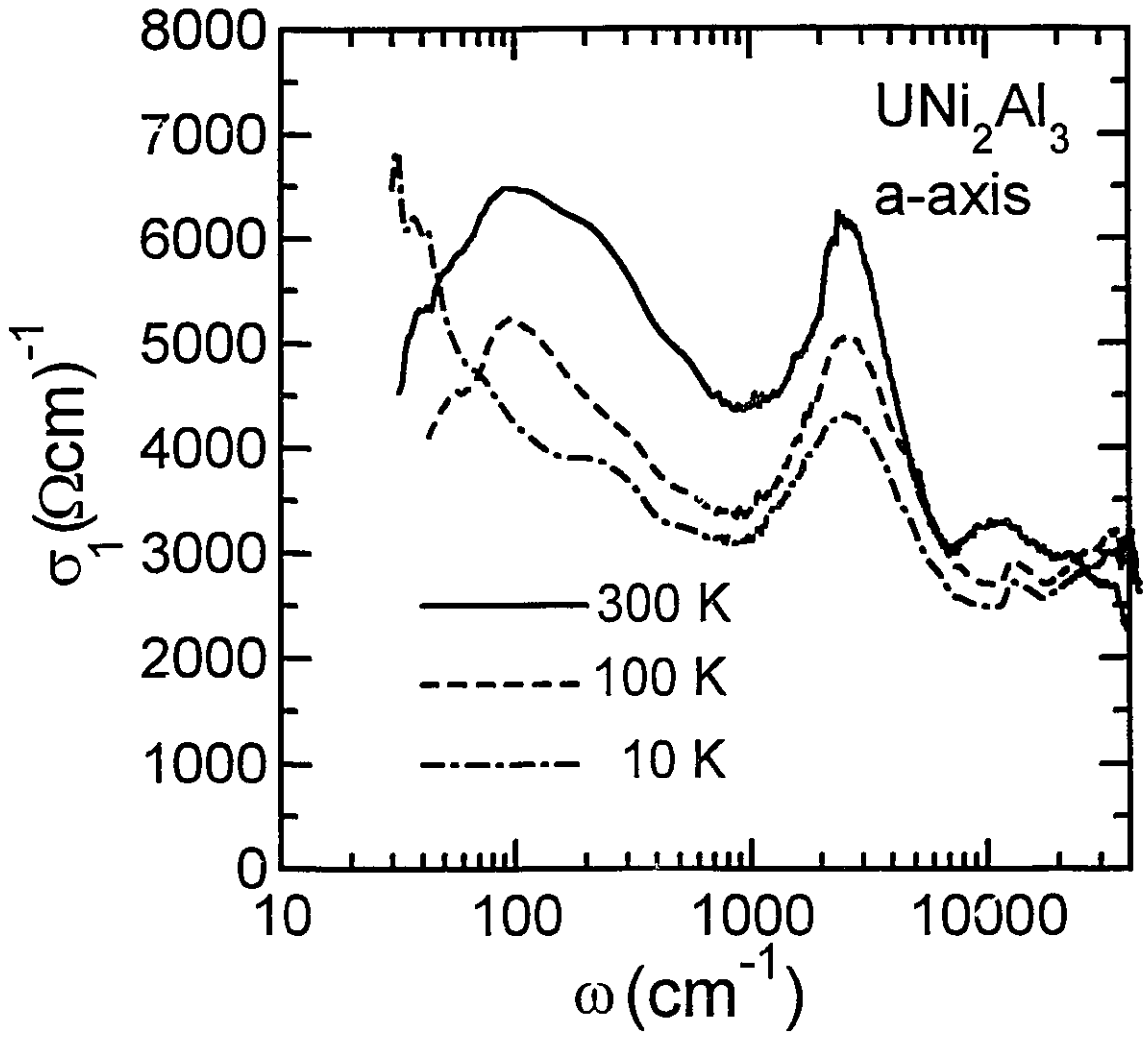

Figure 4.7. Real part of the polarized AC conductivity of UNi_2Al_3 along the a-axis at 300, 100, and 10 K. The conductivity can be fit to a Drude term and four Lorentz osciilators with the fitting parameters being listed in Table 4.1.

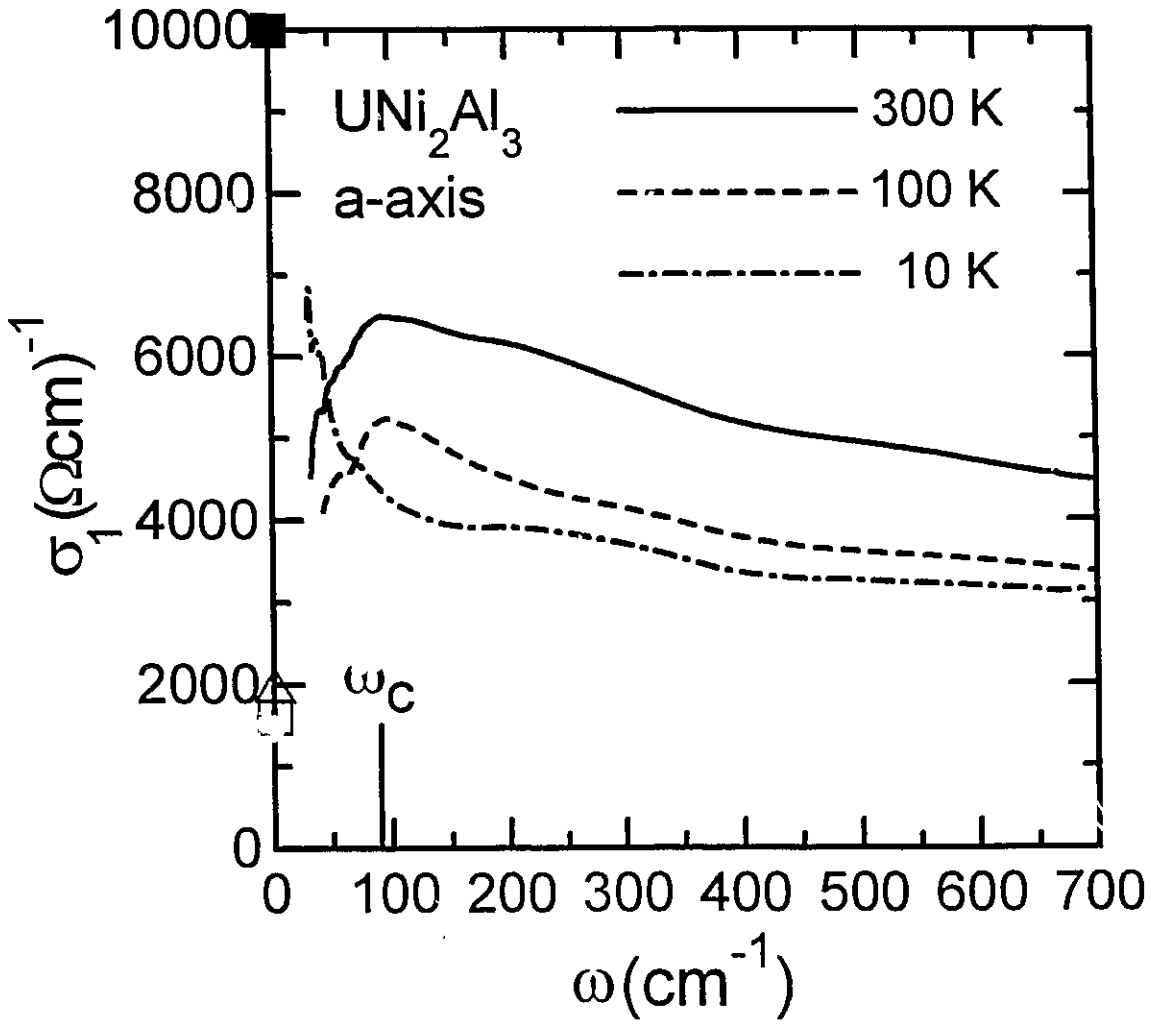

Figure 4.8. Far-infrared conductivity of UNi_2Al_3 at 300 100, and 10 K. The values of the DC conductivity of UNi_2Al_3 at 300 K (square), 100 K (triangle), and 10 K (filled square) as well as a characteristic frequency scale ω_c(=90 cm^{-1}) are indicated. Note that the conductivity declines towards its DC value for frequency below ω_c at 300 and 100 K, whereas a narrow Drude-like peak develops for $\omega < \omega_c$ in the 10 K data.

DC conductivity. Interestingly, there exists a characteristic frequency $\omega_c \cong 90$ cm^{-1} which divides the conductivity spectrum into two different regions. For $\omega > \omega_c$ the conductivity increases with decreasing frequency, as is typical for metals, and its magnitude is reduced as the temperature is lowered. Below ω_c the conductivity begins to decline to the DC conductivity value for the 300 and 100 K data, but rises very rapidly to its DC value at 10 K. Note that the energy scales for the characteristic frequency and the characteristic temperature T_o [the coherence develops for $T<T_o(\cong 100$ K)], deduced from the DC resistivity and susceptibility, are comparable with each other.

To see the far-infrared optical behavior more clearly the real part of the frequency-dependent dielectric function $\varepsilon_1(\omega)$ of UNi_2Al_3 is shown in Fig. 4.9. At high frequencies $\varepsilon_1(\omega)$ is negative at all temperatures. Below ~100 cm^{-1} the dielectric function rises dramatically to positive values for the 300 and 100 K curves, but drops sharply at the same frequency at 10 K. We attribute the positive low-frequency $\varepsilon_1(\omega)$ at high temperatures to an interband transition. As mentioned before, Steglich *et al.*[48] fit the specific heat to a model that includes a single-site Kondo effect (S=1/2, T_K=48 K) and a crystal-field (CF) splitting of 125 K (~90 cm^{-1}) between the doublet of the ground state and the singlet of the first excited state. Also, a gap of ~81 cm^{-1}, which is attributed to the CF splitting, is shown up in the tunneling spectrum at very low temperatures.[49] The value of this CF gap coincides with the peak of the conductivity at 300 and 100 K, as shown in Fig. 4.8. The large negative values of $\varepsilon_1(\omega)$ in the low frequency region at 10 K is in accord with the narrow Drude-like mode shown in the 10 K conductivity spectrum.

The narrow, Drude-like conductivity mode could be fit to a theoretical model proposed by Millis and Lee,[36] which uses the low-temperature Anderson-lattice Hamiltonian to explain the frequency- and temperature-dependent conductivity. In this

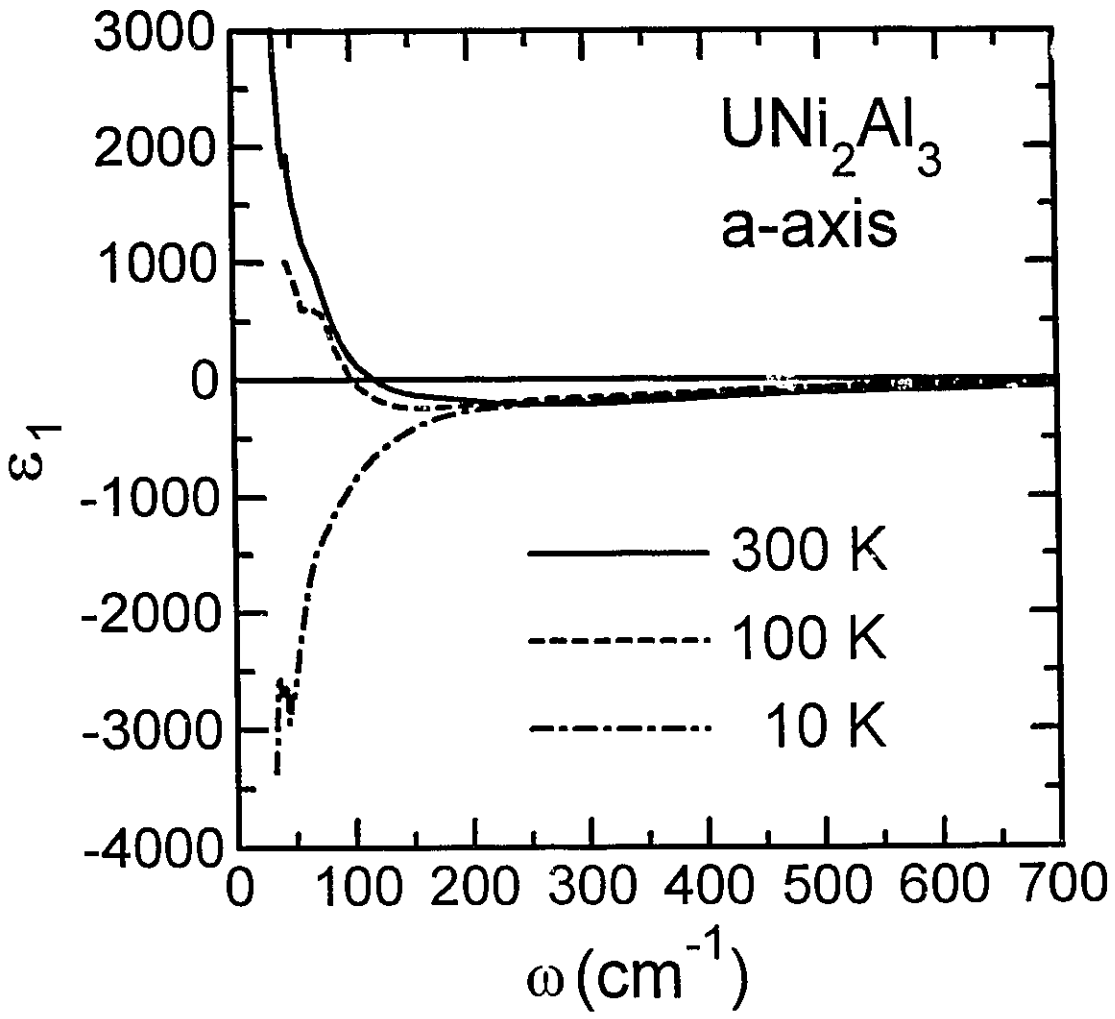

Figure 4.9. Real part of the a-axis far-infrared dielectric function of UNi_2Al_3 at 300, 100, and 10 K. At low frequencies $\varepsilon_1(\omega)$ decreases sharply at 10 K corresponding to the narrow Drude-like peak as shown in the 10 K optical conductivity spectrum (Fig. 4.8). $\varepsilon_1(\omega)$ increases to a positive value at 300 and 100 K as a result of a peak in $\sigma_1(\omega)$ at ω_c, presumably due to the CF splitting of the $5f^2$ (J=4) level of tetravalent uranium.

model the total conductivity consists of two components, one describing the impurity scattering and the other describing boson fluctuations, where the conduction electrons are scattered by the boson fields, analogous to electron-phonon scattering. The conductivity for the impurity scattering part is given by,

$$\sigma_i(\omega) = \frac{(\omega_P^*)^2 \gamma^*}{4\pi\left[\omega^2 + (\gamma^*)^2\right]}, \tag{4.1}$$

where the renormalized scattering rate $\gamma^* = (m_b / m^*)\Gamma$ (m_b, m^*, and Γ are the band mass, the renormalized mass, and the static scattering rate of the conduction electrons, respectively) and the renormalized plasma frequency $(\omega_P^*)^2 = 4\pi n_e e^2 / m^*$ (n_e is the total free carrier density). In this model there is a characteristic frequency ω_c (ω_c=90 cm^{-1} for UNi_2Al_3) above which $\sigma_i(\omega)$ dies away causing the conductivity to become independent of frequency at a value of σ_m. This saturation conductivity σ_m is equal to $n_e e^2 / (m_b W)$, where W is the quasiparticle bandwidth. Fig. 4.10 shows the fit to the 10 K far-infrared conductivity using the formula: $\sigma(\omega) = \sigma_i(\omega) + \sigma_m$. The parameters obtained from this fit are ω_P^*=3400 cm^{-1} (~0.42 eV), γ^*=25 cm^{-1} (~3.1 meV), and σ_m=3800 $\Omega^{-1}cm^{-1}$. The DC conductivity, deduced from the parameters of ω_P^*, γ^*, and σ_m, is 11,300 $\Omega^{-1}cm^{-1}$ roughly consistent with the measured value of 10,000 $\Omega^{-1}cm^{-1}$. As a check on these parameters, one can estimate the value of ω_P^* from the superconducting properties using the London penetration-depth formula in the impure limit ($\xi << \lambda_L$),[51]

$$\lambda_P = \lambda_L \sqrt{\frac{\xi}{l}} = \frac{c}{\omega_P^*} \sqrt{\frac{\xi}{l}}, \tag{4.2}$$

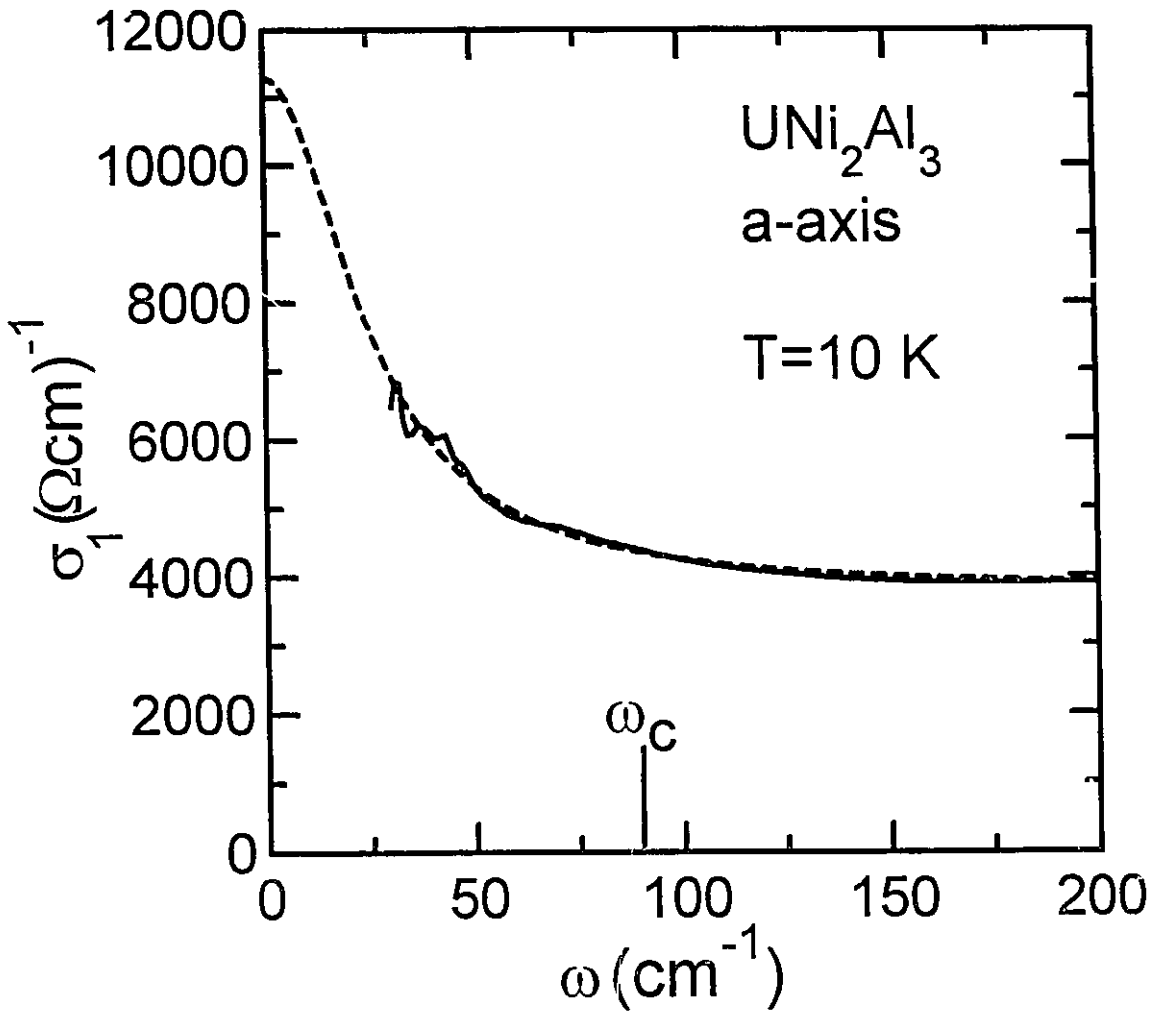

Figure 4.10. Solid line represents the experimental optical conductivity data of UNi_2Al_3 at 10 K. The dashed line results from a fit using the frequency-dependent term $\sigma_1(\omega)$, as shown in Eqn. 4.1, together with a frequency-independent term σ_m.

where ξ and l are the coherence length and the mean free path, respectively. Using the values of l=470 Å, ξ=240 Å, and λ_P=3300 Å for UNi_2Al_3[48] one obtains ω_P^*=3400 cm^{-1}, in fair agreement with the value that we have obtained in this work.

The development of the narrow Drude-like mode seen in the 10 K data is quite common among the HF materials in the coherent region (the region where the spin-disorder scattering is frozen out).[41,40,50] It is known that the anomalous properties of the HF materials are determined by the behavior of the quasiparticles that result from the hybridization between the *d* conduction electrons and the localized *f* electrons of U as the temperature is reduced into the coherent region.[2] The Drude-like mode is governed by the behavior of the quasiparticles, *i.e.*, a large mass and a dramatically reduced scattering at the Fermi level. In studying the optical properties of CrSb, MnSb, NiSb, and NiAs, Allen and Mikkelsen first used a generalized Drude formula to get the frequency dependent scattering rate $\Gamma(\omega)$ and renomalization factor $\lambda(\omega)$ of these materials. The mass enhancement $m^*/m_b = 1+\lambda(\omega)$ (see Chapter 2).[7] The same scheme was used in analyzing the conductivity data of the UPt_3, URu_2Si_2, and UNi_2Si_2 materials as well as the mixed-valence compound $CePd_3$.[41,40,50,52] Here, we use the same formalism to get $\Gamma(\omega)$ and $\lambda(\omega)$ for UNi_2Al_3. To calculate the absolute values of both quantities one must first determine the value of the bare plasma frequency, ω_P. We estimate $\omega_P \cong$23,400 cm^{-1} (~ 2.9 eV) using the static value of $m^*/m_b = 48$[48] and the relation $\omega_P/\omega_P^*(10\text{ K})=(m^*/m_b)^{1/2}$ assuming that the band mass $m_b \approx m_e$ and the free carrier density n_e does not change with temperature. Using the relation $\omega_P^2=4\pi n_e e^2/m_e$, a free carrier density of $n_e=6.1\times10^{21}$ cm^{-3} is obtained for UNi_2Al_3. This value is less than $n_e=1.09\times10^{22}$ cm^{-3} obtained for UPd_2Al_3.[45]

Figs. 4.11 and 4.12 show respectively the frequency-dependent scattering rate

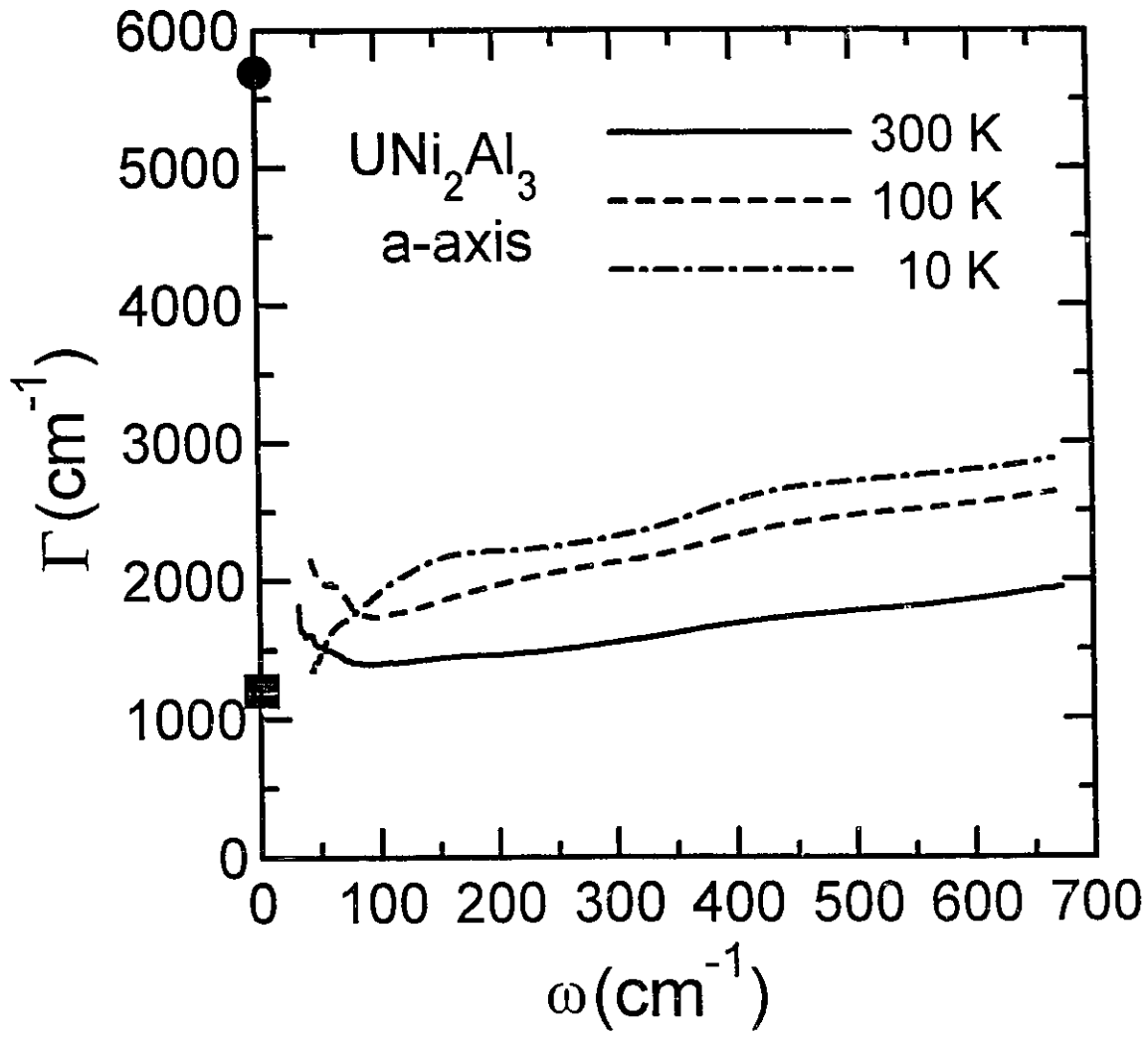

Figure 4.11. Frequency-dependent scattering rate of UNi_2Al_3 at 300, 100, 10 K. The values of $\Gamma(0)$ at 300 and 10 K are represented by the filled circle and square on the left vertical axis, respectively.

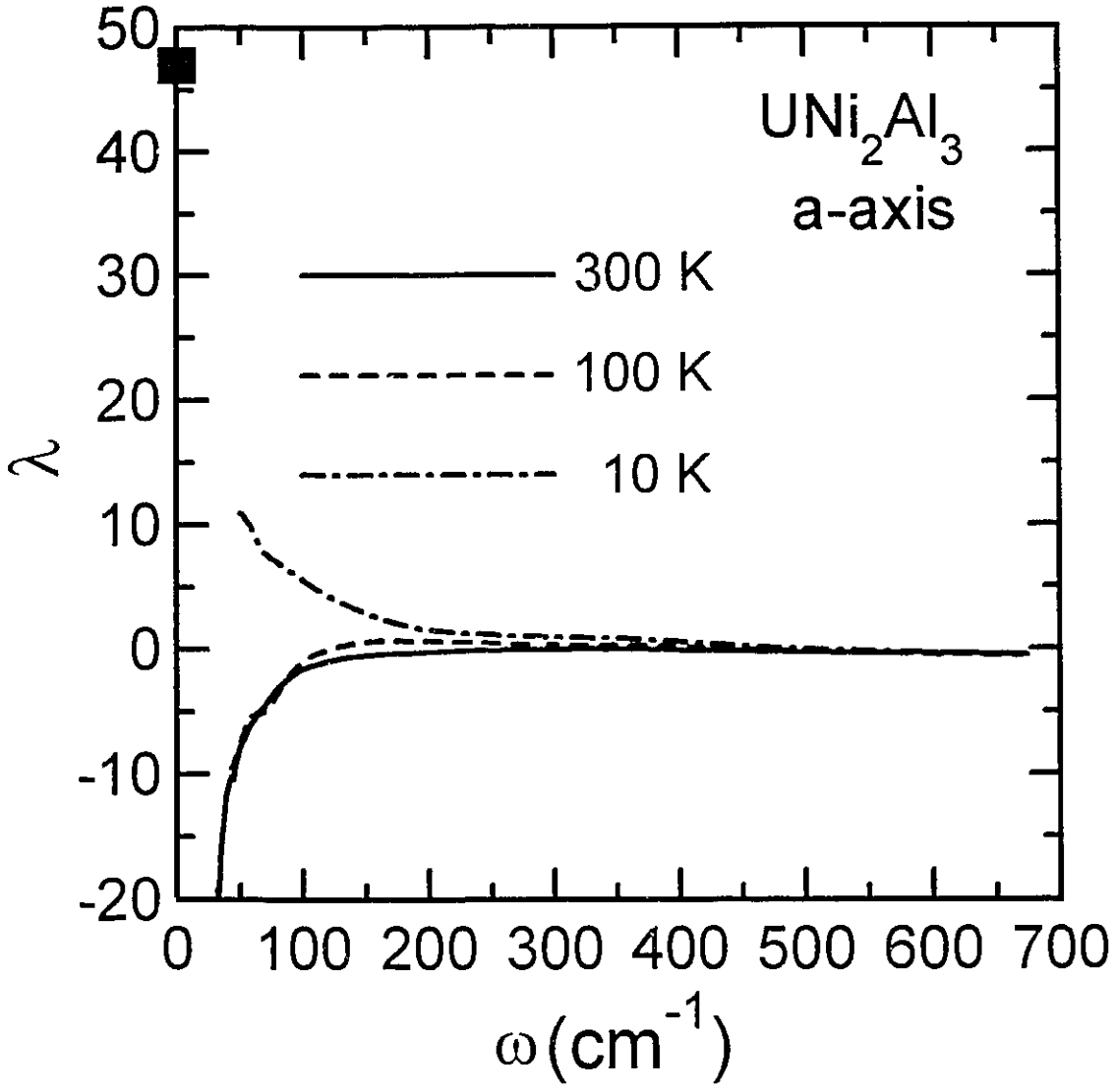

Figure 4.12. Frequency-dependent renormalization factor of UNi_2Al_3 at 300, 100, and 10 K. The value of $\lambda(0)$ at 10 K is given by the filled square on the left vertical axis.

$\Gamma(\omega)$ and renormalization factor $\lambda(\omega)$ of UNi_2Al_3 at 300, 100, and 10 K. We use the fitting parameter $\gamma^*(10\text{ K})$ obtained previously and the static value $m^*/m_b(=48)$ obtained from the specific heat measurement by Steglich *et al.*[48] to get $\Gamma(\omega=0)=1200\text{ cm}^{-1}$ $\{=[1+\lambda(0)]\gamma^*(10\text{ K})\}$ at 10 K. The values of $\Gamma(0)$ and $\lambda(0)$ are indicated in the figures as filled squares. The value of $\Gamma(0)$ at 300 K (~5700 cm^{-1}) is also shown in Fig. 4.11 as the filled circle using the values of the plasma frequency ($\omega_p=23{,}400\text{ cm}^{-1}$) and the DC conductivity (1600 $\Omega^{-1}\text{cm}^{-1}$). The scattering rate gently decreases with decreasing frequency and the magnitude increases as the temperature is reduced at high frequencies. Interestingly, $\Gamma(\omega)$ turns up near 100 cm^{-1} towards the high DC value due to the interband transition in the 300 and 100 K data. In contrast, at 10 K $\Gamma(\omega)$ drops sharply below 150 cm^{-1} towards its DC value. Such a drop has been seen in other HF materials.[41,40,50] The renormalization factor $\lambda(\omega)$ drops off below 100 cm^{-1} and becomes negative at lower frequencies. This unphysical result is due to the interband transition at 300 and 100 K. In contrast, $\lambda(\omega)$ turns up to its high DC value at 10 K.

The static scattering rate of UNi_2Al_3 for $T>T_o$ is quite large due to the spin-disorder scattering of the conduction electrons. $\Gamma(\omega)$ dramatically declines with increasing frequency until $\omega\sim\omega_c$, after which it slightly increases with frequency. For $T<T_o$ $\Gamma(\omega)$ increases with frequency to its saturated value near ω_c. The narrowing of the Drude-like mode found in the 10 K data is due to a small value of $\Gamma(\omega)$ and a further reduction by a factor $[1+\lambda(\omega)]^{-1}$.

The quasiparticle bandwidth W is ~2400 cm^{-1} (~0.30 eV) deduced from the relation $\sigma_m=n_e e^2/(m_b W)$. Using the relation $m_e/m^*\sim T_K/W$,[36] where T_K is the Kondo temperature, we get $T_K\sim72$ K in comparison with $T_K=48$ K from the fit to the specific heat result.[48] As Lee *et al.* pointed out,[2] the quasiparticle band results from the *f*-bands

being moved up to the Fermi level and, then, being narrowed by the hybridization with the *d*-conduction band.

We now discuss the high-frequency conductivity. As shown in Fig. 4.7, the overall conductivity at high frequencies decreases with decreasing temperature. We fit the conductivity spectra at 300, 100, and 10 K to a Drude term and four Lorentz oscillators. The parameters of the Drude term at 300 and 10 K have been given above and for the 100 K case, we assume that the plasma frequency is the same as the one at 300 K and determine the scattering rate using the values of the DC conductivity (~2000 $\Omega^{-1}cm^{-1}$) and the plasma frequency. The fitting results are listed in Table 4.1. The lowest-frequency Lorentz mode corresponds to the interband transition between the ground and the first excited level that is due to the CF splitting mentioned before. Interestingly, we find that this mode still exists at 10 K with the position shifting to a slightly lower frequency though the narrow Drude-like coherent mode is a dominant one in far-infrared at this temperature. Three absorption peaks appear in the higher-frequency region at all temperatures, one is around 2700 cm^{-1} and the other two are located above 10,000 cm^{-1}, that are attributed to the interband transitions. Similar high-frequency absorption peaks have been also found in UPd_2Al_3.[45] With decreasing temperature, the position of mode 2 increases from 300 to 100 K and moves back at 10 K, whereas the width of the mode increases continuously; the position of mode 3 shifts to a higher frequency from 300 to 100 K and stays there below 100 K, while the width becomes wider from 300 to 100 K and narrower from 100 to 10 K; for mode 4, the change of the position is similar to that of mode 3, whereas the change of the width is similar to that of mode 2.

4.3. Conclusion

The temperature dependence of the optical constants of UNi_2Al_3 has been investigated using reflectance spectroscopy. A characteristic frequency scale ω_c(≅ 90 cm^{-1}), which is comparable to the characteristic temperature T_o(≅100 K) deduced from the DC resistivity and susceptibility, is found in the optical conductivity spectra. At high temperatures ($T>T_o$) this scale represents the peak position of the interband transition due to the CF splitting of the $5f^2$ (J=4) level of tetravalent uranium. A narrow Drude-like quasiparticle absorption mode develops below ω_c at low temperatures that is due to the hybridization between the $3d$ conduction band of nickel and the $5f$ bands of uranium. Using the Millis-Lee model,[36] we are able to obtain the renormalized scattering rate $\gamma^* = 25$ cm^{-1} and the renormalized plasma frequency $\omega_p^* = 3400$ cm^{-1} for this narrow mode at 10 K. The quasiparticle bandwidth is also estimated to be ~0.30 eV.

Table 4.1. The parameters used to fit the polarized optical conductivity $\sigma_1(\omega)$ of UNi_2Al_3 along the a axis at 300, 100, and 10 K. γ^D and ${\omega_P}^D$ are the scattering rate and plasma frequency of the Drude part and ω_i, γ_i, and ${\omega_P}^i$ are the center position, width, and strength of the i^{th} Lorentz oscillator. All units are in cm^{-1}.

Mode	T(K)		
	300	100	10
γ^D	5700	4550	25.30
${\omega_P}^D$	23,370	23,370	3373
ω_1	121.1	106.6	94.43
γ_1	784.5	444.3	797.4
${\omega_P}^1$	14,562	8735	13,422
ω_2	2676	2842	2672
γ_2	3272	4649	5270
${\omega_P}^2$	28,714	29,983	34,745
ω_3	12,416	13,613	13,468
γ_3	18,551	22,547	19,494
${\omega_P}^3$	49,354	47,415	40,565
ω_4	32,759	38,570	38,637
γ_4	42,530	50,585	57,106
${\omega_P}^4$	69,818	87,428	92,839

Chapter 5

The Quasi-One-Dimensional Organic Superconductor $(TMTSF)_2ClO_4$

A review of previous experimental results of $(TMTSF)_2ClO_4$ will be given in section 1. Section 2 will present and analyze the polarized reflectance data of $(TMTSF)_2ClO_4$ from far-infrared to near-infrared region along the chain axis. The conclusion will be drawn in section 3.

5.1 Review of Properties of $(TMTSF)_2ClO_4$ from Previous Experiments

The quasi-one-dimensional organic superconductor $(TMTSF)_2ClO_4$ has been extensively studied since it is the only member of the $(TMTSF)_2X$ family (where X is an inorganic anion) that exhibits a three-dimensional superconducting transition with $T_c \cong 1.2$ K at ambient pressure.[4] The crystal structure of $(TMTSF)_2ClO_4$,[53] shown in Fig. 5.1, is triclinic (space group $P\bar{1}$) and forms the zig-zag stack of the nearly planar TMTSF molecules parallel to the a(chain)-axis. The stacks are arranged in sheets with a short distance ($\cong$3.78 Å at room temperature) between two Se ions in neighboring stacks. Within a stack the intrastack distances, d_1 and d_2, alternate, giving rise to a slight dimerization of the structure along the a axis at low temperatures. The tetrahedral non-centrosymmetric anion ClO_4^- randomly resides at either two equivalent positions of an inversion center leading to a disorder at high temperatures. An anion disorder-order phase

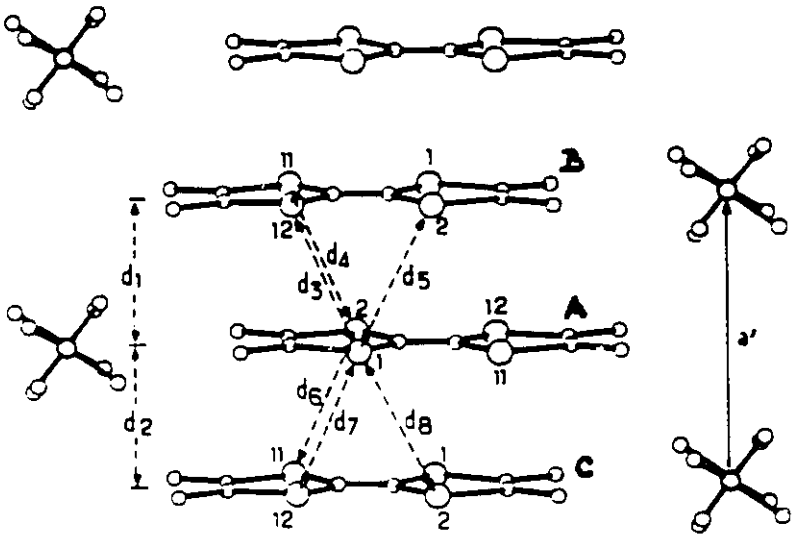

(a)

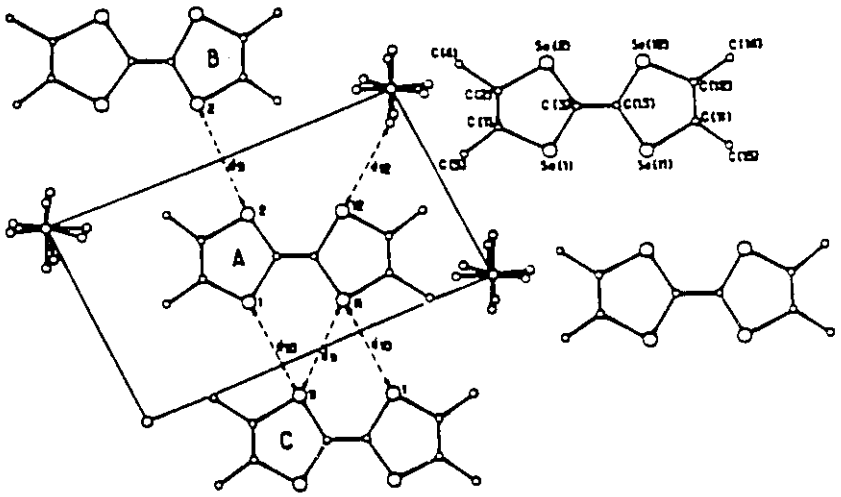

(b)

Figure 5.1. Crystal structure of $(TMTSF)_2ClO_4$: (a) along the a (chain) axis; (b) in the b-c plane. From Ref. 53.

transition occurs at 24 K with the wave vector pointing in the direction of the b axis, as shown in Fig. 5.2, if the cooling rate of the sample is very slow for the so-called relaxed state.[54]

The material has a metallic chain-axis DC resistivity that decreases as the temperature is lowered, which is shown in Fig. 5.3.[4] Surprisingly, the far-infrared conductivity is much lower than the DC value, while the imaginary part of the conductivity shows that there is a considerable spectral weight at low frequencies. These observations have led to the suggestion that a narrow, possibly collective, mode at zero frequency carries the transport current at low temperatures.[55] The first experimental evidence of such a mode was found in the one-dimensional organic compound (TTF-TCNQ) above the Peierls charge-density-wave (CDW) transition temperature ($T_c \cong 58$ K) along the chain axis.[56] This narrow mode has been ascribed, by Bardeen[57] and Lee et al.,[58] to a one-dimensional sliding CDW collective mode first discussed by Fröhlich.[59] Along with the collective mode, a pseudo-gap, which is due to the fluctuations of the CDW instability [or the spin-density-wave (SDW) instability in other one-dimensional organic materials] that pertains to the one-dimensional system, appears in the single-particle part of the conductivity spectrum of (TTF-TCNQ) between the mean-field transition temperature T_c and the three-dimensional Peierls ordering temperature T_c^{3D}. The pseudogap develops into a real gap below T_c^{3D}.[60]

In accordance with this idea a large NMR relaxation rate T_1^{-1} anomaly [a large enhancement of the relaxation rate in comparison with the Korringa law, *i.e.*, the linear temperature dependence which holds for $T>25$ K] of $(TMTSF)_2ClO_4$ was found in the relaxed state for $T<25$ K, as shown in Fig. 5.4 (a), and is attributed to the existence of large non-critical antiferromagnetic spin fluctuations in this temperature region.[61] The

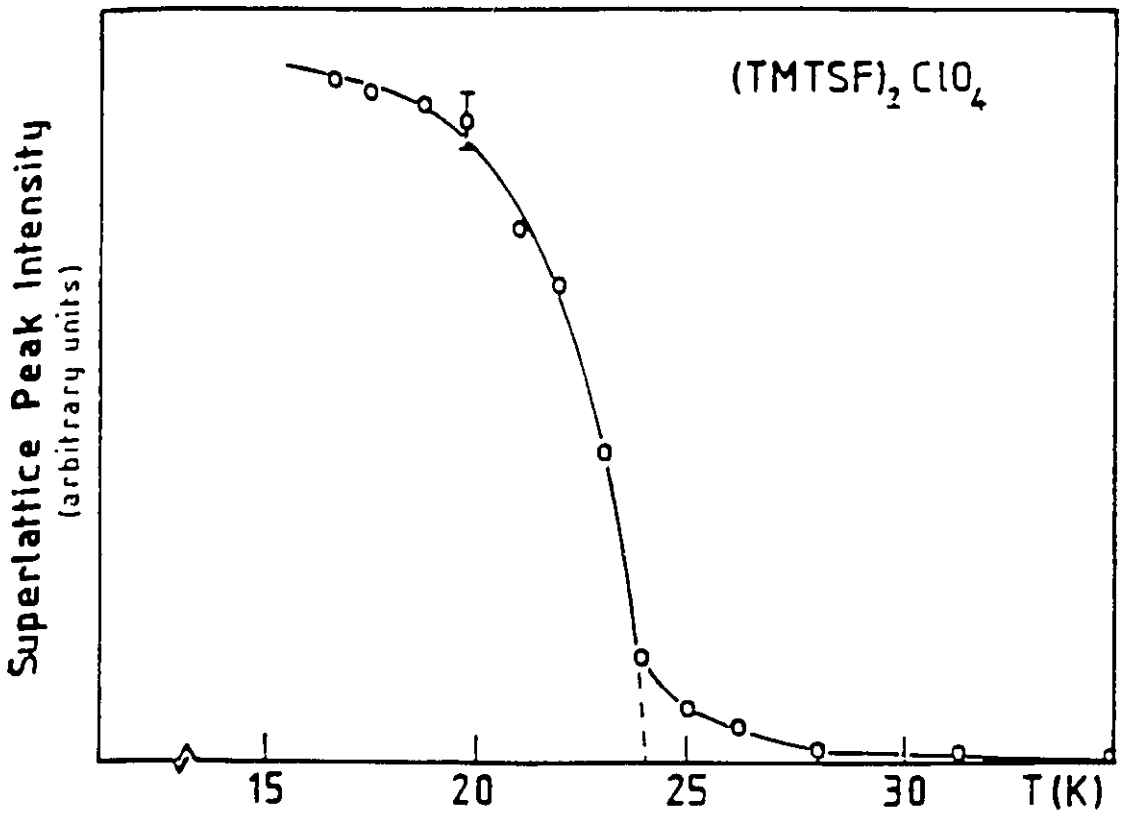

Figure 5.2. Temperature dependence of the superlattice x-ray reflectance intensity of $(TMTSF)_2ClO_4$ measured by Pouget *et al.*, which shows that an anion ClO^- disorder-order phase transition occurs at 24 K. From Ref. 54.

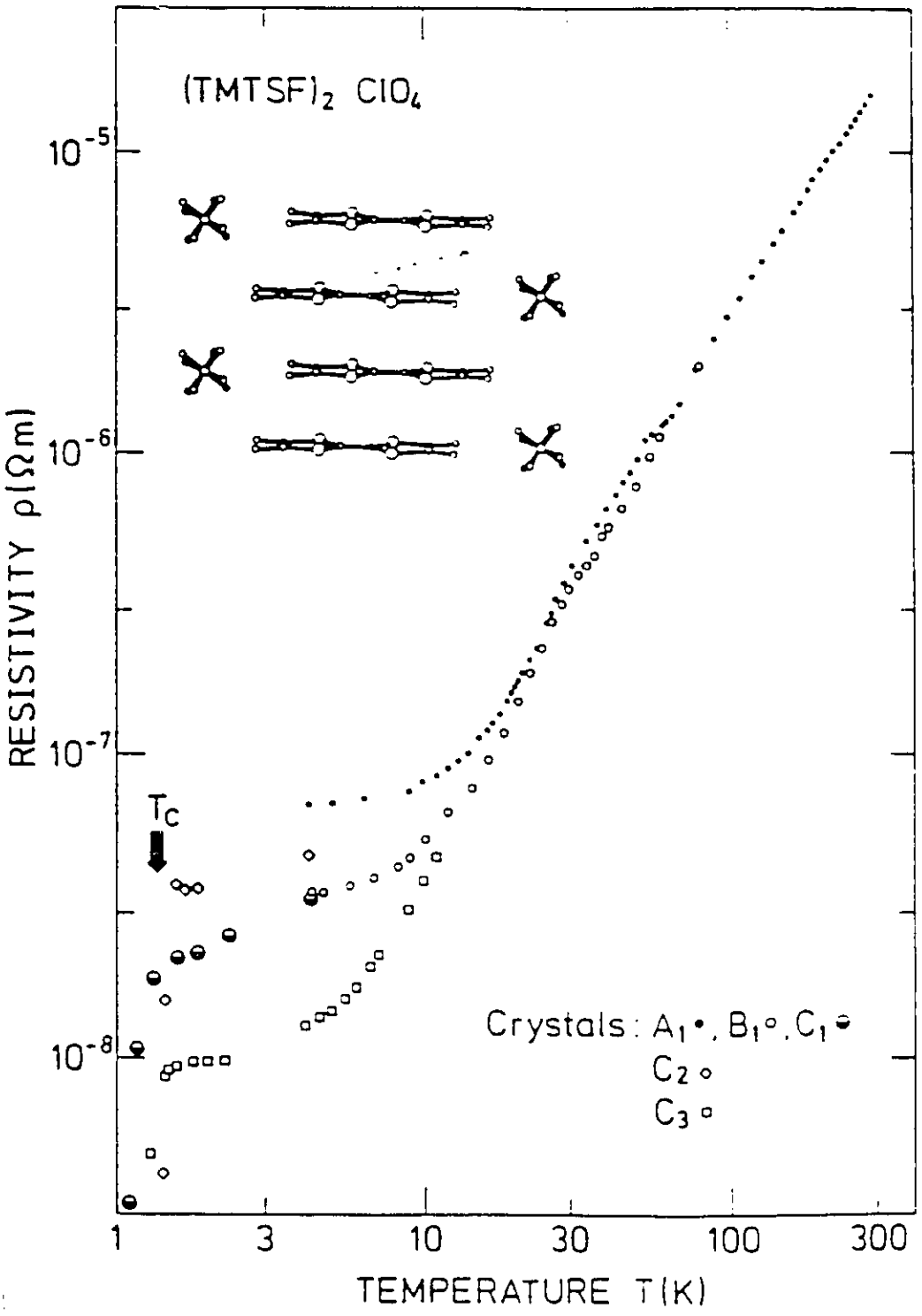

Figure 5.3. Temperature dependence of the longitudinal resistivity of $(TMTSF)_2ClO_4$ along the chain axis, measured by Bechgaard *et al.*, for different crystals. From Ref. 4.

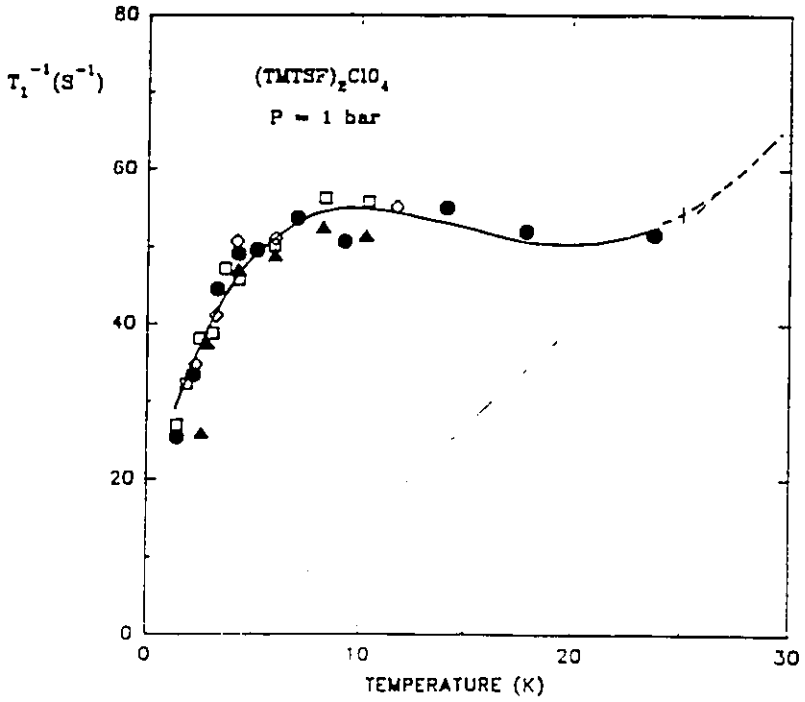

(a)

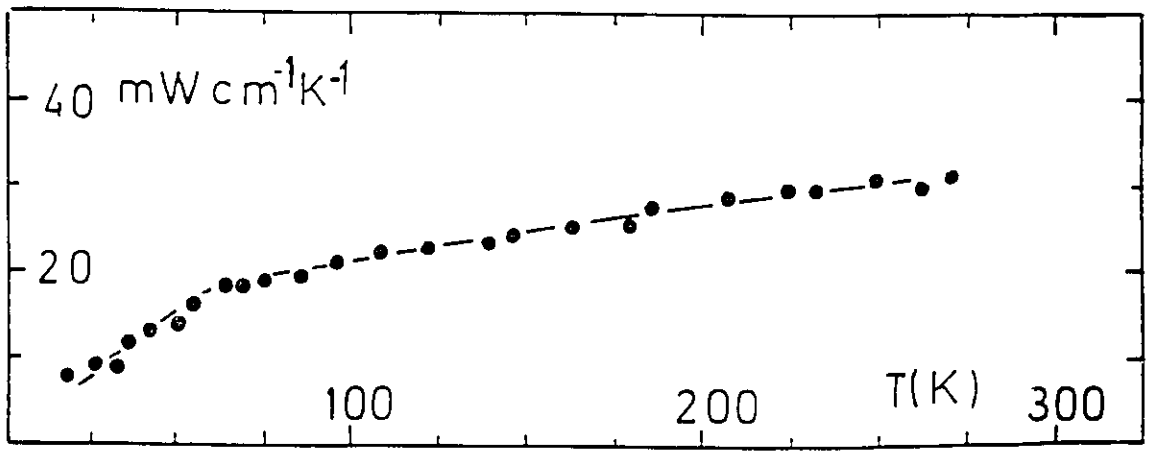

(b)

Figure 5.4. (a) ^{77}Se T_1^{-1} *vs* T data of $(TMTSF)_2ClO_4$ measured by Wzietek *et al.* in the relaxed state: full circles, 31.9 kG// **b'**; full triangles, 6.0 kG (powder); open squares, 31.9 kG// **c***; open diamond-shaped, 21 kG// **b'**. From Ref. 61; **(b)** Thermal conductivity of $(TMTSF)_2ClO_4$ measured by Djurek *et al.* From Ref. 62.

thermal conductivity of $(TMTSF)_2ClO_4$ exhibited in Fig. 5.4 (b) shows a suppression of κ below 60 K that is interpreted as due to the opening of a pseudo-gap in the single-particle density of states.[62,63] A formation of SDW below 5.5 K has also been verified by Walsh *et al.* using the conduction-hole spin resonance technique.[64]

Reflectance spectroscopy is a powerful technique that can be used to explore low-lying electronic excitations in solids. The far-infrared reflectance of $(TMTSF)_2ClO_4$ along the chain axis (the highly conducting direction) has been measured by Ng *et al.* in the temperature range between 2 and 60 K for frequencies up to ~60 cm^{-1} only, which is shown in Fig. 5.5 (a).[5] The derived far-infrared conductivity, displayed in Fig. 5.5 (b), is quite small in comparison with the much larger DC conductivity (Fig. 5.3) and non metallic, *i.e.*, decreasing with decreasing temperature and frequency, whereas the DC conductivity shows a monotonic metallic increase with decreasing temperature. The results of Ng *et al.* also show that there are two temperature-dependent phonon resonances at 7 and 25 cm^{-1} whose intensity increases as the temperature is reduced below 60 K. Eldridge and Bates used a composite-bolometer technique to measure the reflectance of $(TMTSF)_2ClO_4$ between ~5 and 1000 cm^{-1} at 6 K.[65] The result along the chain axis is quite different from that of Ng *et al.* that is probably due to the multiple thermal cyclings of their sample. The derived optical conductivity starts to rise at ~200 cm^{-1} and has a peak near 500 cm^{-1} that was accounted for in terms of a Holstein process (we disagree with this explanation and will later assign the feature to an indication of opening of a gap).

Kikuchi *et al.* have measured the chain-axis reflectance of $(TMTSF)_2ClO_4$ from 5000 to 10,000 cm^{-1} (up to 25,000 cm^{-1} for room temperature only) at temperatures between 30 and 290 K, exhibited in Fig. 5.6.[66] The behavior of the temperature-dependent

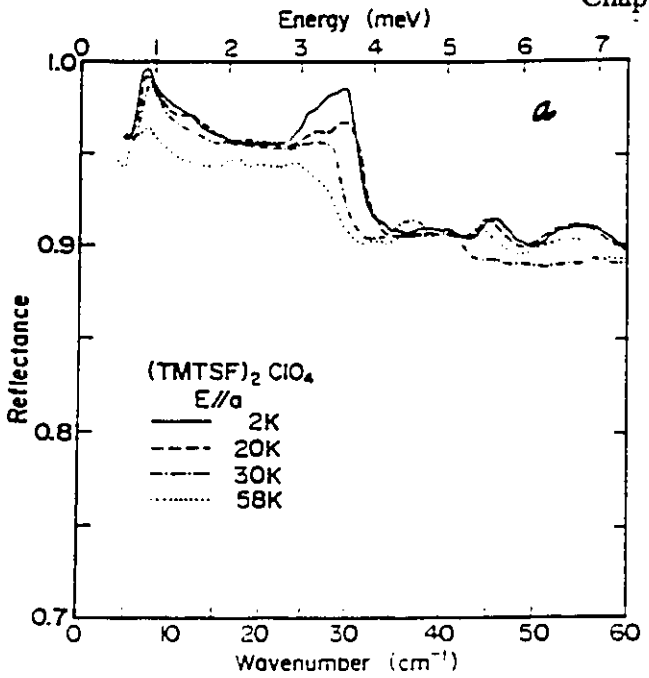

(a)

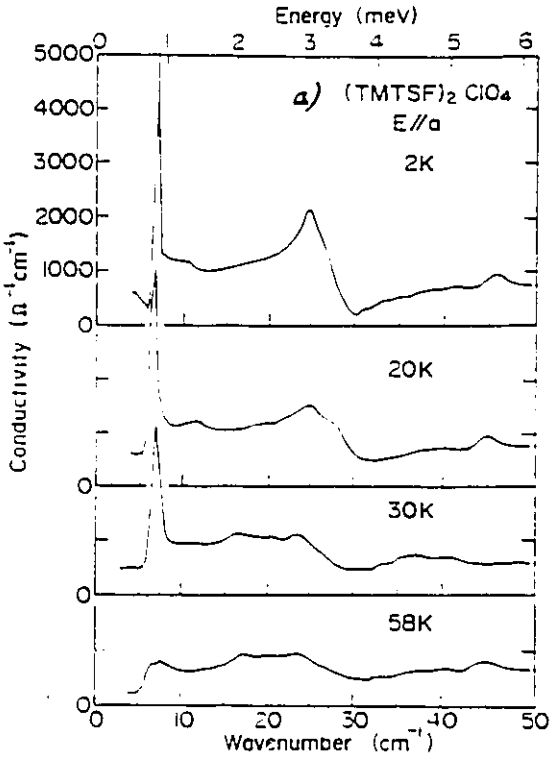

(b)

Figure 5.5. **(a)** Temperature dependence of the polarized reflectance of $(TMTSF)_2ClO_4$ along the chain axis measured by Ng *et al.*; **(b)** Temperature dependence of the far-infrared optical conductivity of $(TMTSF)_2ClO_4$ along the chain axis. From Ref. 5.

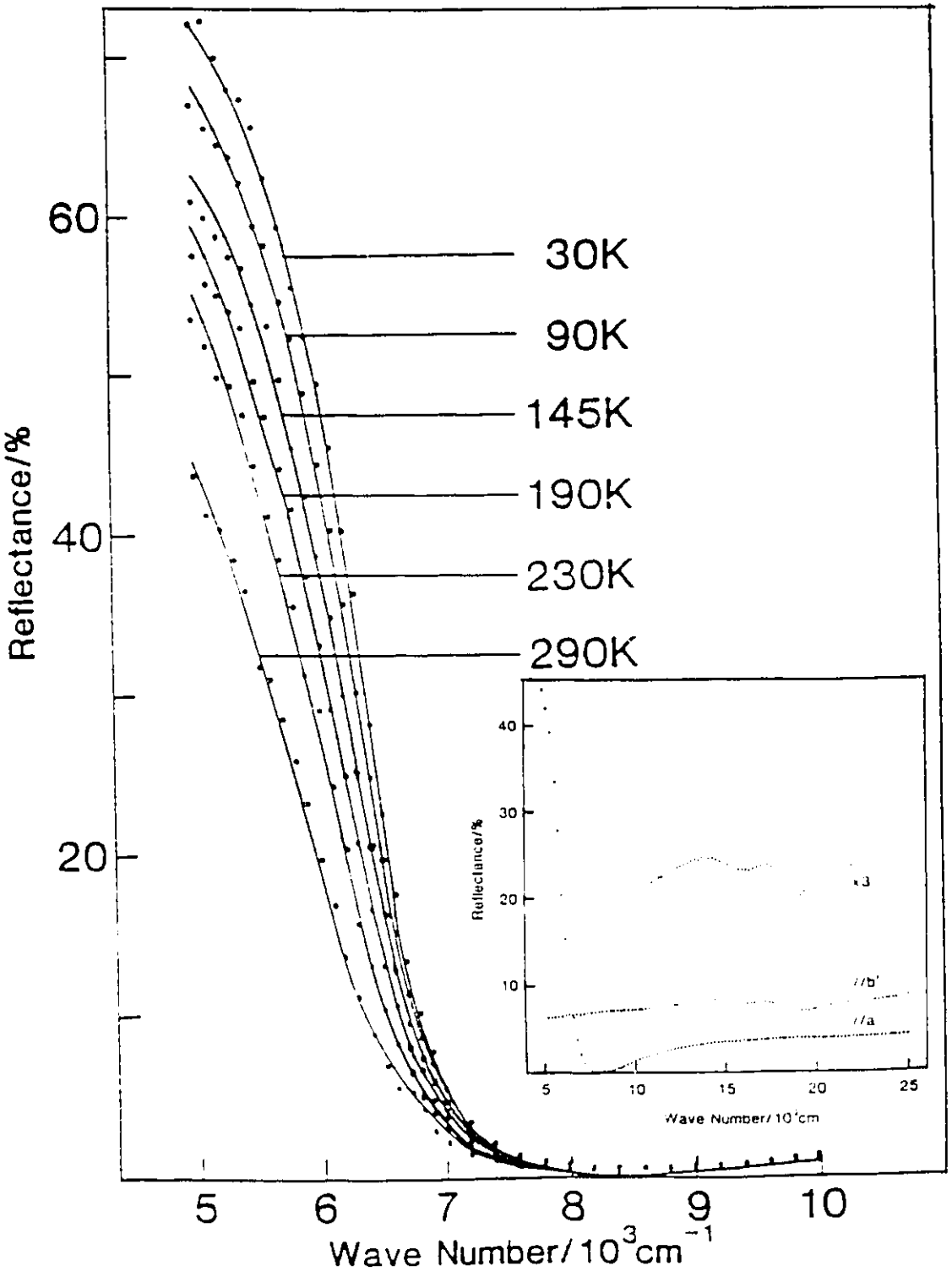

Figure 5.6. Temperature dependence of the polarized reflectance of $(TMTSF)_2ClO_4$ along the chain axis between ~5000 and 10,000 cm^{-1} measured by Kikuchi *et al.* The inset shows the room-temperature data up to 25,000 cm^{-1}. From Ref. 66.

reflectance is metallic and a Drude-like plasma edge was found near 7000 cm^{-1}. This raises a question of why the optical properties of $(TMTSF)_2ClO_4$ along the chain direction are so different in the far-infrared and the higher frequency region. Recently, room-temperature polarized reflectance data of $(TMTSF)_2ClO_4$ along the chain axis have been published by Pedron *et al.* from ~10 to ~10,000 cm^{-1} in which several vibration peaks including the one at ~1300 cm^{-1} are superimposed on the background and a sharp plasma edge occurs at 7000 cm^{-1}.[67] In view of this, superficially contradictory data, it is important to complete the measurements of the chain-axis reflectance of $(TMTSF)_2ClO_4$ in the missing frequency range at low temperatures.

5.2 Optical Properties of $(TMTSF)_2ClO_4$ along the chain axis

The typical dimensions of a crystal of $(TMTSF)_2ClO_4$ is 3.0×0.5×0.2 mm^3 in the a, b, and c directions, respectively. To obtain a reasonable signal to noise ratio we made a mosaic: carefully gluing several crystals (the a-b plane facing up) onto the top flat surface (~2.5 mm in diameter) of the cone-shaped sample holder with the longest dimension, the chain axis, of the crystals parallel to each other. The temperature dependence of the polarized reflectance of the $(TMTSF)_2ClO_4$ single crystals along the chain axis was measured from 60 to 8000 cm^{-1} for temperatures between 10 and 300 K using a Michelson interferometer. The sample was cooled slowly below 40 K (~1 K/min.) for ensuring that it is in the relaxed state.

Fig. 5.7 shows the polarized reflectance of $(TMTSF)_2ClO_4$ at 300, 200, 100, and 10 K along the chain axis. Our room-temperature data are quite similar to those given by Pedron *et al.* except for a few percent magnitude difference between their data and our

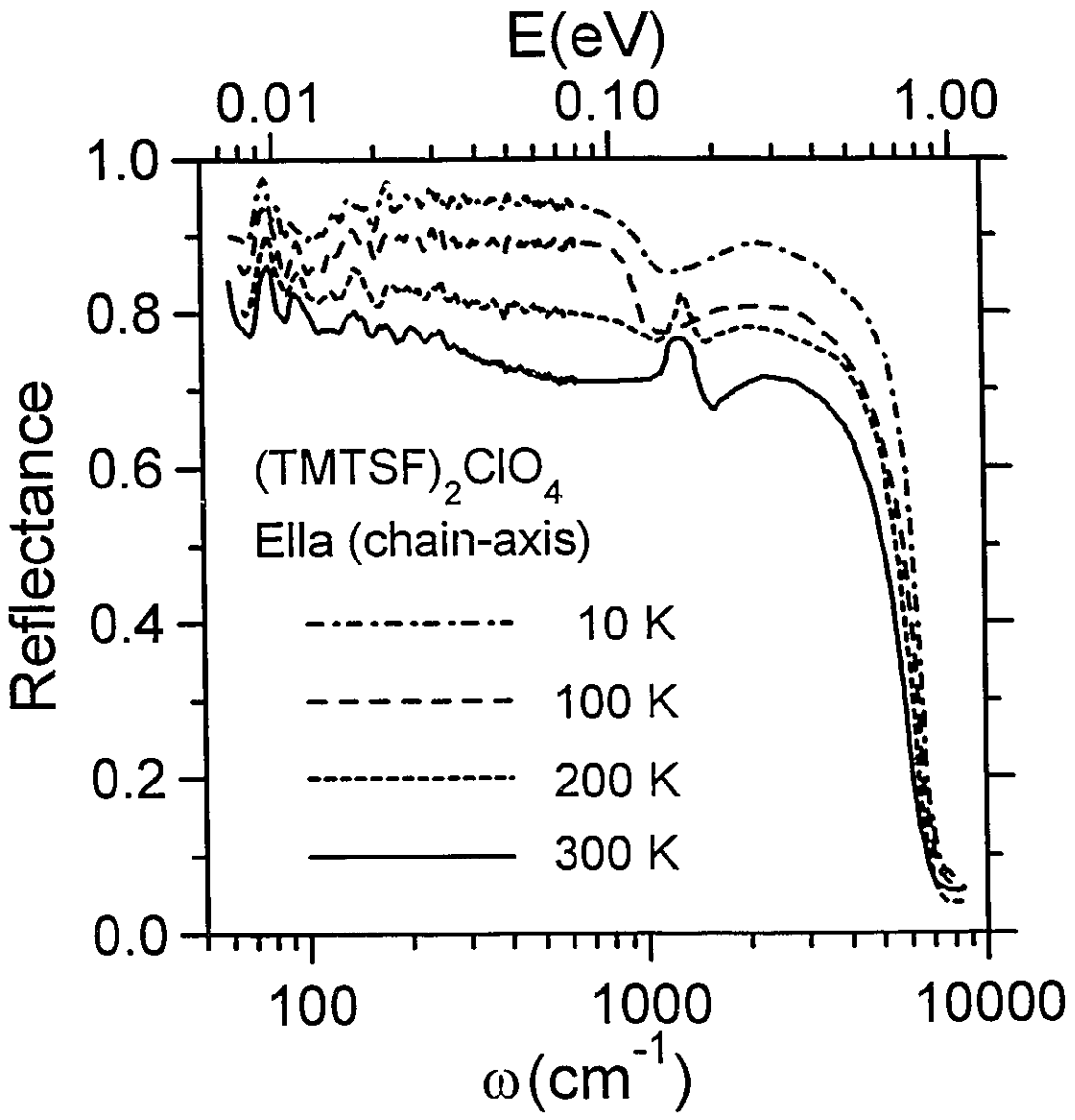

Figure 5.7. Frequency dependence of the polarized reflectance of $(TMTSF)_2ClO_4$ along the chain axis at 300, 200, 100, and 10 K.

data.[67] The reflectance at high frequencies increases as the temperature is lowered and a plasma edge near 7000 cm^{-1} is clearly shown up at all temperatures in agreement with the results of Kikuchi *et al.*[66] A phonon peak is seen near 1300 cm^{-1} at 300 and 200 K and as the temperature is further reduced, the resonance peak is turned into an antiresonance dip. Meneghetti *et al.* have studied vibrational behavior of $(TMTSF)_2X$ using Raman and infrared techniques.[68] According to their results, this phonon may probably be assigned to the activated mode that results from the strongly coupling between the internal C=C stretch mode (a_g,ω_4) (polarizing along the direction perpendicular to the chain axis) and the conduction electron[69] in the TMTSF molecules. In the far-infrared region there are several induced phonons superimposed on the reflectance background at all temperatures. The reflectance decreases with increasing frequency at 300 and 200 K. A more interesting behavior occurs at the temperatures below 100 K: The reflectance background saturates between 170 and 700 cm^{-1}, but, is depressed below 170 cm^{-1}. Note that the magnitude of the 10 K reflectance is about 95% between 170 and 700 cm^{-1} and matches the data point of Ng *et al.* at 60 cm^{-1}.[5]

To understand the optical properties of the material more clearly we perform Kramers-Kronig analysis to get the frequency dependent conductivity and dielectric function. To do this the reflectance data need to be extrapolated at both ends of the frequency range. On the higher-frequency side, we extend our data using the room-temperature data measured by Kikuchi *et al.* for frequencies between 8000 and 25,000 cm^{-1},[66] a constant value between 25,000 and 10^6 cm^{-1}, and free electron behavior [$R(\omega) \propto \omega^{-4}$] beyond 10^6 cm^{-1}. On the lower-frequency side, our reflectance data below 60 K are extended to ~5 cm^{-1} using the data of Ng *et al.*[5] Below the experimental limit, as far as the DC conductivity behavior is concerned, the Hagen-Rubens approximation [$1 - R(\omega) \propto \sqrt{\omega}$] with the corresponding DC conductivity value[4] is customarily used to

extrapolate the reflectance to zero frequency. However, for the organic conductor $(TMTSF)_2ClO_4$, one must be careful to choose a proper extrapolation at low temperatures because the DC conductivity in the low temperature region results from the narrow collective mode at origin, which is supported by a negative, zero-frequency mode of the real part of the dielectric function $\varepsilon_1(\omega)$, and the Hagen-Rubens approximation is not valid at the frequency where our measured reflectance data stop. To do the extension properly we assume the narrow mode has a Drude shape and fit the reflectance data at 10, 20, and 60 K to a high-frequency dielectric constant term $\varepsilon_\infty(\cong 4)$, a Drude term with the known DC conductivity, and a series of Lorentz oscillators that represent the rest of the infrared conductivity. The fitting parameters are listed in Table 5.1 at the end of this chapter. We then use the fitted reflectance as the low-frequency extension in the Kramers-Kronig analysis of the actual data.

Figs. 5.8 (a) and (b) show the reflectance and the corresponding real part of the AC conductivity of $(TMTSF)_2ClO_4$ along the chain axis at 10 and 60 K for frequencies up to 20 cm^{-1}, respectively (the extrapolated data are plotted as the dashed lines). Note that the extrapolated data are smoothly connected to the measured data and the reflectance plasma edge near ~5 cm^{-1}, which is shown in Fig. 5.8 (a) and leads to a narrow zero-frequency mode (the width γ_c<0.5 cm^{-1}, see later) in $\sigma_1(\omega)$ [shown in Fig. 5.8 (b)], matches the slight up-turn in the real data near the end of the measured region. The real part of the AC conductivity of $(TMTSF)_2ClO_4$ along the chain axis in far-infrared together with the corresponding values of the DC conductivity of $(TMTSF)_2ClO_4$ measured by Bechgaard *et al.*[4] are shown in Fig. 5.9 (the 10 K DC value, ~1.96×10^5 $\Omega^{-1}cm^{-1}$, is too high to be indicated on the scale of the ordinate shown in the figure). The conductivity at 10 K has some interesting features: several very sharp induced phonons are superimposed

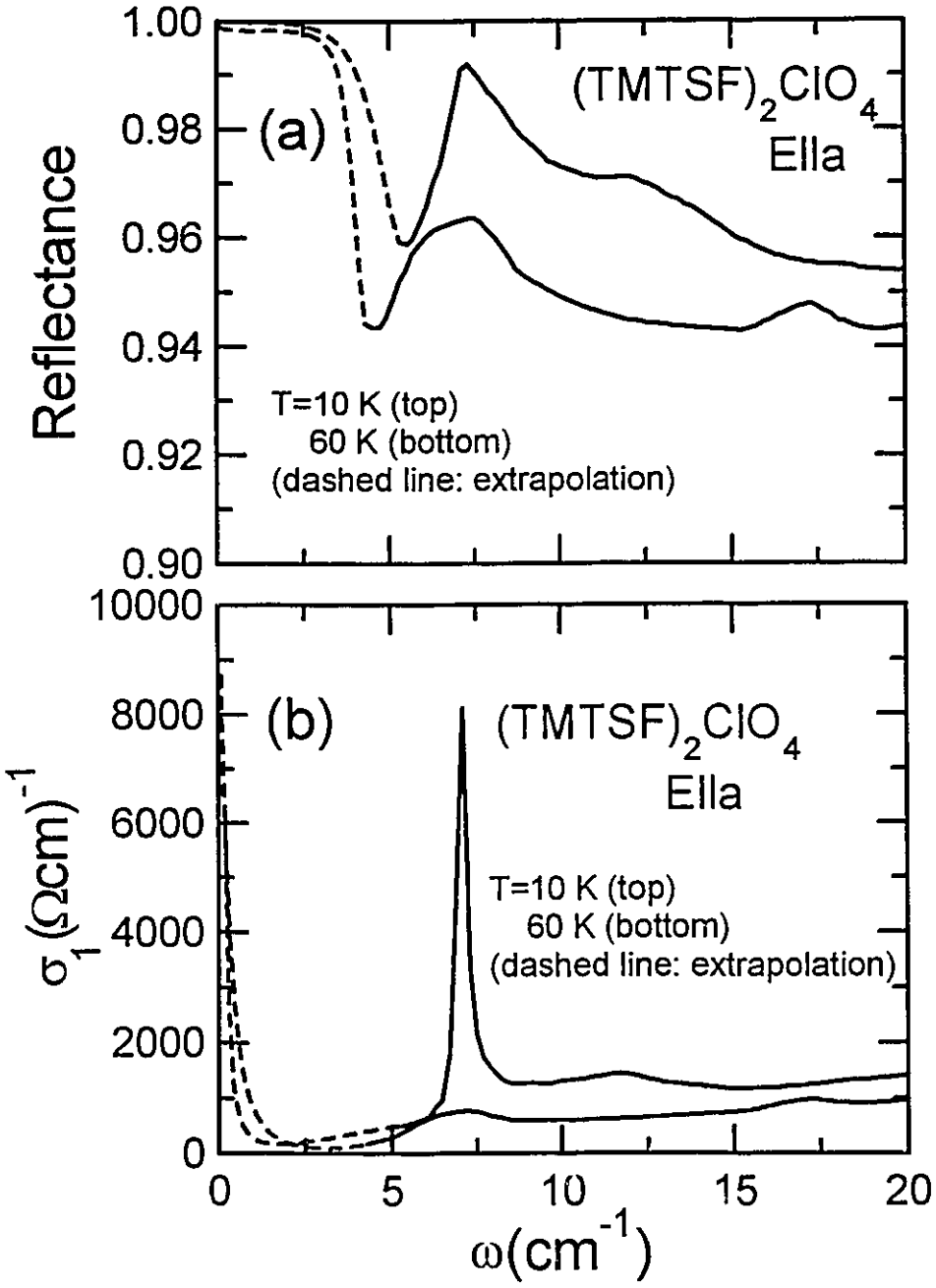

Figure 5.8. (a) Frequency dependence of the chain-axis reflectance of $(TMTSF)_2ClO_4$ up to 20 cm^{-1} at 10 and 60 K measured by Ng *et al.* (Ref. 5). The dashed line is the extrapolated data obtained using the procedure that is described in the text; **(b)** Real part of the chain-axis AC conductivity of $(TMTSF)_2ClO_4$ *vs.* frequency at 10 and 60 K. The data below 5 cm^{-1} where the reflectance was extrapolated are displayed in the dashed line.

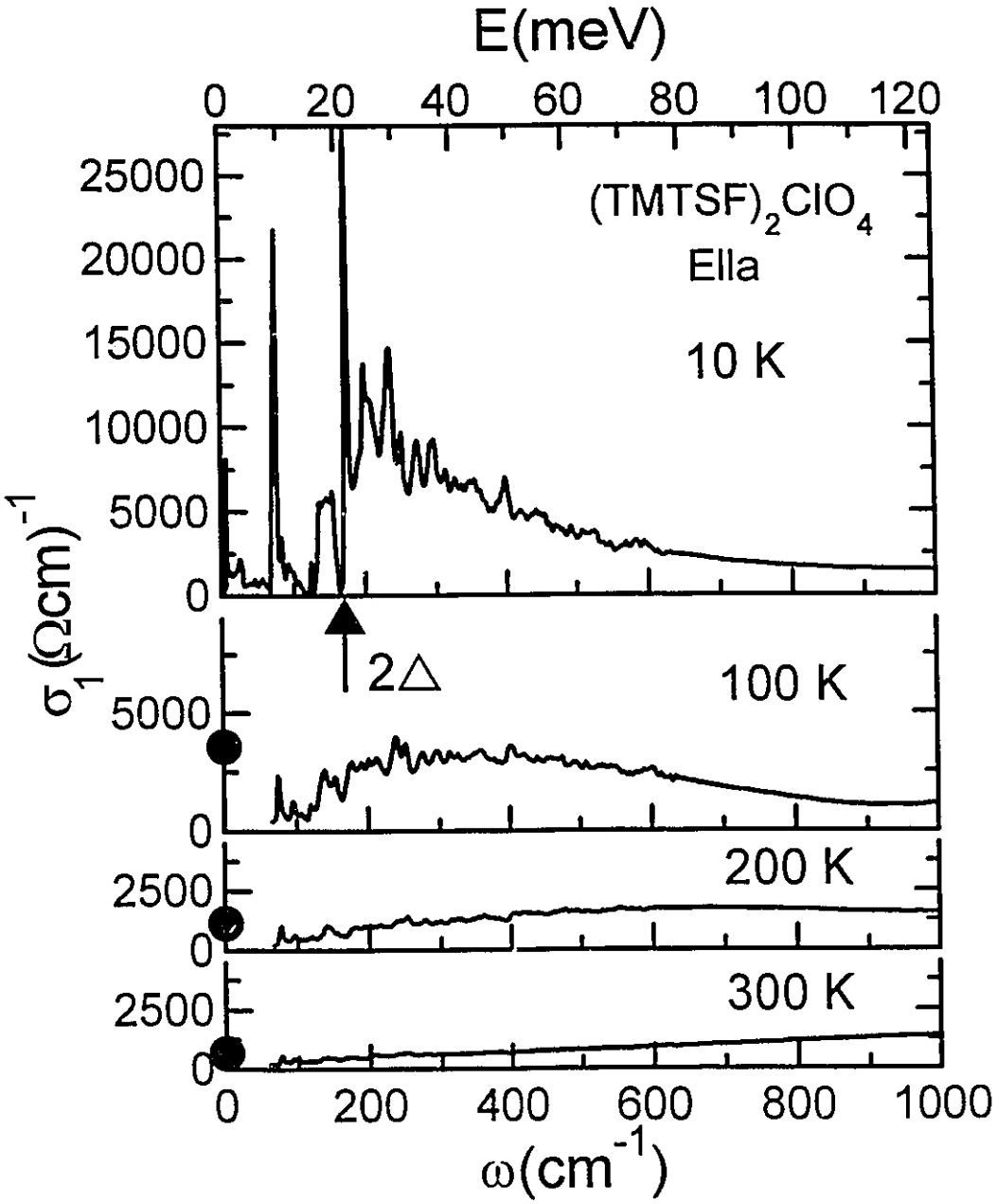

Figure 5.9. Real part of the chain-axis AC conductivity of $(TMTSF)_2ClO_4$ at 300, 200, 100, and 10 K. The values of the DC conductivity of $(TMTSF)_2ClO_4$ measured by Bechgaard *et al.* (Ref. 4) at 300, 200, and 100 K are indicated as the filled circles on the left vertical axis (the 10 K DC value, ~1.96×10^5 $\Omega^{-1}cm^{-1}$, is too high to be denoted on the vertical scale shown.). A gap with the value $2\Delta\cong170$ cm^{-1} (~21 meV) is clearly exhibited in the 10 K conductivity spectrum.

on the background and the background is suppressed for frequencies below 170 cm^{-1} which indicates the formation of a gap $2\Delta \cong 21$ meV. The background has a shape of the square-root edge above 170 cm^{-1}. As mentioned above, Eldridge and Bates found that the chain-axis conductivity of $(TMTSF)_2ClO_4$ at 6 K begins to rise at ~200 cm^{-1} and has a peak near 500 cm^{-1}.[65] We believe that the proper explanation for this feature is the opening of a gap near the lower frequency scale (~200 cm^{-1}). With increasing temperature, the intensity of the induced phonons decreases. The pseudo-gap-like feature can still be seen in the conductivity spectrum at 100 K. Note that to reconcile the far-infrared conductivity data with the DC data below 100 K one must assume that a zero-frequency mode carries the transport current at low temperatures. With decreasing temperature the mode becomes narrower and sharper. In contrast, the conductivity at 200 and 300 K increases with increasing frequency which is characteristic of the $(TMTSF)_2X$ salts;[70,71,72] no gap-like feature is found; the extrapolation to zero frequency agrees fairly well with the DC conductivity value.

As introduced at the beginning the NMR measurement result indicates that there exist the large non-critical antiferromagnetic spin fluctuations in the relaxed state of $(TMTSF)_2ClO_4$ for temperatures below 25 K.[61] This long-range ordering of SDW could be accompanied with a pseudogap opening at the Fermi level,[73] which has been seen in the thermal conductivity result.[62] Therefore, the gap found in this work is tentatively attributed to the formation of the long-range ordering of SDW at low temperatures. However, our results indicate that the precursors of the SDW gap exist as high as 100 K which can be accounted for by an effect of the one-dimensional fluctuation though the interchain coupling along the b axis is large for $(TMTSF)_2ClO_4$ at low temperatures.[70] The fluctuation effects at a Peierls transition in a one-dimensional conductor has been studied by Lee *et al.*[74] By calculating the temperature dependent correlation length $\xi(T)$

they found that for temperatures between T_c and $(1/4)T_c$, where T_c is the mean-field transition temperature, $\xi(T)$ increases approximately linearly with decreasing temperature; however, with further decreasing temperature $\xi(T)$ increases exponentially, characteristic of a three-dimensional ordering with the critical temperature $T_c^{3D} \approx (1/4)T_c$. The value of T_c for $(TMTSF)_2ClO_4$ could be estimated using the mean-field relation $2\Delta = 3.5k_BT_c$ to be $\cong$ 70 K so that the corresponding three-dimensional spin Peierls transition temperature of $(TMTSF)_2ClO_4$ $T_c^{3D} \approx 18$ K which is in good agreement with the value derived from the NMR result.

In studying the conductivity mechanism of one-dimensional organic systems Rice *et al.* have presented a model of the phase phonon excitation along the chain direction. In this model, the coupling between the intramoleclar, infrared-inactive, symmetric vibrational mode a_g and the conduction electron along the chain axis gives rise to this excitation.[69] The model also predicts that below the Peierls transition temperature the phase-phonon resonance at $\omega<2\Delta$ is much sharper in comparison with the one at $\omega>2\Delta$. This is caused by lack of damping for the phonon in the gap region *via* electron-hole-pair excitation. Note from the conductivity spectrum at 10 K (Fig. 5.9) that the phonons below 2Δ, *e.g.*, the one at ~ 75 cm^{-1} and the another one at ~ 2Δ, are much sharper than the ones above 2Δ. This behavior gives us another criterion to determine the gap value.

It can be seen from the conductivity spectra shown in Fig. 5.9 that with the development of the SDW gap the single-particle excitonic spectral weight shifts from high to low frequencies and, at the same time, the intensity of the induced phonons increases drastically. The similarity of the temperature dependence of these two quantities suggests that they are related to each other. The structure of $(TMTSF)_2ClO_4$, obtained from neutron diffraction, shows that a lattice dimerization (LD) develops with decreasing

temperature: the difference between d_1 and d_2 (d_1 and d_2 are the intrastack distances within the unit cell along the chain direction, respectively) is 0.00 Å at room temperature, 0.01 Å at 125 K, and 0.04 Å at 7 K.[53] A model has been presented by Bozio *et al.* for the $(TMTSF)_2ClO_4$ organic salt in which the lattice distortion from a small amplitude LD leads to the doubling of the periodicity of the regular chain spacing a.[75,67] This doubling in turn causes the opening of a $\pm k_F$ narrow gap along the chain direction at the Fermi surface that may correspond to the gap found in the conductivity spectra. As the gap develops the conductivity spectral weight shifts from high to low frequencies which is also the case of $(TMTSF)_2PF_6$.[70] On the other hand, this model also suggests that the electron-molecular vibration coupling gives rise to the activation of an arbitrary number of internal modes (a_g) along the chain axis. The activation of the a_g modes at $\omega<2\Delta$ is closely related to the non-zero value of the gap induced by LD and is responsible for the additional structures within the gap region of the conductivity spectrum. Therefore, we can choose either of these two quantities as an order parameter. The integrated spectral weight between 2Δ and 1000 cm^{-1} as a function of temperature is shown in Fig. 5.10. The spectral weight in this frequency range decreases sharply with increasing temperature between 10 and 100 K. Fig. 5.11 shows the temperature dependence of the integrated intensity of one of the induced phonons around 76 cm^{-1}, together with the temperature dependence of the spectral weight for the zero-frequency narrow mode that will be discussed below. The intensity of the induced phonon drops sharply as the temperature is increased and levels off for $T>100$ K. It is concluded from these results that precursors of the SDW gap that are caused by the effects of the one-dimensional SDW fluctuations can be seen in the temperature range between 25 and ~ 100 K.

As mentioned above, we fit the chain-axis reflectance of $(TMTSF)_2ClO_4$ below

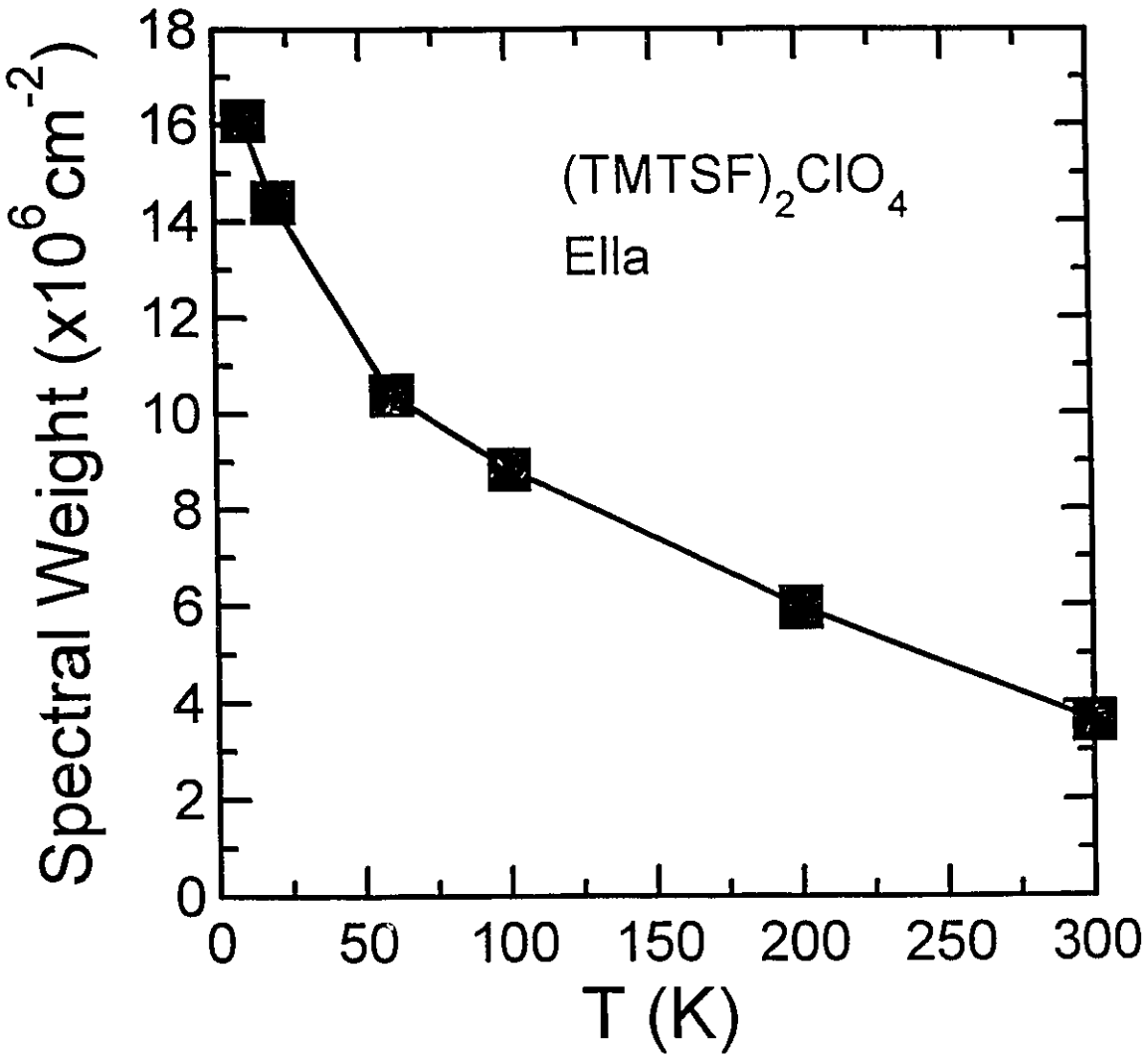

Figure 5.10. Integrated spectral weight in the chain-axis conductivity spectra of $(TMTSF)_2ClO_4$, shown in Fig. 5.9, between 2Δ ($\cong$170 cm^{-1}) and 1000 cm^{-1} as a function of temperature. The solid line is a guide to the eye.

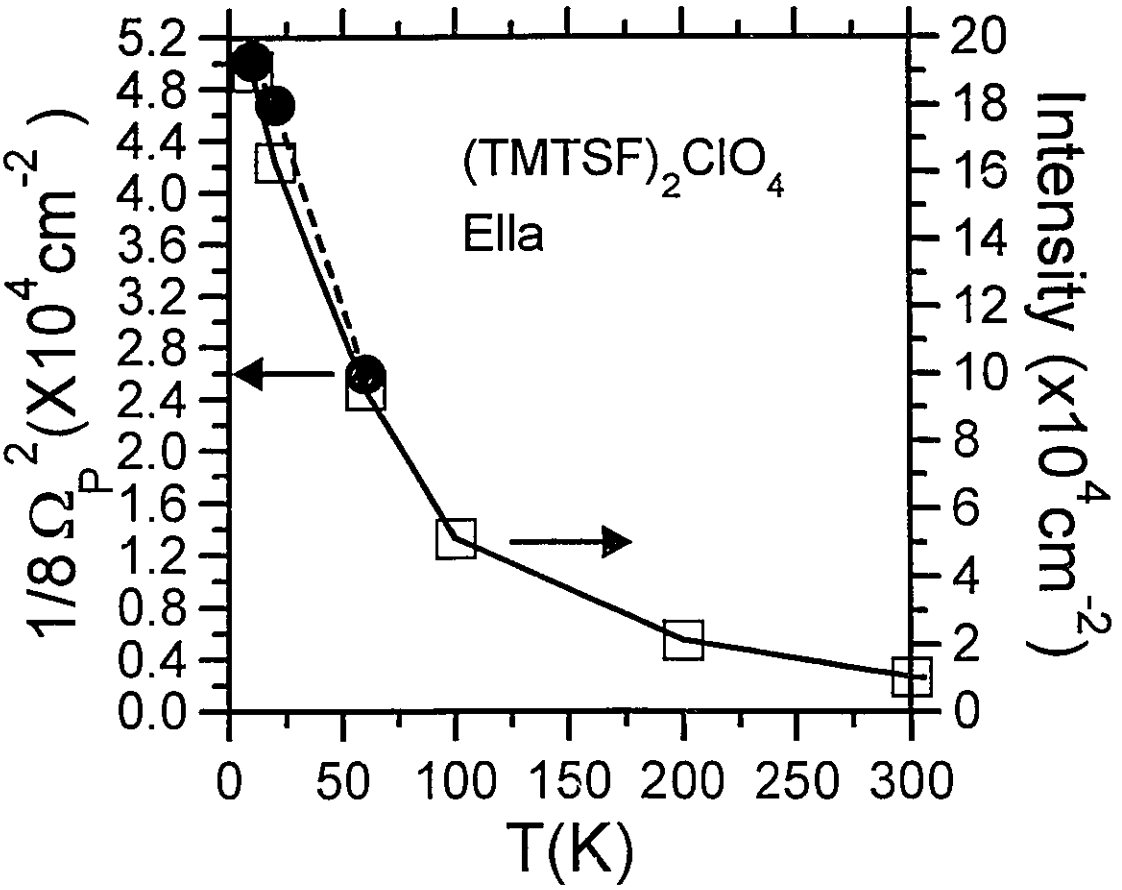

Figure 5.11. Temperature dependence of the spectral weight $(1/8)\Omega_P^2$ for the zero-frequency narrow mode of $(TMTSF)_2ClO_4$ below 60 K, shown as the filled circles with the scale of the left vertical axis, and the integrated intensity of the induced phonon around 76 cm^{-1} of $(TMTSF)_2ClO_4$, shown as the squares with the scale of the right vertical axis. The dashed and solid lines are guides to the eye.

60 K to a high-frequency dielectric constant term $\varepsilon_\infty(\cong 4)$, a Drude term (with the known DC conductivity value) that simulates the narrow mode at zero frequency, and a series of Lorentz oscillators. The Drude parameters obtained from this fitting are listed in Table 5.1 at the end of this chapter, from which one can see that the value of the plasma frequency Ω_F decreases with increasing temperature. According to the sum rule, the spectral weight of this narrow mode is equal to $(1/8)\Omega_p^2$. The temperature dependence of the spectral weight for the narrow mode below 60 K is shown in Fig. 5.11. The fact, shown clearly in the figure, that both temperature dependent spectral weights for the zero-frequency narrow mode and the 76 cm^{-1} induced phonon are similar to each other indicates that *they have the same collective-excitation origin*. This behavior is very important because it rules out the possibility of the single-particle contribution to the DC conductivity in this material.

Recently, a microwave [16.5 GHz (~0.5 cm^{-1})] dielectric study of $(TMTSF)_2AsF_6$, one member of the $(TMTSF)_2X$ series, shows that for $T>T_c$ (T_c is the SDW transition temperature in this salt which is equal to ~12 K), the chain-axis microwave conductivity is smaller than the chain-axis DC value, *e.g.*, at 14 K the microwave conductivity drops to 72% of the corresponding DC value, whereas the microwave conductivity is much larger than the DC value for $T<T_c$.[76] Note that this microwave dielectric result is in agreement with the far-infrared polarized reflectance result obtained by Ng *et al.*[71] This indicates that above T_c the collective mode is located at zero frequency which carries a large DC current, but below T_c the mode is pinned at a finite frequency which makes a much smaller contribution to the DC conductivity (only by its tail at zero frequency). The same behavior has also been found in the one-dimensional (TTF-TCNQ) salt.[56] For another extensively

studied one-dimensional organic salt $(TMTSF)_2PF_6$, the longitudinal DC resistivity at ambient pressure shows a minimum at $T_\rho \cong 15$ K which is due to the transition to a long-range ordering of SDW.[77] The longitudinal microwave [16.5 GHz (~0.5 cm^{-1})] conductivity of $(TMTSF)_2PF_6$ at ambient pressure is much larger then the corresponding DC conductivity for $T<T_c(=T_\rho)$ which indicates that there is a collective mode pinned in the microwave frequency region.[78] This long-range SDW transition can be suppressed by applying a pressure $p \geq p_c (\cong 9$ kbar) which also leads to a superconducting transition at ~1 K[79] [the DC conductivity behavior of $(TMTSF)_2PF_6$ under the pressure $p \geq p_c$ is much like that of $(TMTSF)_2ClO_4$ at ambient pressure]. It is reasonable to assume that the applied pressure ($p \geq p_c$) causes the collective mode of $(TMTSF)_2PF_6$ to move to zero frequency (depinning). The ^{77}Se NMR relaxation rate T_1^{-1} of $(TMTSF)_2PF_6$ under pressure has been measured[80] and the result shows that for $p<p_c$ T_1^{-1} diverges as $(T-T_N)^{-1/2}$, but for $p \geq p_c$ this divergence of T_1^{-1} that results from a long-range critical SDW fluctuations is suppressed and the behavior of T_1^{-1} is quite similar to that of $(TMTSF)_2ClO_4$ shown in Fig. 5.4 (a), which is attributed to a short-range non-critical SDW fluctuations mentioned before. From these results we believe that whether the collective mode in the conductivity spectrum is pinned at a finite frequency or located at zero frequency has strong influence on the behavior of the NMR relaxation rate, *i.e.*, whether it exhibits long-range critical or short-range non-critical SDW fluctuations. The far-infrared results in this work and in the other groups' work[70,71] show that the low-temperature single-particle part of the chain-axis conductivity for $(TMTSF)_2X$ with $X=ClO_4$, PF_6, and AsF_6 always remains the same, *i.e.*, a gap-like feature appears in $\sigma_1(\omega)$ below 200 cm^{-1} at low temperatures, no matter what the material is in a long-range critical or a short-range non-critical SDW fluctuation state at low temperatures. However, in order to achieve the superconductivity for $(TMTSF)_2PF_6$ at low temperature, one must suppress the long-range critical SDW fluctuations, while at the same time the resistivity

minimum, shown in the DC resistivity curve at ambient pressure around 15 K, no longer appears that corresponds to the depinning of the collective mode so that the mode can carry the transport current.

Fig. 5.12 shows the frequency dependence of the real part of the dielectric function $\varepsilon_1(\omega)$ along the chain axis at 10, 100, 200, and 300 K. From the figure one can see that there are several induced phonon modes whose intensity decreases with increasing temperature. Note that $\varepsilon_1(\omega)$ at 10 K tends to decline rapidly to large negative values at the end of the low-frequency region which indicates the development of the narrow mode discussed before. Also, it is noted that there is a strong mode around 23 cm^{-1} in the 10 K curve. Although the optical conductivity is suppressed in far-infrared due to the opening of a SDW gap at low temperatures, the DC conductivity of $(TMTSF)_2ClO_4$ continues to show metallic behavior with a much higher value. The suggestion that there must be a narrow zero-frequency mode to carry the DC current at low temperatures has been supported by both the fitting of the reflectance data and the $\varepsilon_1(\omega)$ data. The following method used by Jacobsen *et al.*,[70] gives us another way to estimate the width γ_c and plasma frequency Ω_P for this mode. The 10 K complex dielectric function $\tilde{\varepsilon}(\omega)$ below 30 cm^{-1} can be expressed as follows,

$$\tilde{\varepsilon}(\omega) = \varepsilon_\infty + \frac{{\omega_P}^2}{{\omega_0}^2 - \omega^2 - i\omega\Gamma} - \frac{{\Omega_P}^2}{\omega(\omega + i\gamma_c)}, \tag{5.1}$$

where ε_∞ is the high-frequency dielectric constant term and is roughly equal to 4 in this case, the second and the third terms give the 23 cm^{-1} and zero-frequency modes, respectively. From Fig. 5.12, $\varepsilon_1(\omega)$ at 10 K first crosses zero at 16 cm^{-1}. The contribution to $\varepsilon_1(16\ cm^{-1})$ from the first two terms are approximately 1900 estimated

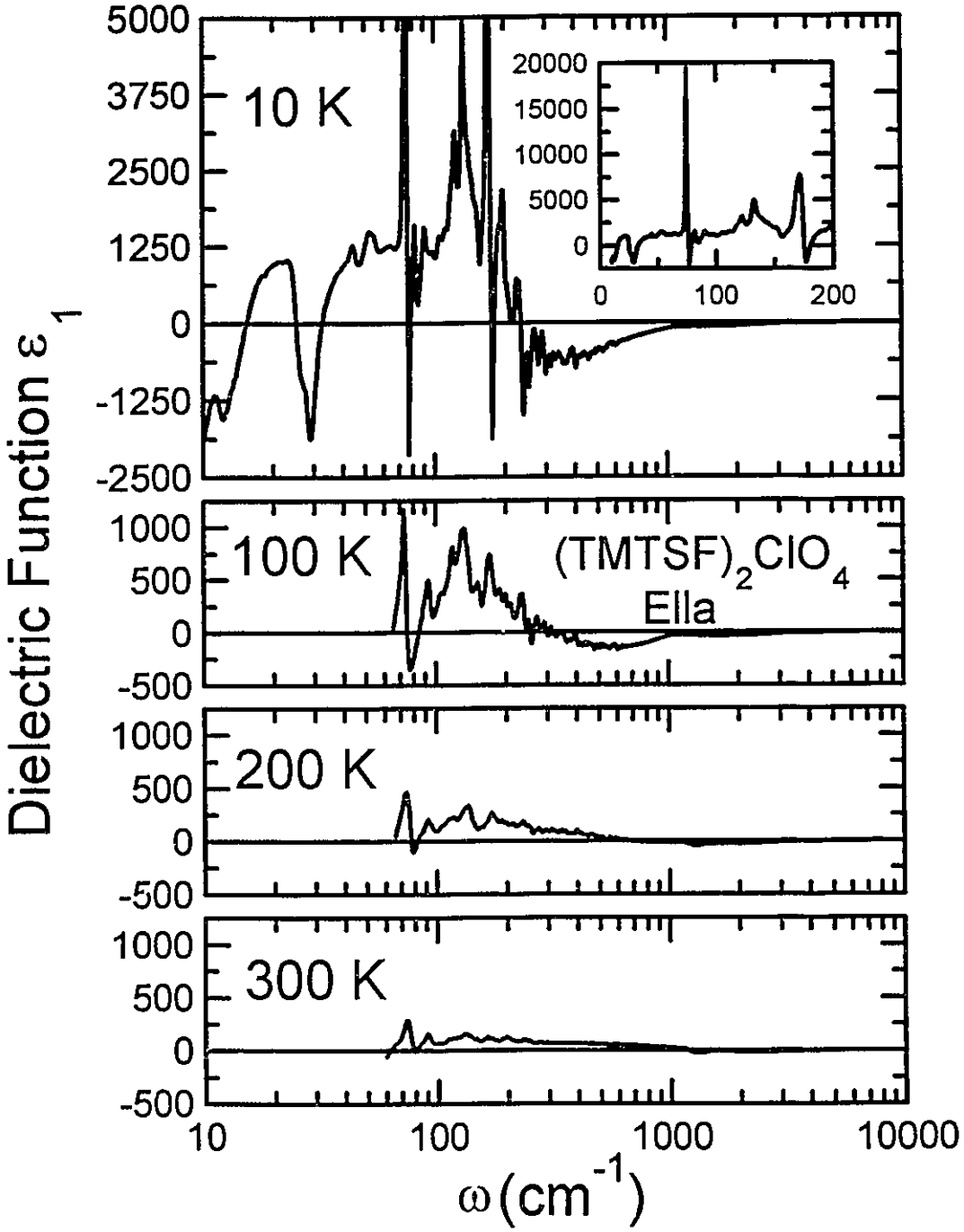

Figure 5.12. Real part of the polarized dielectric function along the chain axis as a function of frequency at 10, 100, 200, and 300 K. Note that the height of the two phase phonon modes around 76 and 172 cm^{-1}, respectively, has been truncated above 5000 cm^{-1} and the real values are shown in the inset of the figure.

from the difference between the zero value at 16 cm^{-1} and the bottom value of the mode at 29 cm^{-1}. Since γ_c<<16 cm^{-1} we may omit γ_c in the third term and obtain the plasma frequency $\Omega_P \cong 700$ cm^{-1}, which is in agreement with the value obtained previously from the fit to the 10 K reflectance data. Using the formula $\sigma_{DC} = \Omega_P^2 / 4\pi\gamma_c$ and σ_{DC}(10 K) ~2×10^5 $\Omega^{-1}cm^{-1}$ we find γ_c~0.04 cm^{-1} at 10 K, which agrees with the values obtained by Ng *et al.* (0.005 cm^{-1} at 2 K and 0.09 cm^{-1} at 25 K).[55]

The zero-frequency collective mode has been suggested by Jacobsen *et al.*[70] to be responsible for the similar behavior in $(TMTSF)_2PF_6$ in term of a theory developed by Lee *et al.*[58] as a current carrying, sliding SDW mode. Besides the collective mode, the theory also predicts that there exists a single-particle part in the conductivity spectrum for ω>2Δ with a shape of the square-root edge resulting from the square-root singularity of the single-particle density of states at ω=2Δ in the SDW state. As shown in Fig. 5.9, the shape of the square-root edge can be seen in the 10 K conductivity background spectrum above 2Δ. Furthermore, the theory indicates that the sliding mode is pinned by impurities at a finite frequency resulting in a decrease of the DC conductivity. This is also the case for $(TMTSF)_2ClO_4$ in the quenched state. As mentioned before an anion disorder-order phase transition happens at 24 K in $(TMTSF)_2ClO_4$ if the material is cooled very slowly. The anion disorder phase can be maintained at low temperatures (T<24 K) by quenching the sample at a higher temperature that leads to a localized electronic behavior for T<6 K.[81] Also the transport measurements on the doped samples $[(TMTSF)_{1-x}(TMTTF)_x]_2ClO_4$ have shown that a non-metallic behavior appears for x≥0.005 at low temperatures.[82]

The zero-frequency mode has been called as the paraconductivity of a quasi-one-dimensional superconductor by Jerome and Schulz in discussing the superconducting fluctuations (SF) in these quasi-one-dimensional organic materials.[83] These authors

believe that if tunneling integral $t_\perp$ between chains is small, the long-range ordered superconductivity will occur at a temperature (T_c) much less than the mean-field value of an individual chain T_c^0; between T_c and T_c^0 strong SF are expected that result in a pseudo-gap in the single-particle density of states and a collective mode contributing to the DC conductivity (the conduction electrons are virtually condensed into the pairs that can be accelerated by an electric field, *i.e.*, electrons come out of the normal Fermi fluid, combining to create virtually bound pairs in a superfluid above the Fermi energy with a lifetime τ_N, and decay back to the Fermi sea with the decay time τ_S). One expects that the paraconductivity increases with decreasing temperature for temperatures below T_c^0 because it is proportional to the mean square amplitude of the superconducting order parameter $<|\Delta|^2>$, which agrees with the result of the temperature dependence of the spectral weight for the zero-frequency mode as shown in Fig. 5.11. The value of T_c^0 for $(TMTSF)_2ClO_4$ could be taken as 70 K deduced above using the mean-field theory. This value agrees well with our experimental results.

5.3 Conclusion

A gap $2\Delta \cong 170$ cm^{-1}, which is related to the short-range ordering of SDW found in the NMR experiment below 25 K, is shown in the chain-axis conductivity spectrum of $(TMTSF)_2ClO_4$ at low temperatures. The precursor of the gap (pseudo-gap) exists for T~100 K that is indicated by both the temperature dependent integrated intensity of the induced phonons and conductivity spectral weight between 2Δ and 1000 cm-1. This gap might be related to the superconducting fluctuations in this quasi-one-dimensional organic superconductor. By fitting the chain-axis reflectance of $(TMTSF)_2ClO_4$ below 60 K we are able to obtained the parameters Ω_p and γ_c of the Drude mode that simulates the narrow mode at zero frequency. This narrow mode is responsible for carrying the

transport current along the chain axis. Surprisingly, we find that the temperature dependence of the spectral weight associated with this narrow mode is quite similar to that associated with the induced phonons found in far-infrared. This clearly indicates the same collective excitation origin for the zero-frequency mode and the induced phonon modes.

Table 5.1. Parameters obtained from fitting the chain-axis reflectance of $(TMTSF)_2ClO_4$ below 60 K to the high-frequency dielectric constant term ε_∞ ($\cong$4), Drude term that simulates the narrow mode at origin, and a series of Lorentz oscillators. γ_c and Ω_P are the width and plasma frequency of the Drude term. ω_i, γ_i, $\omega_P{}^i$, and φ_i are the position, width, strength, and rotated angle of the i^{th} Lorentz oscillator. All units, except for φ_i (in π), are in cm^{-1}.

Mode	T(K)		
	60	20	10
γ_c	0.3871	0.08602	0.03416
Ω_P	455.4	611.7	633.8
ω_1	6.808	7.003	6.995
γ_1	2.920	0.3655	0.3799
$\omega_P{}^1$	312.0	375.5	395.6
φ_1	-0.03588	0	-0.08245
ω_2	14.01	9.944	15.32
γ_2	45.96	9.521	41.94
$\omega_P{}^2$	1322	706.0	1624
φ_2	-0.2745	0	0
ω_3	17.13	28.83	28.19
γ_3	1.241	6.485	4.827
$\omega_P{}^3$	117.3	707.3	631.5
φ_3	0	0.5413	0.3554

ω_4	25.64	31.82	50.70
γ_4	10.13	39.34	11.70
$\omega_P{}^4$	635.1	1580	982.4
φ_4	0.4093	0	0.6653
ω_5	51.77	45.48	53.84
γ_5	16.32	3.461	8.215
$\omega_P{}^5$	1082	252.9	745.2
φ_5	0.6793	0	0
ω_6	54.23	52.85	60.07
γ_6	8.422	19.61	17.60
$\omega_P{}^6$	653.9	1011	1310
φ_6	0	0.7719	0
ω_7	61.58	54.61	74.50
γ_7	21.07	10.08	0.5638
$\omega_P{}^7$	1254	801.4	1050
φ_7	0	0	-0.4502
ω_8	75.80	64.79	148.4
γ_8	2.035	20.54	12.68
$\omega_P{}^8$	905.0	1374	2158
φ_8	-0.2262	0	0
ω_9	97.25	76.01	175.3
γ_9	7.110	0.00003497	2.929
$\omega_P{}^9$	624.7	1066	2220
φ_9	0	-0.4902	0

ω_{10}	133.7	146.0	202.6
γ_{10}	17.95	0.6157	24.86
$\omega_P{}^{10}$	1560	2.053	3858
φ_{10}	-0.3106	0	0
ω_{11}	177.5	187.9	235.4
γ_{11}	3.236	61.14	22.84
$\omega_P{}^{11}$	917.4	4088	3536
φ_{11}	0	0	0
ω_{12}	202.2	238.5	271.2
γ_{12}	31.23	50.90	6.295
$\omega_P{}^{12}$	1822	3242	1140
φ_{12}	0	0	0
ω_{13}	253.8	271.6	295.4
γ_{13}	87.94	1.426	47.56
$\omega_P{}^{13}$	3627	865.7	3061
φ_{13}	0	0	0
ω_{14}	339 9	305.1	342.7
γ_{14}	244.5	43.86	292.6
$\omega_P{}^{14}$	2997	2689	8866
φ_{14}	0	0	-0.07675
ω_{15}	340.8	339.8	350.0
γ_{15}	61.83	54.13	12.28
$\omega_P{}^{15}$	2234	2019	752.1
φ_{15}	0	0	0

ω_{16}	415.8	388.6	400.0
γ_{16}	89.05	460.3	9.435
$\omega_P{}^{16}$	2777	8524	830.2
φ_{16}	0	-0.04550	0
ω_{17}	491.9	400.9	445.0
γ_{17}	121.7	10.84	12.27
$\omega_P{}^{17}$	2263	1114	697.8
φ_{17}	0	0	0
ω_{18}	523.2	459.3	1391
γ_{18}	1292	167.2	782.8
$\omega_P{}^{18}$	8910	2336	7102
φ_{18}	-0.02886	0	0
ω_{19}	603.3	1405	
γ_{19}	145.8	1087	
$\omega_P{}^{19}$	2357	7358	
φ_{19}	0	0	
ω_{20}	1435	3024	
γ_{20}	907.2	1405	
$\omega_P{}^{20}$	6885	1.886	
φ_{20}	0	0	

Chapter 6

Final Remarks

We have presented the optical results of the materials: the pyrochlore oxides $R_2Mo_2O_{7-\delta}$ with R=Sm, Gd, and Ho, the heavy-fermion superconductor UNi_2Al_3, and the quasi-one-dimensional organic superconductor $(TMTSF)_2ClO_4$. As have been discussed in the last three chapters, the questions raised in the first chapter can be answered as follows.

The metal-semiconductor transition found in the DC resistivity measurements of the pyrochlore oxides[1] can be accounted for within the band structure model that was put forward by Sleight and Bouchard.[15] The electrical behavior of $Sm_2Mo_2O_{7-\delta}$ is metallic since the full narrow Mo-O π^*a valence band completely merges into the empty broad R-O σ^* conduction band. With decreasing the ionic radius of R^{3+} for $Gd_2Mo_2O_{7-\delta}$, these two bands overlap slightly. If there are enough oxygen deficiencies in the material, like the case of the single crystal used in this optical work, causing the random potential field larger than the critical one, then the Anderson localization occurs and the DC conductivity turns out to be *via* the variable-range hopping at very low temperatures (T<25 K). The effect of this localization is reflected in the optical conductivity spectra as a linearly depressed conductivity below 400 cm^{-1} at low temperatures. However, for a fully oxygenated polycrystalline $Gd_2Mo_2O_{7-\delta}$ sample, the DC conductivity shows a metallic behavior that, we think, is due to the random potential field is smaller than the critical field. With further decreasing the ionic radius of R^{3+} for $Ho_2Mo_2O_{7-\delta}$, both the DC and the AC conductivity show that this material is a semiconductor with a small gap

(≅0.035 eV from the DC resistivity curve and ≅0.25 eV from the optical conductivity curve with the difference being caused by the different types of the interband transitions) between the Mo-O π^*a valence and the R-O σ^* band.

For the heavy-fermion superconductor UNi_2Al_3, we found that there is a characteristic frequency ω_c(≅90 cm^{-1}) in the real part of the AC conductivity along the a-axis which is compatible with the characteristic temperature T_o(≅100 K) deduced from the DC resistivity and susceptibility results. Above ω_c, the optical conductivity shows a Drude-like behavior for all temperatures. In contrast, below ω_c, the conductivity declines to its DC value for $T \geq T_o$ that is due to the interband transition between the doublet of the ground state and the singlet of the excited state resulting from the CF splitting of $5f^2$ configuration of U^{4+}, whereas it increases sharply to form a narrow Drude-like quasiparticle mode for $T<T_o$. This mode is believed to be caused by the $5f$ band of U moving up to near the Fermi level E_F and then being narrowed by hybridizing with the $3d$ conduction band of Ni in the coherent temperature region ($T<T_o$). As have been mentioned above, the effects of the CF splitting manifest themselves in the conductivity spectra as an interband transition peak around 90 cm^{-1} for $T \geq T_o$.

For the quasi-one-dimensional organic superconductor $(TMTSF)_2ClO_4$, we have demonstrated in the chain-axis optical conductivity spectra that a gap (2Δ≅21 meV) develops at low temperatures. The precursors of the gap (pseudogap) can be seen as high as 100 K. This is the reason why the far-infrared conductivity is so low at low frequencies in the low-temperature region. This gap could be due to the short-range ordering of SDW found in the NMR relaxation rate results for $T<T_c^{3D}$(≅25 K).[61] The pseudogap found between T_c^{3D} and T_c(≅70 K), where T_c is the mean-field transition temperature deduced from the mean-field gap equation, is probably caused by the one-dimensional SDW

fluctuations. A zero-frequency narrow mode is suggested to carry the very larger DC current along the chain axis at low temperatures (T<100 K) which has been supported by both the fitting of the reflectance data to the Drude term as well as the other terms and the large negative values found in $\varepsilon_1(\omega)$ at low frequencies. The spectral weight of this narrow mode decreases rapidly with increasing temperature in the manner similar to the temperature dependence of the spectral weight of the induced phonons appearing in the far-infrared region for ω<2Δ. This strongly indicates that both the zero-frequency narrow mode and the induced phonons have the same collective-excitation origin. The microwave dielectric studies on this material will be very interesting since from which one can see this narrow mode directly.

Appendix A

Lorentz Model

The most frequently used model to simulate the photon-induced excitations in solids is the Lorentz model which can be derived from the following classical Newton's equation,

$$\frac{\partial^2 \vec{r}}{\partial t^2} + \gamma \frac{\partial \vec{r}}{\partial t} + {\omega_0}^2 \vec{r} = \frac{e}{m^*} \vec{E}, \tag{A.1}$$

that describes the motion of an electron with the effective mass m^*, the charge e, the viscous damping term γ, and the eigenvibration frequency ω_0, in a continuous medium under a local electric field $\vec{E}$.

On the other hand, the complex dielectric function $\bar{\varepsilon}(\omega)$ is defined as:

$$\bar{\varepsilon}(\omega) = \frac{\vec{D}}{\vec{E}} = \frac{\vec{E} + 4\pi\vec{P}}{\vec{E}}, \tag{A.2}$$

where $\vec{D}$ and $\vec{P}$ are the displacement and polarization vectors, respectively. The polarization vector $\vec{P}$ is related to the coordination of the electron $\vec{r}$ by the expression:

$$\vec{P} = eN\vec{r}, \tag{A.3}$$

where N is the density of electrons in the medium.

Applying a trial solution $\vec{r} = \vec{r}_0 e^{-i\omega t}$ to Eqn. A.1, one gets

$$\vec{r} = \frac{e}{m^*} \frac{\vec{E}}{\omega_0{}^2 - \omega^2 - i\gamma\omega}. \tag{A.4}$$

Substituting Eqn. A.4 into Eqn. A.3 and using Eqn. A.2, one can finally obtain the Lorentz complex dielectric function as follows,

$$\bar{\varepsilon}(\omega) = 1 + \frac{\omega_P{}^2}{\omega_0{}^2 - \omega^2 - i\omega\gamma}, \tag{A.5}$$

where $\omega_P{}^2 = \frac{4\pi N e^2}{m^*}$.

Sometimes, a phonon shape that is due to the phonon-electron interaction is not symmetric. In such a case, one can use a so-called "rotated Lorentz oscillator" model to simulate this kind of the phonon shape. This model is expressed in the following formula:

$$\bar{\varepsilon}(\omega) = 1 + \frac{\omega_P{}^2 e^{i\varphi}}{\omega_0{}^2 - \omega^2 - i\omega\gamma}, \tag{A.6}$$

where φ is the rotated angle.

Appendix B

Fano Lineshape

The mixing effects between a discrete state and a continuum have been studied in details by Fano referred to as the so-called Fano lineshape.[20] The conclusion drawn from these studies is that the mixing can lead to *a change of the lineshape of the discrete state from a symmetric one to an asymmetric one.* In the case that we are interested in the discrete state refers to a phonon excitation, whereas the continuum refers to an electronic background.

Let's suppose a discrete state φ with the energy E_φ and a continuum of states $\psi_{E'}$ to satisfy the following relations:

$$\langle \varphi | H | \varphi \rangle = E_\varphi, \tag{B.1}$$

$$\langle \psi_{E'} | H | \varphi \rangle = V_{E'}, \tag{B.2}$$

$$\langle \psi_{E''} | H | \psi_{E'} \rangle = E' \delta(E'' - E'), \tag{B.3}$$

where H is the Hamiltonian of the system, and $V_{E'}$ is the off-diagonal matrix element between the states $\psi_{E'}$ and φ, in this case, is also the strength of the electron-phonon (e-p) interaction. Here the discrete energy level E_φ lies within the energy range of the continuum states E'.

Next, one is going to diagonalize the energy matrix elements of states $\varphi, \psi_{E'}$. To do this, one firstly writes the eigenstate of states $\varphi, \psi_{E'}$ as:

$$\Psi_E = a\varphi + \int dE' b_{E'} \psi_{E'}, \tag{B.4}$$

with the corresponding eigenvalue E within the range of E'. Using Eqs. B.1, B.2, and B.3, one has the following two relations to determine the coefficients a and $b_{E'}$:

$$E_\varphi a + \int dE V_{E'} b_{E'} = Ea, \tag{B.5}$$

$$V_{E'} a + E' b_{E'} = E b_{E'}. \tag{B.6}$$

So, the diagonalization of the matrix, shown in Eqs. B.1, B.2, and B.3, is fulfilled. In the concrete, from Eqn. B.6 one has the relation between $b_{E'}$ and a:

$$b_{E'} = \left[\frac{1}{E - E'} + z(E)\delta(E - E') \right] V_{E'} a, \tag{B.7}$$

where the second term comes as $E = E'$ and $z(E)$ will be determined later. The phase shift due to the interaction of $\psi_{E'}$ with the state φ is:

$$\Delta = -\arctan[\pi / z(E)]. \tag{B.8}$$

Substituting Eqn. B.7 to Eqn. B.5 one obtains the expression:

$$E_\varphi + F(E) + z(E)|V_E|^2 = E, \tag{B.9}$$

where

$$F(E) = P\int dE' \frac{|V_{E'}|^2}{E - E'}, \tag{B.10}$$

and P denotes "principal part of." From Eqn. B.9 one has:

$$z(E) = \frac{E - E_\varphi - F(E)}{|V_E|^2}. \tag{B.11}$$

From Eqs. B.8 and B.11 one can see that the phase shift changes sharply by ~π as E passes through the "resonance" at $E = E_\varphi + F$ within an interval ~$|V_E|^2$. The quantity F *is* the shift of the resonance position with respect to E_φ.

From the normalization requirement,

$$\left\langle \Psi_{\bar{E}} \middle| \Psi_E \right\rangle = a^*(\bar{E})a(E) + \int dE' b_{E'}{}^*(\bar{E}) b_{E'}(E) = \delta(\bar{E} - E), \tag{B.12}$$

and considering Eqs. B.7 and B.8, one can obtain:

$$a = \frac{\sin\Delta}{\pi V_E}, \tag{B.13}$$

$$b_{E'} = \frac{V_{E'}}{\pi V_E}\frac{\sin\Delta}{E-E'} - \cos\Delta\delta(E-E'), \tag{B.14}$$

where, according to Eqs. B.8 and B.11,

$$\Delta = -\arctan\frac{\pi|V_E|^2}{E-E_\varphi - F(E)}. \tag{B.15}$$

Supposing that there is a transition operator T acting on an initial state i and causing a transition to the state Ψ_E, the matrix element represented this transition process is expressed as:

$$\langle\Psi_E|T|i\rangle = \frac{1}{\pi V_E^*}\langle\Phi|T|i\rangle\sin\Delta - \langle\psi_E|T|i\rangle\cos\Delta, \tag{B.16}$$

where

$$\Phi = \varphi + P\int dE'\frac{V_{E'}\psi_{E'}}{E-E'}, \tag{B.17}$$

which indicates that the state φ is modified by an admixture of states of the continuum. As mentioned above, the phase shift Δ changes substantially as the energy E passes through the resonance position $E_\varphi + F$. Since $\sin\Delta$ is an even function of $E-E_\varphi-F$, whereas $\cos\Delta$ is an odd function of this variable, the terms of $\langle\Phi|T|i\rangle$ and $\langle\psi_E|T|i\rangle$ in Eqn. B.16 interfere with opposite phase on the two sides of the resonance which results in the

transition probability, expressed as the squared matrix element $\left|\langle \Psi_E | T | i \rangle\right|^2$, to be zero on one side of the resonance at $\Delta = \Delta_0$, *i.e.*, $E = E_0$, where

$$\tan \Delta_0 = -\frac{\pi |V_{E_0}|^2}{E_0 - E_\varphi - F(E_0)} = \frac{\pi V_{E_0} \langle \psi_{E_0} | T | i \rangle}{\langle \Phi | T | i \rangle}. \tag{B.18}$$

Finally, the Fano lineshape is expressed as the ratio of the transition probability $\left|\langle \Psi_E | T | i \rangle\right|^2$ to the probability $\left|\langle \psi_E | T | i \rangle\right|^2$ that is of the transition to the unperturbed continuum:

$$\frac{\left|\langle \Psi_E | T | i \rangle\right|^2}{\left|\langle \psi_E | T | i \rangle\right|^2} = \frac{(q+\varepsilon)^2}{1+\varepsilon^2}, \tag{B.19}$$

where

$$q = \frac{\langle \Phi | T | i \rangle}{\pi V_E^* \langle \psi_E | T | i \rangle}, \tag{B.20}$$

$$\varepsilon = -\cot \Delta = \frac{2(E - E_\varphi - F)}{\Gamma}, \tag{B.21}$$

in which $\Gamma = 2\pi |V_E|^2$, that is the spectral width of the state φ. Fig. B.1 shows the Fano lineshapes for several values of q. Usually, the quantities q, $F(E)$, and Γ can be regarded as independent of E over a sufficient range.

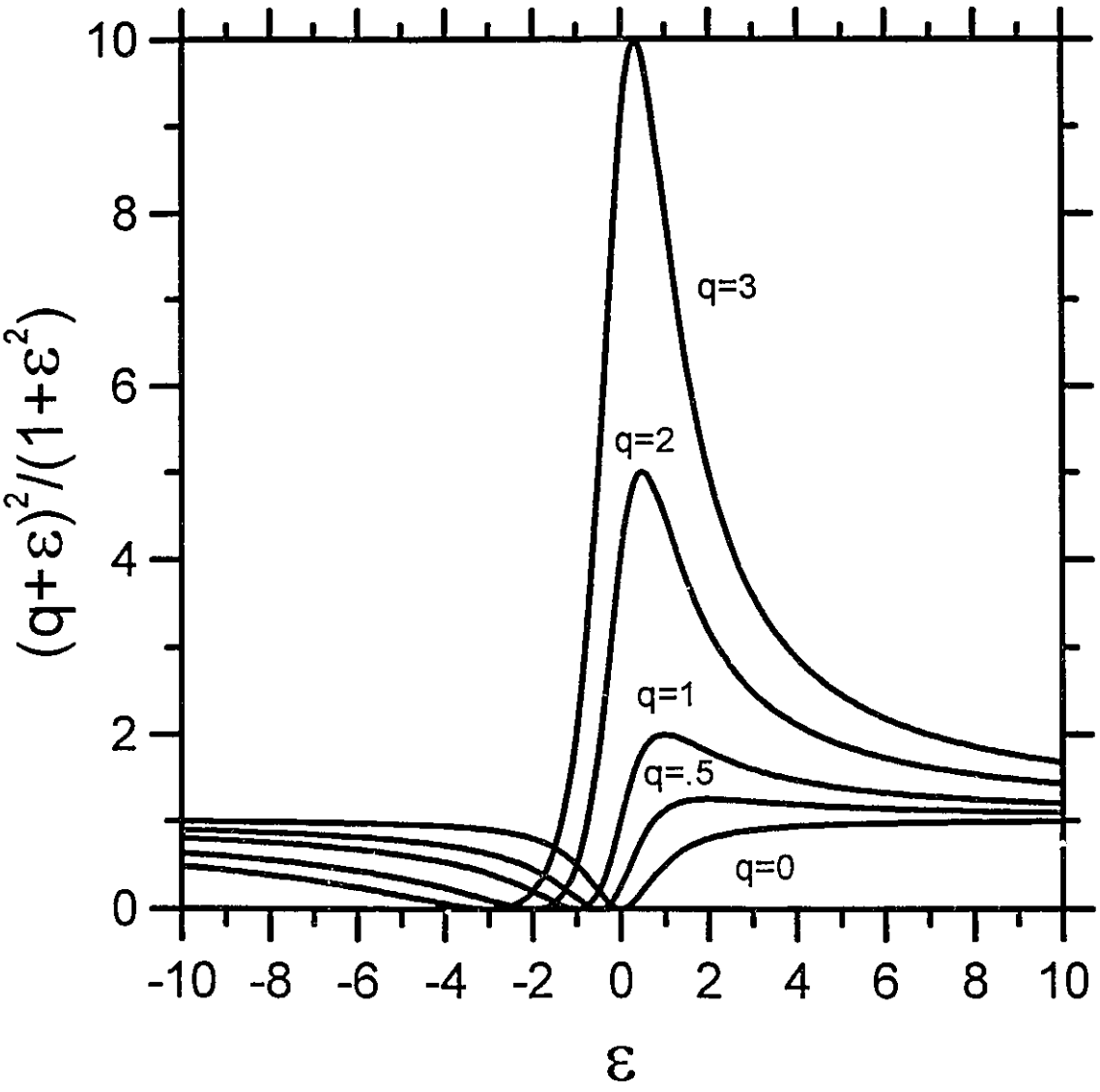

Figure B.1. Fano lineshapes for q=0, 0.5, 1, 2, and 3.

Appendix C

Anderson Localization

The behavior of electrons in a crystal can be described by band models, *e.g.*, the nearly-free electron model (NFE). The basic point of NFE model is that the potential energy $V(x,y,z)$ is a periodic function of the lattice, so that one can express it into a sum of the Fourier components in reciprocal space. Inserting this expression into the Schrödinger equation one can obtain the energy bands of electrons in the crystal. The electronic behavior of a material can be explained by the band theory: if the conduction band of a material is partially filled, it is a metal; it is an insulator, in which the density of states $N(E_F)$ vanishes at the Fermi level E_F, if the conduction band of a material is empty.

If $V(x,y,z)$ is not periodic, *e.g.*, in the impurity band of doped semiconductors and in non-crystalline materials, what happens to the electronic behaviors in these materials? Anderson has presented a theory for answering this question, which is referred to as Anderson localization.[16,26] He pointed out that if the random potential in these materials is strong enough, *i.e.*, $(V_0/B) > (V_0/B)_{crit.}$, where $\pm\frac{1}{2}V_0$ are the limits within which the random potential varies, B is the band width, and the value of $(V_0/B)_{crit.} \approx 2$, the localization of the one-electron wave functions can happen. In this localization, *the density of states at E_F is non-zero* and the AC conductivity $\sigma_1(\omega)$ is always finite for $\omega \neq 0$ at T=0, but approaches zero roughly as ω^2 as $\omega \to 0$. On the other hand, the DC conductivity vanishes at T=0, and is by thermally activated hopping obeying the $T^{1/4}$ law at small T.

Mott develops this theory by presenting the idea of the mobility edge E_c that separates localized from non-localized states.[84] Fig. C.1 illustrates that if a conduction and valence band in a non-crystalline system overlap slightly, there exists a pseudogap between E_c' and E_c where all electronic states are localized.[26] In this case the Fermi level E_F sits within the pseudogap region. The DC conductivity results from thermal excitations of electrons to the mobility edge E_c at high temperatures that can be expressed as:

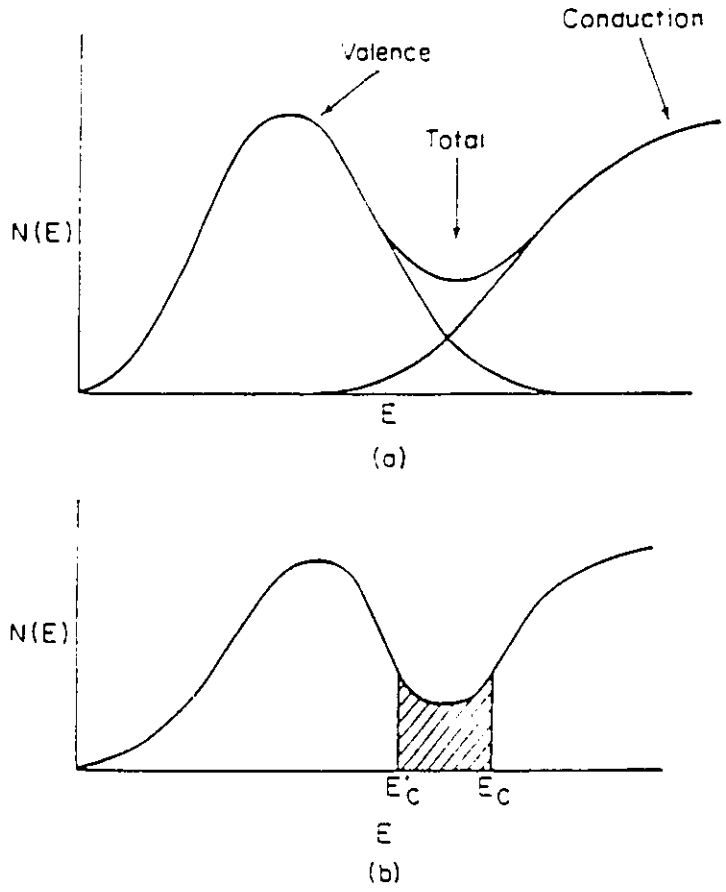

Figure C.1. (a) Overlapping slightly between the valence and conduction bands causing a pseudogap with the Fermi level E_F located in the localized region; **(b)** The total density of states, with localized states shaded. From Ref. 26.

$$\sigma \approx \sigma_0 \exp\left[-(E_c - E_F)/k_B T\right], \tag{C.1}$$

where $\sigma_0 = 0.026e^2/\hbar a$. As mentioned above, at very low temperatures the DC conductivity is by the variable-range hopping and behaves as:

$$\sigma \approx \sigma_1 \exp\left[-(Q/T)^{1/4}\right], \tag{C.2}$$

where σ_1 is a prefactor, $Q = 1.5\alpha^3/N(E_F)$, $N(E_F)$ is the density of states at E_F and α represents the fall-off rate of the envelope of the wave function $\phi \propto \exp(-\alpha r)$.

Mott and Davis have studied the AC hopping conductivity in a non-crystalline medium.[24] Their theory begins with assuming that a dipole D, which has two alternative positions with the energies W_1, W_2 ($\Delta W = W_1 - W_2$), is built up at each of n sites per unit volume. The polarization of the dipole induced by applying an external field F can be expressed as

$$\left\{FD^2 \overline{\cos^2\theta}/k_B T\right\}/(1+e^{\Delta W/k_B T}), \tag{C.3}$$

where $\overline{\cos^2\theta}$ is an average over all possible values of θ, here θ is the angle between the directions of the polarization and the external field, and is equal to $\frac{1}{3}$. Then the AC conductivity can be calculated to be:

$$\sigma_1(\omega) = \frac{nD^2}{3k_B T}\frac{1}{1+\exp(\Delta W/k_B T)}\frac{\omega^2\tau}{1+\omega^2\tau^2}, \tag{C.4}$$

where τ is the mean time for a transition from the upper to the lower state. After averaging over a range of values of ΔW, one has:

$$\sigma_1(\omega) = 0.2nN(W)D^2\omega^2\tau/(1+\omega^2\tau^2), \tag{C.5}$$

where $N(W)$ is the number of pairs between W and $W+dW$. In order to average over τ, one supposes that for each hopping process an electron must overcome a barrier with the height U. The rate for occurring this process is:

$$1/\tau = \nu_{ph}\exp(-U/k_BT). \tag{C.6}$$

If $B(U)dU$ is the number of barriers of height between U and $U+dU$, then, one can write $d\tau/\tau = dU/k_BT$. The average of $\omega^2\tau/(1+\omega^2\tau^2)$ turns out to be $\frac{1}{2}\pi k_BTB(U)\omega$ provided that $B(U)$ is constant. Finally, one can obtain the AC hopping conductivity that can be expressed as:

$$\sigma_1(\omega) \approx 0.3nN(W)B(U)D^2k_BT\omega, \tag{C.7}$$

which is proportional to both T and ω.

As the degree of the overlap increases, the Fermi level E_F will move from the localized region to the extended region above E_c which is the case of the Anderson insulator-metal transition.

Bibliography

1. J.E. Greedan, M. Sato, N. Ali, and W.R. Datars, J. Solid State Chem., **68**, 300 (1987).
2. P.A. Lee, T.M. Rice, J.W. Serene, L.J. Sham, and J.W. Wilkins, Comments on Condensed Matter Phys., **128**, 99 (1986).
3. R.A. Steeman, E. Frikkee, C. van Dijk, G.J.Nieuwenhuys, and A.A. Menovksy, J. Magn. Magn. Mat., **76&77**, 435 (1988); A. Grauel, A. Bohm, H. Fischer, C. Geibel, R. Kohler, R. Modler, C. Schank, F. Steglich, G. Weber, T. Komatsubara, and N. Sato, Phys. Rev. **B**, **46**, 5818 (1992).
4. K. Bechgaard, K. Carneiro, M. Olsen, F.B. Rasmussen, and C.S. Jacobsen, Phys. Rev. Lett., **46**, 852 (1981).
5. H.K. Ng, T. Timusk, and K. Bechgaard, J. Phys. (Paris), Colloq. **C3**, 867 (1983).
6. C. Kittel: Introduction to Solid State Physics (Fifth Edition, New York: John Wiley & Sons Inc., 1976) pp 323-326; pp 441-443.
7. J.W. Allen and J.C. Mikkelsen, Phys. Rev. **B**, **57**, 2952 (1977).
8. N. Cao, T. Timusk, N.P. Raju, J.E. Greedan, and P. Gougeon, J Phys.: Condens. Matte, 7, 2489 (1995).
9. J.N. Reimers, A.J. Berlinsky, and A.C. Shi, Phys. Rev. **B**, **43**, 865 (1991) .
10. B.D. Gaulin, J.N. Reimers, T.E. Mason, J.E. Greedan, and Z. Tun, Phys. Rev. Lett., **69**, 3244 (1992).
11. J.E. Greedan, M. Sato, Xu Yan, and F.S. Razavi, Solid State Commun., **59**, 895 (1986).
12. M. Sato, X. Yan, and J.E. Greedan, Z. Anorg. Allg. Chem., **540/541**, 177 (1986).
13. N.P. Raju, E. Gmelin, and R.K. Kremer, Phys. Rev. **B**, **46**, 5405 (1992).
14. P.J. Ford and J.A. Mydosh, Phys. Rev. **B**, **14**, 2057 (1976).

15. A.W. Sleight and R.J. Bouchard, Proc. 5th Materials Research Symp., (NBS special Publication 364) 227 (1972).

16. P.W. Anderson, Phys. Rev., **109**, 1492 (1958).

17. J.N. Reimers and J.E. Greedan, J. Solid State Chem., **72**, 390 (1988).

18. J.N. Reimers, J.E. Greedan, R.K. Kremer, E. Gmelin, M.A. Subramanian, Phys. Rev. **B**, **43**, 3387 (1991).

19. N.P. Raju, G. Liu, N. Cao, T. Timusk, J.E. Greedan, and P. Gougeon, to be published.

20. U. Fano, Phys. Rev., **124**, 1866 (1961).

21. A.S. Barker, Jr., and J.A. Ditzenberger, Phys. Rev. **B**, **1**, 4378 (1970).

22. D.A. Bonn, J.D. Garrett, and T. Timusk, Phys. Rev. Lett., **61**, 1305 (1988).

23. N. Cao, J.D. Garrett, and T. Timusk, Physica **B**, **191**, 263 (1993).

24. N.F. Mott and E.A. Davis: Electronic Processes in Non-crystalline Materials (Oxford:Clarendon Press, 1971) p 51.

25. H.F. Jang, G. Gripps, and T. Timusk, Phys. Rev. **B**, **41**, 5152 (1990).

26. N.F. Mott: Metal-insulator Transitions (London: Taylor and Francis Ltd., 1974) Chapter 1.

27. N.P. Raju and G. Rangarajan, J. Phys.: Condens. Matter, **2**, 3539 (1990).

28. P.G. Le Comber, A. Madan, and W.E. Spear, J. Non-Crystalline Solids, **11**, 219 (1972).

29. M.J. Weber, B.H. Matsinger, V.L. Donlan, and G.T. Surratt, J. Chem. Phys., **57**, 562 (1972).

30. P. Gougeon, N.P. Raju, Guo Liu, and J.E. Greedan, to be published.

31. T.T.M. Palstra, A.A. Menovsky, J. van den Berg, A.J. Dirkmaat, P.H. Kes, G.J. Nieuwenhuys, and J.A. Mydosh, Phys. Rev. Lett., **55**, 2727 (1985).

32. G. Aeppli, E. Bucher, C. Broholm, J.K. Kjems, J. Baumann, and J. Hufnagl, Phys. Rev. Lett., **60**, 615 (1988).

33. M.B. Maple, J.W. Chen, Y. Dalichaouch, T. Kohara, C. Rossel, M.S. Torikachachvili, M.W. McElfresh, and J.D. Thompson, Phys. Rev. Lett., **56**, 185 (1985).

34. P. Santini and G. Amoretti, Phys. Rev. Lett., **73**, 1027 (1994).

35. A. Edelstein, Phys. Lett., **27 A**, 614 (1968); S. Doniach, Physica, **91B**, 231 (1977).

36. A.J. Millis and P.A. Lee, Phys. Rev. **B**, **35**, 3394 (1987).

37. M.S.S. Brooks and P.J. Kelly, Phys. Rev. Lett., **51**, 1708 (1983); J. Sticht and J. Kubler, Solid State Commun., **54**, 389 (1985).

38. A. de Visser, J.J.M. Franse, A. Menovsky, and T.T.M. Palstra, Physica **B+C**, **127B**, 442 (1984).

39. Piers Coleman, Phys. Rev. Lett., **59**, 1026 (1987).

40. D.A. Bonn, J.D. Garrett, and T. Timusk, Phys. Rev. Lett., **61**, 1305 (1988).

41. P.E. Sulewski, A.J. Sievers, M.B. Maple, M.S. Torikachvili, J.L. Smith, and Z. Fisk, Phys. Rev. **B**, **38**, 5338 (1988).

42. F. Marabelli, G. Travaglini, P. Wachter, and J.J.M. Franse, Solid State Commun., **59**, 381 (1986).

43. C. Geibel, S. Thies, D. Kaczorowski, A. Mehner, A. Grauel, B. Seidel, U. Ahlheim, R. Helfrich, K. Petersen, C.D. Bredl, and F. Steglich, Z. Phys. **B** - Condensed Matter, **83**, 305 (1991).

44. C. Geibel, C. Schank, S. Thies, H. Kitazawa, C.D. Bredl, A. Bohm, M. Rau, A. Grauel, R. Caspary, R. Helfrich, U. Ahlheim, G. Weber, and F. Steglich, Z. Phys. **B** - Condensed Matter, **84**, 1 (1991).

45. L. Degiorgi, M. Dressel, G. Gruner, P. Wachter, N. Sato, T. Komatsubara, and Y. Uemura, Europhys. Lett., **25**, 311 (1994).

46. A. Schroder, J.G. Lussier, B.D. Gaulin, J.D. Garrett, W.J.L. Buyers, L. Rebelsky, and S.M. Shapiro, Phys. Rev. Lett., **72**, 136 (1994).

47. J. Sticht and J. Kubler, Z. Phys. **B**-Condensed Matter, **87**, 299 (1992).

48. F. Steglich *et al.*, Physica **C**, **185-189**, 379 (1991).

49. J. Aarts, A.P. Volodin, A.A. Menovsky, G.J. Nieuwenhuys, and J.A. Mydosh, Europhys. Lett., **26**, 203 (1994).

50. N. Cao, J.D. Garrett, and T. Timusk, Physica **B**, **191**, 263 (1993).

51. T. Van Duzer and C.W. Turner: Principles of Superconductive Devices and Circuits (Elsevier North Holland, Inc., 1981) p 123.

52. B.C. Webb, A.J. Sievers, and T. Mihalisin, Phys. Rev. Lett., **57**, 1951 (1986).

53. B. Gallois, D. Chasseau, J. Gaultier, C. Hauw, A. Filhol, and K. Bechgaard, J. Phys. (Paris), Colloq. **C3**, 1071 (1983).

54. J.P. Pouget, G. Shirane, K. Bechgaard, and J.M. Fabre, Phys. Rev. **B**, **27**, 5203 (1983).

55. H.K. Ng, T. Timusk, and K. Bechgaard, Mol. Cryst. Liq. Cryst., **119**, 191 (1985).

56. C.S. Jacobsen, D.B. Tanner, A.F. Garito, and A.J. Heeger, Phys. Rev. Lett., **33**, 1559 (1974); D.B. Tanner, C.S. Jacobsen, A.F. Garito, and A.J. Heeger, Phys. Rev. **B**, **13**, 3381 (1976); D.B. Tanner, K.D. Cummings, and C.S. Jacobsen, Phys. Rev. Lett., **47**, 597 (1981).

57. J. Bardeen, Solid State Commun., **13**, 357 (1973); D. Allender, J.W. Bray, and J. Bardeen, Phys. Rev. **B**, **9**, 119 (1974).

58. P.A. Lee, T.M. Rice, and P.W. Anderson, Solid State Commun., **14**, 703 (1974).

59. H. Fröhlich, Proc. Roy. Soc. London **A**, **223**, 296 (1954).

60. H. Basista, D.A. Bonn, T. Timusk, J. Voit, D. Jerome, and K. Bechgaard, Phys. Rev. **B**, **42**, 4088 (1990).

61. P. Wzietek, F. Creuzet, C. Bourbonnais, D. Jerome, K. Bechgaard, and P. Batail, J. Phys. I France, **3**, 171 (1993).

62. D. Djurek, M. Prester, D. Jerome, and K. Bechgaard, J. Phys. **C**, **15**, 669 (1982); D. Djurek, S. Knezovic, and K. Bechgaard, Mol. Cryst. Liq. Cryst., **119**, 161 (1985).

63. D. Jerome, Mol. Cryst. Liq. Cryst., **119**, 1 (1985).

64. W.M. Walsh, Jr., F. Wudl, E. Aharon-Shalom, L.W. Rupp, Jr., J.M. Vandenberg, K. Andres, and J.B. Torrance, Phys. Rev. Lett., **49**, 885 (1982).

65. J.E. Eldridge and G.S. Bates, Mol. Cryst. Liq. Cryst., **119**, 183 (1985).

66. K. Kikuchi, I. Ikemoto, K. Yakushi, H. Kuroda, and K. Kobayashi, Solid State Commun., **42**, 433 (1982).

67. D. Pedron, R. Bozio, M. Meneghetti, and C. Pecile, Phys. Rev. **B**, **49**, 10893 (1994).

68. M. Meneghetti, R. Bozio, I. Zanon, C. Pecile, C. Ricotta, and M. Zanetti, J. Chem. Phys., **80**, 6210 (1984).

69. M.J. Rice, C.B. Duke, and N.O. Lipari, Solid State Commun., **17**, 1089 (1975); M.J. Rice, Phys. Rev. Lett., **37**, 36 (1976).

70. C.S. Jacobsen, D.B. Tanner, and K. Bechgaard, Phys. Rev. **B**, **28**, 7019 (1983).

71. H.K. Ng, T. Timusk, D. Jerome, and K. Bechgaard, Phys. Rev. **B**, **32**, 8041 (1985).

72. C.C. Homes and J.E. Eldridge, Phys. Rev. **B**, **42**, 9522 (1990).

73. C. Bourbonnais, a private communication.

74. P.A. Lee, T.M. Rice, and P.W. Anderson, Phys. Rev. Lett., **31**, 462 (1973).

75. R. Bozio, M. Meneghetti, and C. Pecile, Phys. Rev. **B**, **36**, 7795 (1987).

76. J.L. Musfeldt, M. Poirier, P. Batail, and C. Lenoir, submitted to Phys. Rev. **B**.

77. K. Bechgaard, C.S. Jacobsen, K. Mortensen, H.P. Pedersen, and N. Thorup, Solid State Commun., **33**, 1119 (1980).

78. J.L. Musfeldt, M. Poirier, P. Batail, and C. Lenoir, Phys. Rev. **B**, 51, 8347 (1995).

79. D. Jerome, A. Mazaud, M. Ribault, and K. Bechgaard, J. Phys. Lett. (Paris), **41**, 95 (1980).

80. D. Jerome, Organic Conductors: Fundamentals and Applications, edited by J.P. Farges (Marcel Dekker, Inc., 1994) p 431.

81. S. Tomic, D. Jerome, P. Monod, and K. Bechgaard, J. Phys. (Paris), Colloq. **C3**, 1083

(1983).

82. C. Coulon, P. Delhaes, J. Amiell, J.P. Manceau, J.M. Fabre, and L. Giral, J. Physique, **43**, 1721 (1982).

83. D. Jerome and H.J. Schulz, Advances in Physics, **31**, 299 (1982).

84. N.F. Mott, Phil. Mag., **13**, 989 (1966).

85. A.M. Mamedov and A.H. Zejnally, J. Phys. Soc. Jpn., **49**, 125 (1980).

86. W.J.L. Buyers, private communication.